

**VIBRO-ACOUSTIC RESPONSE OF
AEROSPACE STRUCTURE UNDER
NON-UNIFORM EDGE LOADS:
AN ANALYTICAL INVESTIGATION**

Thesis

Submitted in partial fulfillment of the requirement for the degree of

DOCTOR OF PHILOSOPHY

by

VIJAY G



**DEPARTMENT OF MECHANICAL ENGINEERING
NATIONAL INSTITUTE OF TECHNOLOGY KARNATAKA,
SURATHKAL, MANGALORE – 575025, INDIA**

March, 2022

*Dedicated to my NGO kids at
Edforall, Aurobindo street,
Puducherry, India*

DECLARATION

I hereby *declare* that the Research Thesis entitled **VIBRO-ACOUSTIC RESPONSE OF AEROSPACE STRUCTURE UNDER NON-UNIFORM EDGE LOADS: AN ANALYTICAL INVESTIGATION** which is being submitted to the *National Institute of Technology Karnataka, Surathkal* in partial fulfillment of the requirements for the award of the Degree of *Doctor of Philosophy* is a *bonafide report of the research work carried out by me*. The material contained in this Thesis has not been submitted to any University or Institution for the award of any degree.



VIJAY G

Register No.: 177097ME022

Department of Mechanical Engineering.

Place: NITK – Surathkal

Date: 21/03/2022

CERTIFICATE

This is to *certify* that the Research Thesis entitled **VIBRO-ACOUSTIC RESPONSE OF AEROSPACE STRUCTURE UNDER NON-UNIFORM EDGE LOADS: AN ANALYTICAL INVESTIGATION**, submitted by **VIJAY G** (Register Number: 177097ME022) as the record of the research work carried out by him, is *accepted* as the *Research Thesis submission* in partial fulfilment of the requirements for the award of degree of **Doctor of Philosophy**.


Dr. P. Jeyaraj

Research Guide

Associate Professor

Department of Mechanical Engineering.

NITK Surathkal – 575025


Chairman – DRPC 21.3.2022

(Signature with Date and Seal)



ACKNOWLEDGEMENTS

It is my great pleasure to express my heartfelt gratitude to my research supervisor Dr. P. Jeyaraj, Associate Professor, Department of Mechanical Engineering, National Institute of Technology Karnataka, Surathkal, Mangalore, for his exemplary guidance and encouragement throughout my research work. Working under him has had a profound effect not only on how research should be carried out at its best, but also on how to develop humbleness and kindness towards students. Without his support and suggestions, achieving this goal would not have been possible.

I sincerely thanks to the RPAC members, Dr. Arun Kumar Thalla, Department of Civil Engineering and Dr. Hemantha Kumar, Department of Mechanical Engineering for providing valuable suggestion and support extended to me on all occasion.

I wish to express my sincere thanks to Prof. Ravikiran Kadoli, Head of the Department, Department of Mechanical Engineering, National Institute of Technology Karnataka, Surathkal, Mangalore, for their kind help in providing the facilities.

I wish to express my sincere thanks to Dr. M C Leninbabu, Department of Mechanical Engineering, Vellore Institute of Technology, Chennai campus, for sharing his knowledge, which greatly helped me to carry out my research work.

I sincerely acknowledge the help rendered to me by M.Tech guys Saurabh Ranjan and Ashish Kumar during my earlier stages of research.

I would like to thank Kutotikonda Akshita on her encouragement and moral support during the downhearted time in research.

I wish to express my sincere thanks to my friend Arul Raj Vaiduriyam, Research scholar, VIT University, Chennai campus, for his selfless advice and support to join as a research scholar in NITK.

I acknowledge my sincere thanks to Somi Naidu Bali Reddy for his moral support during the downhearted time in research.

I am grateful to my friends STG Krishna Teja, Karishma Bendale, Arjun B, Vasanthakumar V, Anandraj C S, Thivash V and others for their encouragement during research. Days spent with Praveen J, Rakesh Patil, Mohammed Sohail Bakshi, Purna Chandra Tanti, Vinayak kallannavar and Chetan H. C. in NITK hostel are not forgettable.

I would like to thank God for giving me the strength, knowledge, ability and opportunity to understand this research study and to persevere and complete it satisfactorily.

I would like to thank my father Gunasekaran, mother Kannagi Devi and sister Vishvaja, for their massive love and support throughout my life. Without them, achieving this goal would not have been possible.

“Last but not least,

I want to thank ME for believing in ME.

I want to thank ME for doing all this hard work.

I want to thank ME for having no days off.

I want to thank ME for never quitting.

I want to thank ME for being a giver and trying to give more than I receive.”

(By Snoop Dogg)

(VIJAY G)

ABSTRACT

KEYWORDS: Analytical solutions; FG-graphene reinforced nanocomposites; 2D continuum orthotropic plate model; Non-uniform uniaxial edge loads; Reddy's TSDT; elastic buckling; Sound radiation; Sound transmission loss;

Analytical investigation carried on vibro-acoustic characteristics of plates under different non-uniform uniaxial edge loads, subjected to steady-state mechanical and acoustic waves excitation is presented. Owing to their high stiffness to weight ratio, these functionally graded-graphene reinforced nanocomposites (FG-GRC) are used as structural members in unified wing aircrafts, space launchers etc., these Graphene reinforced nanocomposites plate is assumed to be a layered structure, in which weight fraction (W_{GNP}) of the graphene nanoplatelets ($GNPs$) continuously vary in each layer through the plate thickness. It is also assumed that $GNPs$ are evenly distributed in longitudinal direction, but randomly slanted towards the transverse direction of plate. By using 2D continuum orthotropic plate model, the effective material properties of graphene reinforced nanocomposites with different grading pattern/weight fraction of $GNPs$ are obtained by combining the modified Halpin-Tsai model and rule of mixture. In order to model the porous graphene reinforced nanocomposites, closed-cell cellular solids under Gaussian Random Field (GRF) are used. An analytical method based on the strain energy approach is adopted to estimate the buckling load (P_{cr}). Free and forced vibration responses of the plate are obtained, by using an analytical method based on Reddy's third-order shear deformation theorem (TSDT). Further, vibration response of the plate is given as an input to the Rayleigh integral code built-in-house using MATLAB[®] to obtain the acoustic response characteristics. Validation studies carried out to ensure the accuracy of results based on 2D continuum orthotropic plate model. The predicted buckling, vibration and acoustic characteristic results of graphene reinforced nanocomposites plates by using the 2D continuum orthotropic plate model is compared with the published results and shows the good agreement with the present approach.

Initially, influence of non-uniform uniaxial edge (NUE) loads on vibration and acoustic response isotropic plates is investigated. The results reveals that the buckling load (P_{cr}) is significantly influenced by the nature of NUE loads. Similarly, natural frequencies reduce with an increase in axial compressive load due to a reduction in structural stiffness. Vibration and acoustic resonant amplitudes are affected by the intensity of the compressive load. Sound transmission loss reduces with an increase in compressive load magnitude and the effect is significant in the stiffness dominant region.

Followed by this, free vibration and buckling characteristics of graphene reinforced nanocomposites under the different NUE loads, four distinctive gradings (i.e., UD, X, O, and C patterns of $GNPs$) and different W_{GNP} are studied. Results revealed that buckling and free vibration behaviour of the plate is significantly influenced by the $GNPs$ dispersion pattern and weight fraction under non-uniform edge loads. It is also observed that buckling mode and the fundamental vibration mode of the plate under combined tensile-compression load (i.e., load factor (α) = 2) is entirely different from the other NUE load cases. Furthermore, to understand the vibro-acoustic characteristics of graphene reinforced nanocomposites under the different NUE loads, same grading patterns and different W_{GNP} have been selected from the previous studies on free vibration and buckling characteristics. It is found that, the nature of edge load variation on buckling and vibro-acoustic response is significant. Free vibration mode shape changes with an increase in edge load and consequently affects the resonant amplitude of responses also especially for the plates with a higher aspect ratio. W_{GNP} and dispersion grading pattern of $GNPs$ also influences the resonance amplitudes. Plate with FG-GRC_C dispersion pattern and higher W_{GNP} has improved buckling and vibro-acoustic response behaviour. Similarly, change in sound transmission loss level is significant in the stiffness region compared to the damping and mass dominated region.

Finally, a detailed investigation of porosity grading and coefficients on vibro-acoustic characteristics of graphene reinforced nanocomposites under the different NUE loads is presented. Three types of porous distribution patterns, in which the porosity changes latterly the thickness bearing of the graphene reinforced

nanocomposites, are considered. Plates with porosity is less at the surface and more at the centre is termed as VPC (increasing porosity towards the centre). Plates with less porosity at the centre and more at the surfaces is termed as VPS (increasing porosity towards the surface) and the plate with uniform porosity is termed as UP. It is observed that, the W_{GNP} and grading pattern of $GNPs$ reinforcement causes the stiffness hardening effect, whereas porosity distribution and coefficients cause the stiffness softening effect on the graphene reinforced nanocomposite plate. It is found that the plate with symmetric distribution of $GNPs$ with more concentration at the surface and symmetric porosity variation with more porosity at the centre radiates less sound power (i.e., $FG - GRC_C^{VPC}$ with higher $W_{GNP}\%$).

TABLE OF CONTENTS

ACKNOWLEDGEMENTS	i
ABSTRACT	iii
LIST OF TABLES	xi
LIST OF FIGURES	xiii
NOMENCLATURE.....	xvii
LIST OF ABBREVIATIONS	xix
1. INTRODUCTION	1
1.1. Introduction	1
1.2. Literature Review	3
1.2.1. Effective material properties of the FG-graphene reinforced nanocomposites	3
1.2.2. Buckling response of the graphene reinforced nanocomposites.....	6
1.2.3. Vibration response of the FG-graphene reinforced nanocomposites.....	9
1.2.4. Acoustic response of the FG-graphene reinforced nanocomposites.....	11
1.3. Closure	16
1.4. Research objectives	17
2. METHODOLOGY AND VALIDATION STUDIES	19
2.2. Methodology for analytical studies	19
2.2.1. Material modelling.....	19
2.2.2. Buckling load calculation for FG-graphene reinforced nanocomposites 24	
2.2.3. Buckling mode shape calculation	26
2.2.4. Free vibration response for FG-graphene reinforced nanocomposites ..	27
2.2.5. Forced vibration and sound radiation response for FG-graphene reinforced nanocomposites	29
2.3. Validation for analytical studies.....	33
2.3.1. Buckling load validation	33
2.3.2. Vibration frequencies validation.....	34
2.3.3. Validation of acoustic response	35

2.4. Closure	36
3. VIBRO-ACOUSTIC STUDIES OF ISOTROPIC PANEL UNDER NON-UNIFORM UNIAXIAL EDGE LOADS.....	37
3.1. Introduction	37
3.2. Buckling characteristics of isotropic plate	37
3.3. Vibration response of the isotropic plate.....	38
3.3.1. Free vibration characteristics of the isotropic plate	38
3.3.2. Forced vibration characteristics	41
3.4. Sound radiation characteristics.....	45
3.5. Sound transmission loss characteristics	52
3.6. Closure	55
4. BUCKLING AND FREE VIBRATION STUDIES OF FG-GRC PANEL UNDER NON-UNIFORM UNIAXIAL EDGE LOADS	57
4.1. Introduction	57
4.2. Investigation on buckling characteristics of the FG-GRC plate	58
4.2.1. Effect of <i>GNPs</i> pattern and weight fraction on FG-GRC plate under NUE load	58
4.2.2. Effect of aspect ratio (a/b), <i>GNPs</i> pattern and weight fraction on dimensionless buckling load.....	60
4.2.3. Effect of width to thickness ratio (b/h) on dimensionless buckling load	63
4.3. Investigation on free vibration behaviour of the FG-GRC plate.....	64
4.3.1. Free vibration behaviour of the FG-GRC plate under NUE load	64
4.3.2. Effect of <i>GNPs</i> pattern and weight fraction on dimensionless natural frequency	66
4.3.3. Effect of width to thickness ratio (b/h) on dimensionless natural frequency	70
4.4. Closure	71
5. VIBRO-ACOUSTIC STUDIES OF FG-GRC PANEL UNDER NON-UNIFORM UNIAXIAL EDGE LOADS.....	73
5.1. Introduction	73
5.2. Investigation of <i>GNPs</i> grading and weight fraction under no load condition	74
5.3. Buckling response of FG-GRC plate under NUE load	75

5.4.	Vibration response of FG-GRC plate under NUE load.....	77
5.4.1.	Free vibration characteristics	77
5.4.2.	Forced vibration characteristics	81
5.5.	Sound radiation characteristics.....	83
5.6.	Sound transmission loss characteristics	90
5.7.	Closure	92
6.	VIBRO-ACOUSTIC STUDIES OF POROUS FG-GRC PANEL UNDER NON-UNIFORM UNIAXIAL EDGE LOADS	95
6.1.	Introduction	95
6.2.	Buckling response	96
6.3.	Vibration response.....	99
6.3.1.	Free vibration characteristics	99
6.3.2.	Forced vibration characteristics	102
6.4.	Sound radiation characteristics.....	105
6.5.	Sound transmission loss characteristics	112
6.6.	Closure	114
7.	SUMMARY AND CONCLUSIONS.....	115
7.1.	Summary	115
7.2.	Conclusions	116
7.2.1.	Studies of the isotropic plate.....	116
7.2.2.	Free vibration studies of FG-GRC plate	117
7.2.3.	Vibro-acoustic studies of FG-GRC plate.....	117
7.2.4.	Vibro-acoustic study of porous FG-GRC plate	118
7.3.	Scope for Future Research	119
	Appendix A. Different Coefficients of [K] and [M] are given as	120

LIST OF TABLES

2.1	Porosity coefficients for different porous grading of porous FG-GRC plate.	22
2.2	FG-graphene reinforced nanocomposites panel properties.	24
2.3	Comparison of critical buckling change (%) result with Thai <i>et al.</i> (2019).	34
2.4	Validation of dimensionless buckling load results with Yang <i>et al.</i> (2018).	34
2.5	Validation of dimensionless natural frequencies (Eq. (2.46)) results with Xu <i>et al.</i> (2019).	35
2.6	Validation of dimensionless natural frequencies (Eq. (2.47)) results with Yang <i>et al.</i> (2018).	35
3.1	Buckling coefficient and buckling load ratio for different types of loading for isotropic plate.	38
3.2	Variations on the natural frequencies of the isotropic plate with increase in non-uniform load intensity.	41
3.3	Variations on the forced vibration response peaks of the isotropic plate with increase in non-uniform load intensity.	42
3.4	Variations on the sound power level peaks of the isotropic plate with increase in non-uniform load intensity.	47
4.1	Buckling load ratio of FG-GRC plate under NUE loads.	58
4.2	Dimensionless buckling load of FG-GRC plate under NUE load.	59
5.1	Buckling load ratio of FG-GRC plate under NUE loads.	73
5.2	Dimensionless buckling load of FG-graphene reinforced plate.	76
6.1	Buckling load ratio of porous FG-GRC under NUE loads.	96
6.2	Dimensionless buckling load of porous FG-GRC under NUE loads.	97

LIST OF FIGURES

1.1	Structural graphene reinforced nanocomposites used in aerospace/aircraft industries: (a) outer body panels; (b) fuselage (www.materialstoday.com).	2
1.2	Schematic representation: (a) Types of external loading acts on structure; (b) Elastic buckling of a flat panel.	2
2.1	Flowchart of the detailed work process of the current thesis.	20
2.2	Types of NUE loads used in current investigation.	20
2.3	Types of porosity distribution and <i>GNPs</i> grading of FG-GRC plate used in current investigation.	21
2.4	Schematics of sound radiation analysis.	30
2.5	Schematics of sound transmission loss analysis.	32
2.6	Comparison of sound power level (<i>dB</i>) and sound transmission loss with Chandra <i>et al.</i> (2014).	36
3.1	Variation of natural frequencies with NUE loads for various edge loading cases.	40
3.2	Variation on the natural frequencies and associated mode shapes of the isotropic plate with increase in axial load intensity under $\alpha = 2$ case.	40
3.3	Effect of NUE loads on forced vibration response.	43
3.4	3D representation of effect of increase in axial load magnitude on the forced vibration response for $\alpha = 2$, <i>Case 1</i> loading.	44
3.5	Effect of NUE load on sound power level (<i>dB</i>).	46
3.6	3D representation of effect of increase in axial load magnitude on the sound power level response for $\alpha = 2$, <i>Case 1</i> loading.	47
3.7	Contour representational effect of NUE load on sound pressure level radiated.	48
3.8	Effect of different NUE load on sound power level (<i>dB</i>).	49
3.9	Effect of non-uniform loads on sound radiation efficiency.	49
3.10	Effect of non-uniform load on sound power level (<i>dB</i>) vs octave frequency band.	50

3.11	Effect of NUE load on the overall sound power level (dB).	50
3.12	Effect of NUE load on the sound directivity pattern.	51
3.13	Effect of NUE load on sound transmission loss for normal and angle incidence.	53
3.14	Effect of different NUE loads on sound transmission loss.	54
4.1	Effect of distribution pattern and weight fraction (W_{GNP}) on the FG-GRC plate under NUE load.	60
4.2	Effect of aspect ratio (a/b) on the distribution pattern of FG-GRC plate under NUE load.	61
4.3	Effect of aspect ratio (a/b) on weight fraction W_{GNP} of FG-GRC plate under NUE load.	62
4.4	Effect of NUE load on aspect ratio (a/b) vs buckling load.	63
4.5	Effect of width to thickness ratio (b/h) and functional grading on the buckling load of the FG-GRC plate.	64
4.6	Effect of width to thickness ratio (b/h) and weight fraction on the buckling load of FG-GRC _{UD} plate under NUE load case $\alpha=2$.	65
4.7	Effect of NUE load on free vibration frequencies.	65
4.8	Effect of the distribution pattern of $GNPs$ and NUE load on the fundamental natural frequency.	67
4.9	Effect of weight fraction and NUE load on the fundamental natural frequency of the FG-GRC plates.	68
4.10	Effect of type of NUE load on the fundamental natural frequency of FG-GRC plates.	69
4.11	Effect of width to thickness ratio (b/h) and functional grading on the free vibration of the FG-GRC plate.	70
4.12	Effect of width to thickness ratio (b/h), weight fraction and NUE load on the natural frequency of FG-GRC plate.	71
5.1	Effect of slenderness ratio (b/h) and weight percentage of GNP on different dispersion pattern of FG-GRC plate.	75
5.2	Effect of NUE loads on dimensionless natural frequency.	80
5.3	Effect of NUE loads on the mode shapes.	81
5.4	Effect of NUE loads on dimensionless average RMS velocity.	82

5.5	Effect of NUE loads on sound power level (<i>dB</i>).	85
5.6	Effect of <i>GNPs</i> dispersion pattern and W_{GNP} on sound power level (<i>dB</i>).	86
5.7	Effect of NUE load on sound radiation efficiency.	86
5.8	Effect of NUE loads on sound power level (<i>dB</i>) vs octave frequency band.	87
5.9	Effect of NUE loads on overall sound power level (<i>dB</i>).	87
5.10	Effect of NUE loads on directivity pattern.	88
5.11	Contour representational effect of NUE load on sound pressure level radiated.	89
5.12	Contour profile representational effect of NUE load on sound pressure level radiated at $0.99P_{cr}$.	89
5.13	Effect of NUE loads on sound transmission loss for normal and angle incidence.	91
5.14	Effect of <i>GNPs</i> dispersion pattern and W_{GNP} on sound transmission loss.	92
6.1	Effect of porosity coefficients (γ , η and η^*) on dimensional buckling load.	98
6.2	Parametric effect on dimensionless natural frequency.	100
6.3	Variation of dimensionless fundamental frequency of porous FG-GRC plate under different porosity coefficients.	101
6.4	Effect of NUE loads on the free vibration mode shapes.	101
6.5	Forced vibration response of porous FG-GRC plate under different porosity coefficients.	104
6.6	Effect of porosity coefficients on sound power level of porous FG-GRC plate.	106
6.7	Effect of different NUE load on sound power level of porous FG-GRC plate.	108
6.8	Effect of NUE loads and porosity factor on sound radiation efficiency.	108
6.9	Effect of porosity coefficient on overall sound power level (<i>dB</i>) vs octave frequency band.	109

6.10	Effect of NUE load and porosity factor on the overall sound power level (<i>dB</i>).	110
6.11	Effect of NUE load and porosity factor on directivity pattern.	110
6.12	Contour representational effect of porosity coefficient on SPL radiated.	111
6.13	Effect of porosity coefficients on sound transmission loss of porous FG-GRC plate.	113
6.14	Effect of different NUE load on sound transmission loss of porous FG-GRC plate.	113

NOMENCLATURE

- k : acoustic wave number.
- ω : angular frequency.
- m and n : are the half wave number of the plate in x and y direction, respectively.
- $\dot{w}^*(r_s)$: complex conjugate of normal velocity.
- $p(r)$: complex pressure amplitude.
- ρ_o : density of the medium (kg/m^3).
- ρ^* : density of the non-porous FG-GRC plate.
- u, v and w : displacement along x, y and z axes, respectively.
- $|r - r_s|$: distance among the surface and the field.
- W_{ref} : equal to 10^{-12} watts.
- p_o : harmonic point load with the unit amplitude (N).
- N_o : highest force value in the variation.
- θ_{inc} and ϕ_{inc} : incidence angle of the sound pressure wave.
- a_{GNP}, b_{GNP} and h_{GNP} : length, width and thickness of solitary graphene nanolayer, respectively.
- $[M]$: mass matrix of nanocomposite plate.
- ma : matrix material
- u_o, v_o and w_o : mid-plane displacement of x, y and z axes, respectively.
- $\dot{w}(r_s)$: normal particle velocity at the surface location.
- α : parameter used to define particular NUE loads.
- γ : porosity coefficient of UP case.
- η : porosity coefficient of VPC case.
- η^* : porosity coefficient of VPS case.
- ϕ_y and ϕ_x : rotations about x and y axes, respectively.
- G^* : shear modulus of the non-porous FG-GRC plate.
- c_o : speed of sound (ms^{-1}).
- V_m and V_b : strain and kinetic energy of the plate, respectively.
- $[K]$: structural stiffness matrix of nanocomposite plate.

- $n(r_s)$: surface normal.
- $\langle \bar{W}^2 \rangle$: time average velocity square.
- p_{inc} : unit incident sound pressure (N/m²).
- u_{mn} , v_{mn} and w_{mn} : unknown displacement coefficients with the respective coordinates.
- ϕ_{xmn} and ϕ_{ymn} : unknown rotational coefficients with the respective coordinates.
- δ and t : variational operator and time period value, respectively.
- T : work done by external mechanical forces.
- E^* : Young's modulus of the non-porous FG-GRC plate.

LIST OF ABBREVIATIONS

- 2 D : 2 dimensional.
- 3 D : 3 dimensional.
- BEM : boundary element method.
- BLR* : buckling load ratio.
- CNT : carbon nanotubes.
- FEM : finite element method.
- FSDT : first-order shear deformation theory.
- FG-GRC : functionally graded graphene reinforced nanocomposites.
- GNP* : graphene nanoplates.
- HSDT : higher-order shear deformation theory.
- IMLS : improved moving least-square.
- NURBS : non-uniform rational basis spline.
- NUE : non-uniform uniaxial edge.
- TSDT : third-order shear deformation theory.
- UD : uniform distribution.

CHAPTER 1

1. INTRODUCTION

1.1.Introduction

Thin walled or slender panel members are used as structural components in aerospace vehicles, civil and oceanic applications. Recently graphene nanoplates (*GNP*) and carbon nanotubes (*CNTs*) based nano-reinforcements are commonly used in functionally graded carbon-reinforced nanocomposites (FG-GRC and porous FG-GRC), which obtains a huge interest in structural scientific community due to their remarkable performance. These nanocomposites are characterized as inhomogeneous in nature where the elastic properties vary along the thickness direction to achieve the desired property. Restrictive factors like achievement of uniform dispersion and high manufacturing cost associated with *CNT* based composites makes it very difficult to fabricate such composites through the general manufacturing processes. However, graphene gains superior properties in terms of uniform dispersion in a polymer matrix, mechanical (Rafiee et al. (2009)), electrical (Novoselov et al. (2004)), energy storage (Bonaccorso et al. (2015)) and low manufacturing cost. Due to this graphene emerges as an ultimate reinforcement for obtaining high stiffness and stress in structural nanocomposite applications (Tiwari et al. (2015)). Since the panel gives good weight reduction and high increase in stiffness properties, which will be in favourable of offering superior mechanical properties when compared to traditional metallic structures during their life service. Due to these advantages, nanocomposite constructions are used in many aerospace structures for the weight reduction and good acoustical properties which are important factors to be considered during the design process along with high stiffness and strength.

Hence the graphene reinforced nanocomposite panels can be implemented in the aerospace structures (Rafiee *et al.* (2009)) as shown in Figure 1.1 for their high stiffness to the low weight ratio property with the superior mechanical strength. During the in-flight conditions these structures are subjected to the arbitrary in-plane compression edge loads and transverse static/dynamic mechanical loadings (Figure

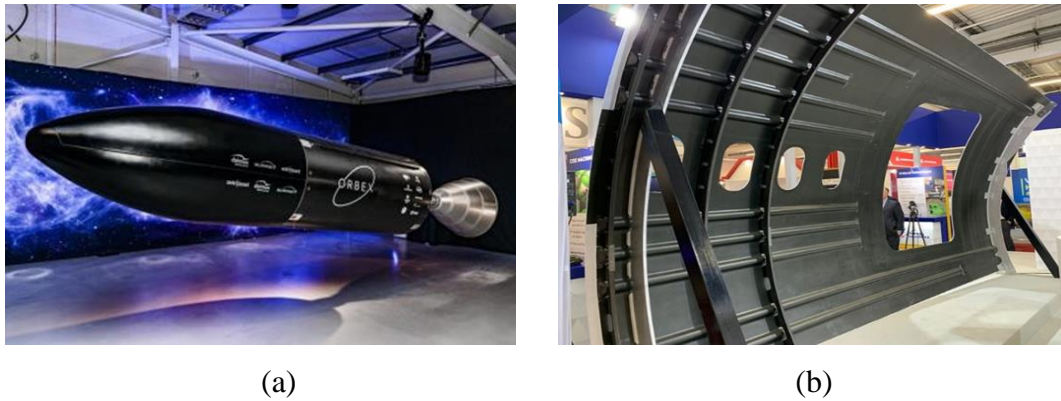


Figure 1.1: Structural graphene reinforced nanocomposites used in aerospace/aircraft industries: (a) outer body panels; (b) fuselage (www.materialstoday.com).

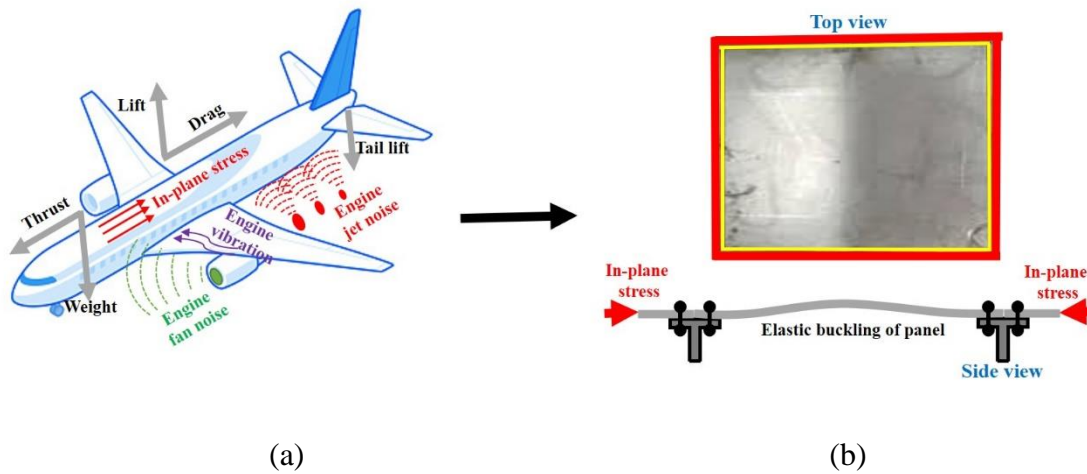


Figure 1.2: Schematic representation: (a) Types of external loading acts on structure; (b) Elastic buckling of a flat panel.

1.2 (a)), which causes the change in structural stiffness of the FG-GRC plate. As a result, buckling and dynamic instability occurs, which trends to the sudden failure of the structural members and significant change in vibro-acoustic response characteristics. So, monitoring the vibro-acoustic response like sound radiation and sound transmission loss (i.e., acoustic comfort) of the graphene reinforced nanocomposite structure under the non-uniform in-plane compressive loading condition is still a motivating topic.

Non-uniform compressive stress loads can be observed in the typical structural components such as walls, floor, stiffener... etc., area of space launcher vehicle or aircrafts, which are extensively made-up of nanocomposites. During the in-flight conditions these structures experience symmetric or asymmetric stress resultant acts

as compressive and tensile in-plane stresses (Figure 1.2 (b)). These axial stresses are equivalent to the non-uniform uniaxial edge (NUE) loads and this pre-stress will influence the dynamic characteristics of the nanocomposite structure subjected to transverse harmonic mechanical excitation. So, it is crucial to analyse dynamic and acoustic response of structure subjected to NUE loads subjected to steady-state mechanical excitation for the better design consideration.

1.2.Literature Review

A brief literature study on the homogenization method to obtain the effective material properties, buckling, free/forced vibration and sound radiation/transmission loss characteristics of the graphene reinforced nanocomposites panels are given out in detail in following sections.

1.2.1.Effective material properties of the FG-graphene reinforced nanocomposites

In general, an analytical homogenization theory is used to predict the elastic properties of graphene reinforced nanocomposites to a continuum thin orthotropic plate. Then the geometrically complex graphene reinforced nanocomposites are covered into a simple 2D orthotropic plate with the equivalent material properties for the analytical investigation. Several research works are published on obtaining effective stiffness properties of different types of graphene reinforced nanocomposites structures are grouped in this section.

Affdl and Kardos (1976) have benchmarked a micro-mechanic's mathematical model to calculate the elasticity constants for the various type of reinforced composites by introducing Halpin-Tsai equations, which forms the basis to model the different types of nanocomposites analytically.

Choi and Lakes (1995) performed both analytical modelling and experiments to obtain elastic moduli of conventional cell foam and open-cell foam materials of negative Poisson's ratio. Their analytical results are closely matching with the experimental data.

Gibson and Ashby (1999) have done a detailed general material characterization, structural design, acoustic properties, and mechanics of three-dimensional cellular material.

Ashby *et al.* (2000) have benchmarked the processing, characterization, mechanical properties, design formulation, and other structural characterization of metal foams.

Roberts and Garboczi (2001) derived the theoretical formulation to predict the effective material properties of closed-cell cellular structure by using Voronoi tessellation and level-cut Gaussian random fields. They presented material properties of closed-cell cellular materials, and the properties are found to be in good agreement with experimental data.

Novoselov *et al.* (2004) investigated the electric properties of monocrystalline graphitic films, which are stable under the ambient conditions. They concluded that graphitic films exhibit a strong ambipolar electric field which is in favour of conducting electricity.

Yasmin and Daniel (2004) have done a detailed experimental investigation to estimate the mechanical properties of graphite/epoxy nanocomposite material. The composites showed higher thermal stability in comparison with pure epoxy and they observed increased char concentration for higher amount of graphene reinforcements.

Wicklein and Thoma (2005) proposed a numerical method to study the elastic behaviour of open-cell aluminium foam and shown the effect of porosity grading pattern and distribution pattern.

De Villoria and Miravete (2007) carried out experimental study on the dispersion properties of nano reinforcement and also implemented the micromechanical model to predict the mechanical properties of nanocomposites. Their study highlighted that *CNT* reinforcement has poor dispersion properties compared to *GNP* reinforcement.

Rafiee *et al.* (2009) have done a detailed comparison study on nanocomposites with graphene and carbon nanotube as the reinforcements. The result highlights the superiority of graphene reinforcement over the *CNT*, Young's modulus of graphene

reinforced structure possesses 31% high when compare to neat epoxy, 3%, and 14% increase when compared to single and multi-walled *CNT* respectively.

Bakshi (2010) done a detailed review work on *CNT* metal matrix composites, which highlights the processing techniques, strengthening mechanism, mechanical properties, and nanotube dispersion. Similarly, Jagannadham (2012) investigated changes in the thermal conductivity of graphene-copper composite, for the different dimensional parameters experimentally.

Hangai *et al.* (2012) investigated functionally graded aluminium foam using X-ray tomography, to show the porosity variation at different regions of metal foam structures.

Zaman *et al.* (2012) extensively studied the effects of graphene reinforcements on the polymer-based nanocomposites and noted that graphene reinforcements exhibit high mechanical performance, electrical and thermal conductivities. They concluded that graphene would replace *CNT* for many applications of nanocomposites.

Bonaccorso *et al.* (2015) studied the impact of the integration of *GNPs* reinforcement on practical applications and explained the advantage of the 2-D crystal structure of graphene, for the possibility of designing layer by layer assembly of a new artificial structure by exploiting the current exciting traditional structure.

Tiwari *et al.* (2015) done a detailed literature study on fundamental aspects of graphene materials and its emerging applications with detailed processing, properties and technology developments of graphene materials including multifunction graphene sheet, surface functionalization and reinforced nanoplatelets composite etc., for wide range of applications.

King *et al.* (2015) experimentally examined the influence of weight fraction (1 - 6%) of graphene platelets content on the aerospace graded epoxy and shown that tensile strength increases from 2.72 GPa of plain epoxy to 3.35 GPa of an xGnP-M-5/epoxy composite.

Li *et al.* (2016) experimentally investigated the effect of spatial orientation of nanoplatelets reinforcement on properties of nanocomposites with the help of

Krenchel orientation factor from the Raman data. They estimated the effective Young's modulus of the reinforcement in graphene-based nanocomposites.

Koohbor and Kidane (2016) optimized the porosity gradient and distribution of Functionally graded foam using an analytical study for energy absorption characteristics and observed that the analytical results are closely matching with the experimental results.

Lin *et al.* (2017) used molecular dynamics simulation to study graphene/polymer composites and shown that tensile strength increases with increases number of graphene layers (*GNPs*).

Sun *et al.* (2018) studied on design, fabrication and characterization of multi-layer graphene reinforced nanostructure, highlighted that predesigned cobalt gradient can maximally enhance the stability, surface compressive stress and the mechanical properties of nano-composites.

Zhao *et al.* (2020) done a detailed literature study on fabrication, micromechanics models to predict effective mechanical properties and mechanical analyses of graphene reinforced nanocomposite structures is presented

Above comprehensive literature study clears that, effective material properties of graphene reinforced nanocomposites (i.e., FG-GRC and porous FG-GRC) can be calculated analytically for predicting the buckling and dynamic responses.

1.2.2. Buckling response of the graphene reinforced nanocomposites

Several research works are published on the buckling analysis of different types of graphene reinforced nanocomposite structures under non-uniform edge loads are grouped in this section.

Lessia (1986) presented an accurate solution method for the laminated plates under the varying edgewise compressive loads by implementing analytical methods and highlighted those types of load configuration has a significant influence in buckling strength.

Baker *et al.* (1993) have benchmarked the Mathieu's approach for the arbitrary edgewise compressive force into modest fundamental stress problems, by obtaining the exact analytical solution for the elasticity problem as a stress input factor.

Bert and Devarakonda (2003) examined the buckling characteristics of Kirchhoff plate under the simply supported condition subjected to non-uniform edge stress using Galerkin's method.

Kang and Lessia (2005) expressed the accurate solution method for the buckling study of simply supported isotropic plate subjected to the linearly varying load using the method of Frobenius.

Jones (2006) and Timoshenko *et al.* (2009) analysed the buckling of the rectangular plate under non-uniform edge loadings using analytical method to obtain the precise buckling strength.

Zhong and Gu (2006) studied the impact of load intensity/configurations on the buckling strength of simply supported plate subjected to non-uniform edge load by using formulation based on FSDT (First-order shear deformation theory) method.

Rafiee *et al.* (2009) experimentally investigated buckling of graphene reinforced epoxy nanocomposites and observed a remarkable increase in the critical buckling load for the addition of 0.01 wt.% of graphene platelets. They also highlighted the futuristic use of this material in space and aeronautical application areas due to high buckling resistant and lightweight.

Mijuskovic *et al.* (2014) have derived analytical results for the buckling load, under the arbitrary in-plane load with the variable boundary condition by using Ritz energy method and highlighted that types load configuration has a significant influence in buckling strength.

Shen *et al.* (2017) did an analytical investigation on buckling performance of the FG-Graphene reinforced structure subjected to the thermal environment along with the compression loads and shown that buckling characteristics can be improved by varying distribution pattern of *GNPs*.

Song *et al.* (2017) carried out an analytical study on buckling characteristics of FG-GRC structures with the help of a formulation based on FSDT and noted that minute increment in weight fraction of graphene reinforcement increases the buckling strength significantly.

Mirzaei and Kiani (2017) analysed theoretically the buckling characteristics of FG-Graphene reinforced plate subjected to thermal environment based on the NURBS formulation, with the temperature-dependent material properties.

Wu *et al.* (2017(a) - 2017(b)) presented the analytical solution for buckling characteristics of FG-Graphene reinforced composites and also demonstrated that dispersion of a greater number of *GNPs* towards the outer surface of the FG-GRC plate results in significant improvement in buckling strength.

Wu *et al.* (2017) established the theoretical formulae for the FG-Graphene reinforced beam under the thermal load, Bolotin's method is employed to determine the buckling behaviour. It is shown that more amount of *GNPs* distribution towards the outer surface area, effectively increases natural frequencies.

Wu *et al.* (2018) studied the instability of the FG-GRC plate under the periodic uniaxial force and thermal load using an analytical approach. Similar to their earlier study, they demonstrated that the distribution of more *GNPs* near the top and bottom surface can significantly increase the natural frequency and buckling strength.

Akbas (2017) analytically studied the stability of non-homogeneous porous plate under the in-plane loads by using the differential quadrature method, to highlight the influence of nature of porosity distribution on the buckling strength.

Song *et al.* (2018) employed the Halpin- Tsai approach to determine mechanical properties of FG-GRC plate then examined the bending and buckling behaviour of the FG-Graphene reinforced composite plate by using the Navier solution technique.

Wang and Zhang (2019) analytically studied the instability characteristics of porous graphene foam structure and highlighted the effects of porous distribution on the buckling strength, with the help of two variable refined plate theory.

Moita *et al.* (2020) did a detailed analytical study on buckling behaviour of FGM plate subjected to uniform mechanical and thermal load using finite element method (FEM).

Phan (2020) used iso-geometric method for the analysis of porous graphene reinforced nanocomposites with the help of refined plate theory and implemented Newmark's time integration scheme for calculating forced vibration response.

Above comprehensive literature study clears that, graphene reinforced nanocomposites (i.e., FG-GRC and porous FG-GRC) can be analysed analytically for its buckling behaviour under non-uniform uniaxial edge loads by finding the effective stiffness properties analytically.

1.2.3. Vibration response of the FG-graphene reinforced nanocomposites

Several research studies related to the vibration response of different types of graphene reinforced nanocomposites structures are grouped in this section.

Lessia and Kang (2001), Kang and Lessia (2001) using Frobenius analytical method studied the effects of compressive load on the free vibrational features of the plate with simply supported edges, subjected to a linearly varying load and noted that increase in load results in the shift of natural frequencies towards zero.

Liew *et al.* (2004) examined the vibration and buckling characteristics of isotropic plate using a mesh-free method formulated based on FSDT (First-order shear deformation theory) and compared the results with the numerical solutions.

Reddy (2006) analysed the dynamic behaviour of isotropic/orthotropic plate under various boundary conditions using Hamilton's principle method considering various shear deformation theories.

Ferreira *et al.* (2011) numerically examined buckling and free vibration of isotropic/laminated plate using collocation approach with radial basis function and obtained highly accurate buckling load and natural frequencies.

Chandra *et al.* (2012) done a detailed numerical investigation on the dynamic analysis of graphene/polymer composites by implementing continuum FEM. They explained

that natural frequencies and mode shapes have a significant dependence on the physical dimension of the graphene and structural boundary conditions.

Jeyaraj (2013) has done a detailed numerical study on buckling strength and dynamic response of metal plate by using the FEM approach, to show the instability of the nodal and anti-nodal lines when the plate subjected to high temperature.

Neves *et al.* (2013) used numerical method developed using quasi-3D HSDT (Higher-order shear deformation theory) to analyse deflection, stresses, free vibration and buckling characteristics of a simply supported isotropic and functionally graded sandwich plates.

Song *et al.* (2017) formulated analytical solutions for the dynamic behaviour of the FG-GRC plate, based on Reddy's HSDT. Different studies have been carried out to analyse the effects of graphene distribution, weight fraction, physical dimension and the total number of the layer on the dynamic behaviour of the plate.

Garcia-Macias *et al.* (2018) investigated the bending and vibrational behaviour of FG-GRC and FG-CNT plates and highlighted the superior property of graphene as reinforcement, dispersion and low-cost manufacturing over carbon nanotubes.

Guo *et al.* (2018) analysed the vibration characteristics of FG-Graphene reinforced quadrilateral plates with the help of element-free IMLS-Ritz method and shown that *GNPs* distribution and weight fraction affects the natural frequencies.

Arefi *et al.* (2018) carried out analytical study on vibration behaviour of FG-Graphene reinforced plate resting on the elastic foundation. Effect of *GNPs* dispersion pattern on natural frequencies of plate has been investigated based on nonlocal elasticity theory.

Reddy *et al.* (2018) numerically studied the vibration behaviour of moderately thick FG-GRC plates by using finite element method based on FSDT and analysed the effect of weight percentage of graphene nanolayer, geometry and size of *GNPs* on the vibration characteristics.

Yang *et al.* (2018) theoretically studied effects of *GNPs* grading pattern and porosity distribution on the dynamic and instability characteristics of porous graphene

reinforced plate based on the FSDT and Chebyshev-Ritz method shown that minute increase in W_{GNP} has a significant increase in natural frequencies.

Ramteke *et al.* (2019) carried out a detailed analytical study of dynamic behaviour of porous FGM structure by varying grading pattern and porosity with the help of higher order shear deformation model. Natural frequencies are affected significantly by the grading pattern and types of porosity distribution.

Thai *et al.* (2019) studied the dynamic and buckling characteristics of FG-Graphene reinforced structure with different dispersion pattern and weight percentage of *GNPs* based on NURB formulation. Their results shown that *GNPs* grading, weight percentage and no of layers has a huge shift in changing the dynamic behaviour of the plate.

Phung Van *et al.* (2019) analytically studied the porosity effect on free vibration response of FG-nanoplates by using Iso-geometric analysis and results show that the porosity has huge influence in the vibration response.

Chen *et al.* (2020) analytically done a detailed free vibration study of varying cross-sectional of graphene reinforced composites blades, by establishing FSDT and von Karman theory. A comprehensive parametric study is conducted, with a particular focus on the effects of distribution pattern, weight fraction, and geometries size of the *GNPs* together with dimensional parameters of varying cross-sections blade.

Above comprehensive literature study clears that, graphene reinforced nanocomposites (i.e., FG-GRC and porous FG-GRC) can be analytically modelled for its buckling behaviour under non-uniform uniaxial edge loads and find variations in vibration behaviour by finding the effective stiffness properties analytically.

1.2.4. Acoustic response of the FG-graphene reinforced nanocomposites

Several research works related to acoustic response studies of plates made of different types of materials are grouped in this section.

Rayleigh (1896) derived the first comprehensive and systematic mathematical formulation to predict the acoustics problems for a given phenomenon. His acoustical

system in theory of sound aimed at general vibrations and waves, and they could be easily applied to other problems.

Fuller (1990) analytically studied the sound radiation of vibrating plates subjected to the direct oscillating forces and demonstrated that the radiation efficiency is influenced by the nature of coupling between the plate modes of response and radiated field.

Kirkup (1994) was the first to benchmark the Rayleigh integral method for predicting the acoustic field of the baffled vibrating panel. He also shown that the Rayleigh integral approach is a superior computational model and simple method to calculate the acoustic field of flat panels.

Fhay and Gardonio (2007) described procedure for the structural vibration, acoustic fields related to sound radiation and transmission loss analysis using the numerical analysis and also discussed different issues associated with the computational aspects.

Assaf and Guerich (2008) numerically analysed the transmission loss characteristics of the sandwich structure subjected to acoustic plane waves by using combined finite and boundary element methods.

Mellert *et al.* (2008) investigated the consequence of noise and vibration on health of flight attendants and pilots at their workplace (cabin and cockpit) and show the importance of sound quality (sound level) for work environments during the long-haul flights.

Li and Li (2008) investigated analytically the impact of disseminated mass loading on the acoustical radiation behaviour of an isotropic plate in both air and liquid medium and concluded that the acoustical characteristics charges at a high rate with respective medium.

Jeyaraj *et al.* (2009) presented numerical investigation on vibro-acoustic behaviour of fibre reinforced composite plate subjected to the thermal load with consideration of inherent material damping and shown that increase of thermal load results in decrease of vibration response. Also, Jeyaraj (2010) numerically investigated vibro-acoustic characteristics of an isotropic plate with different taper configurations by combining

FEM and BEM and found that nature of taper and excitation location of the harmonic force has significant influence on the vibro-acoustic response.

Thompson *et al.* (2009) done a detailed study on sound transmission loss through isotropic panels based on the infinite panel assumed and highlighted that transmission coefficients greater than unity should not necessarily be seen as error in calculation.

Khorshidi (2011) derived a dimensionless equation of motion based on FSDT to obtain the transverse dynamic and acoustic radiation characterization of a metal plate with altered boundary conditions. The influence of boundary conditions, types of loads, aspect ratio and thickness on sound radiation has been explained in detail.

Geng and Li (2012) carried out experimental and numerical studies on vibro-acoustic response of clamped rectangular plate under mechanical and acoustic excitations and observed that increase in thermal load reduces the natural frequencies of the structure and also leads to mode interchanging behaviour.

D'Alessandro *et al.* (2013) done a detailed review work on the vibro-acoustics behavior of sandwich panel through numerical modelling and experiment. Their work mainly focused on predicting and validating the prominent sound transmission model and the results shows nearby matching of both numerical and experimental approach.

Petrone *et al.* (2014) numerically and experimentally investigated the sound radiation characteristics of aluminium foam sandwich panels by using FEM approach and validated their numerical model with the experimental results obtained using sound intensity probe technique.

Chandra *et al.* (2014) examined analytically vibro-acoustical behaviour of the metal ceramic functionally graded plates by following FSDT and shown that sound power level decrease by increasing power-law index.

Geng *et al.* (2014) investigated both experimentally and numerically the vibroacoustic performance of a metal plate subjected to the thermal load. The plate is excited by both mechanical and acoustical excitations and vibration and acoustic responses are investigated. They clearly shown that the increase in thermal loading leads to decrease in the natural frequency.

Arunkumar *et al.* (2016) investigated the vibro-acoustics behaviour of the aerospace sandwich plate using 2D equivalent models through finite element model for vibration response and Rayleigh integral method for predicting acoustic characteristics.

Yang *et al.* (2016) analytically investigated the sound radiation response of metal ceramic functionally graded plate considering three-dimensional elasticity solution and Rayleigh integral approach. They highlighted the influence of various load types such as material distribution, temperature increases and temperature fields on the sound radiation response of the plate.

George *et al.* (2018) numerically examined the vibro-acoustic behaviour of FG-CNT plate using combined FEM and Rayleigh integral approach. Their results shown that vibro-acoustic response of plate is significantly influenced by the graded dispersion patterns of the *CNTs*. However, the free vibration mode shapes of the plate are not sensitive to the nature of dispersion pattern.

Sharma *et al.* (2018) numerically studied the vibro-acoustic behaviour of flat laminated composite panel under different boundary conditions by using combined FEM/BEM method. They highlight the effects of thermal loading, aspect ratio, slenderness and lay-up scheme on the sound radiation characteristics.

Zhang *et al.* (2018) proposed the vibro-acoustic coupling model to investigate the sound radiation behaviour of the structure under different elastic boundary conditions and impedance wall boundary conditions.

Sarigul and Karagozlu (2018) by using FEM investigated the vibro-acoustic coupling analysis of the composite plate and shown that the plate behaviour has a significant effect on material, ply orientation and number of layers.

Talebitooti and Zarastvand (2018) presented an analytical model developed based on the HSDT to investigate the sound transmission loss characteristics of the composite structure.

Arunkumar *et al.* (2018) numerically examined the dynamic behaviour of aerospace sandwich structure by using combined FEM/BEM approach. Their results revealed

that foam filled panel significantly reduces the resonant amplitude in both sound radiation and sound transmission loss characteristics.

Xu and Huang (2019) examined the acoustic response of the FG-GRC plate subjected to the thermo-mechanical environment through the analytical solution by following Reddy's TSDT and Rayleigh integral. Their results have shown, that the distribution pattern and low content of graphene has a major effect on vibro-acoustic behaviour.

Zhou *et al.* (2019) analytically studied the impact of thermal load on the behaviour of porous functionally graded material and observed that thermal load and graphene reinforcements has significant effect on the dynamic and sound radiation characteristics.

Natarajan and Padmanabhan (2019) proposed a better semi-analytical method to predict the acoustic characteristics of interior acoustic problems by implementing the scaled boundary finite element method.

Li and Yang (2020) numerically investigated the vibro-acoustic behaviour of annular cellular structures made of meta-material with the negative Poisson's ratios by using spectral element method. They found that the graded configurations have more potential than the conventional ones for optimal acoustic performance.

Above comprehensive literature study clears that, graphene reinforced nanocomposites (i.e., FG-GRC and porous FG-GRC) can be analytically/numerically analysed for its buckling behaviour under axial loads. Similarly, the vibration and acoustical response characteristics of the panels made of FG-GRC and porous FG-GRC materials, subjected to mechanical harmonic force excitations, can be studied using the numerical/analytical methods successfully.

In the present thesis, an analytical method is adopted to analyze the dynamic and acoustic response of graphene reinforced nanocomposites under the non-uniform uniaxial edge loads. To avoid expensive and time-consuming process of experimental and numerical methods, a prominent analytical method is chosen. The effective material properties of graphene reinforced nanocomposites with different grading pattern/weight fraction of graphene nanoplates (*GNP*) are obtained by grouping of

modified Halpin-Tsai model (Affdl and Kardos (1976)) and rule of mixture (Villoria and Miravete (2007)). In order to model the porous graphene reinforced nanocomposites, closed-cell cellular solids under Gaussian Random Field (*GRF*) are used (Roberts and Garboczi (2001)). An analytical method based on the strain energy (Jones (2006)) approach is used to calculate the buckling load. Free and forced vibration responses of the plate are obtained using an analytical method based on Reddy's third-order shear deformation theorem (TSDT) (Reddy (2006)) while acoustic behaviour is analysed using Rayleigh Integral (Rayleigh (1945)).

1.3. Closure

From the above comprehensive literature review, it is evident that the graphene reinforced nanocomposites (i.e., FG-GRC and porous FG-GRC) are implemented in the aerospace industries (Rafiee *et al.* (2009), Zhao *et al.* (2020)) for their superior mechanical properties along with the light weight in nature (Zaman *et al.* (2012), King *et al.* (2015)). Furthermore, reduction of vibration and noise of these structures on the aerospace industries is still considered as an important design consideration for avoiding acoustic discomfort of passengers and resonance of the inner structural components. So, it is evident that to understand the influence of non-uniform uniaxial edge loads, *GNPs* grading/weight fraction and porosity grading/coefficients on the dynamic and acoustic characteristics of graphene reinforced nanocomposites subjected to steady-state mechanical excitation and acoustic waves for the better design consideration. Anticipating acoustic characteristics of graphene reinforced nanocomposite through 3D modelling and experimental, is still a time consuming and expensive procedure. Literature survey subjected that complex 3D structure of graphene reinforced nanocomposites can be analytically modelled into a simple 2D continuum orthotropic plate and also highlights those *GNPs* reinforcements and porosity have significant effects on the stiffness of the nanocomposites plate. So detailed investigation on acoustic characteristics of different kind of graphene reinforced nanocomposites under the influence of non-uniform in-plane edge loads has to be done.

1.4. Research objectives

Challenge of making a structure, as light as possible without sacrificing the sufficient strength and stiffness requirement is the required fundamental approach in the aerospace component design. Unavoidably, this obligation leads to the need to stabilize thin-walled structures to withstand both tensile and compressive loads in the most of the conditions. Since the graphene reinforced nanocomposite structure has a capability of having superior mechanical properties (Raffiee *et al.* (2009), King *et al.* (2015)) like having high strength to weight ratio makes them as an excellent replacement instead of traditional materials. Due to this, the nanocomposite structure has been widely used in several applications (Zhao *et al.* (2020)) ranging from satellites, aircraft, ships, automobiles etc., These panels are used as body panels of floor, ceiling and partition walls due to capability of acting as insulating material for sound proof. When these structural nanocomposite panels are subjected to the in-plane compression load, the structural stiffness changes significantly which in turn to changes dynamic characteristics of the structure.

So, it is important to investigate in detail about the influence of different design parameters associated with nanocomposite panels under the non-uniform uniaxial edge (NUE) loads on the buckling and vibro-acoustic characteristics of the graphene reinforced nanocomposite panels. The main objectives of the proposed analytical investigation are

- To analyze the buckling and vibro-acoustic response behavior of isotropic panel subjected to the different types of NUE loads.
- To investigate the buckling and free vibration characteristics of different FG-GRC panels under the influence of NUE loads.
- To investigate the influence of grading pattern and weight fraction of *GNPs* reinforcement on sound radiation and sound transmission characteristics of FG-GRC panel under the NUE loads.

- To investigate the influence of porosity grading pattern and coefficients on sound radiation and transmission loss characteristics of porous FG-GRC panels under the NUE loads.

In the current investigation, graphene reinforced nanocomposite panel used in aerospace application are specifically considered. The types of panels considered in the present are; for graphene grading pattern (a) uniform graphene grading (i.e., benchmark case), (b) linear X graphene grading, (c) linear O graphene grading and (d) parabolic C graphene grading. Whereas for porosity distribution grading pattern; (a) uniform distribution, (b) varying towards center and (c) varying towards surface as shown in Figure 2.1. In this thesis, the buckling, vibration and acoustic response of graphene reinforced nanocomposites are calculated from the theoretical homogenization model (i.e., 2D orthotropic continuum plate). So, in the introduction part of each chapter, corresponding equivalent properties of graphene reinforced nanocomposite are explained and followed by results and discussions, finally, conclusion are presented about the important outcomes of the research work. Different analysis of the current research work is explained in the following sections.

Chapter 2, deals with solution methodology and validation studies for material modelling, buckling, free and forced vibration, sound radiation and transmission loss analysis of graphene nanocomposites.

Chapter 3, focuses on in-depth investigation of the buckling and acoustic behavior of isotropic panel subjected to the non-uniform uniaxial edge loads.

Chapter 4, presents the investigation of buckling and free vibration characteristics of different FG-GRC panels under the non-uniform uniaxial edge loads.

Chapter 5, provides the investigation of sound radiation and sound transmission characteristics of FG-GRC panel under the non-uniform uniaxial edge loads.

Chapter 6, describes the investigation of sound radiation and sound transmission characteristics of porous FG-GRC panel under the non-uniform uniaxial edge loads.

In Chapter 7, important findings and conclusions are summarized.

CHAPTER 2

2. METHODOLOGY AND VALIDATION STUDIES

2.1. Introduction

In this section, methodology used to compute the buckling, vibration and acoustic responses of FG-graphene reinforced nanocomposites by using analytical approach is presented. In order to ensure the accuracy of the analytical results obtained from the proposed analytical approach, a brief validation studies are also presented. By using homogenization technique (i.e., theoretically modelled 2D continuum orthotropic plate of FG-graphene reinforced nanocomposites), buckling and vibration response are calculated.

2.2. Methodology for analytical studies

A 2D continuum orthotropic plate model is used to obtain the buckling, free and forced vibration response of the FG-graphene reinforced nanocomposites panels and the calculated forced vibration response is fed as input to Rayleigh integral to calculate the sound radiation and transmission loss characteristics. The methodology followed in the present work is presented in the form of a flowchart in Figure 2.1.

A simply supported rectangular graphene reinforced nanocomposite plate with a dimension ($a \times b \times h$) subjected to various kinds of non-uniform uniaxial edge (NUE) loads as shown in Figure 2.2 is considered, in order to investigate the effect of *GNPs* reinforcements and porosity on vibro-acoustics characteristics of a nanocomposite plate.

2.2.1. Material modelling

A detailed description about the mathematical model of the material adopted to calculate the buckling, vibration and acoustic characteristics for each type of FG-graphene reinforced composites panel is presented in this section. Three types of porosity distribution patterns, in which the porosity volume changes through the thickness of the FG-GRC plate, are considered. Plates with less porosity volume at the surface and more porosity volume at the centre is termed as VPC (increasing porosity

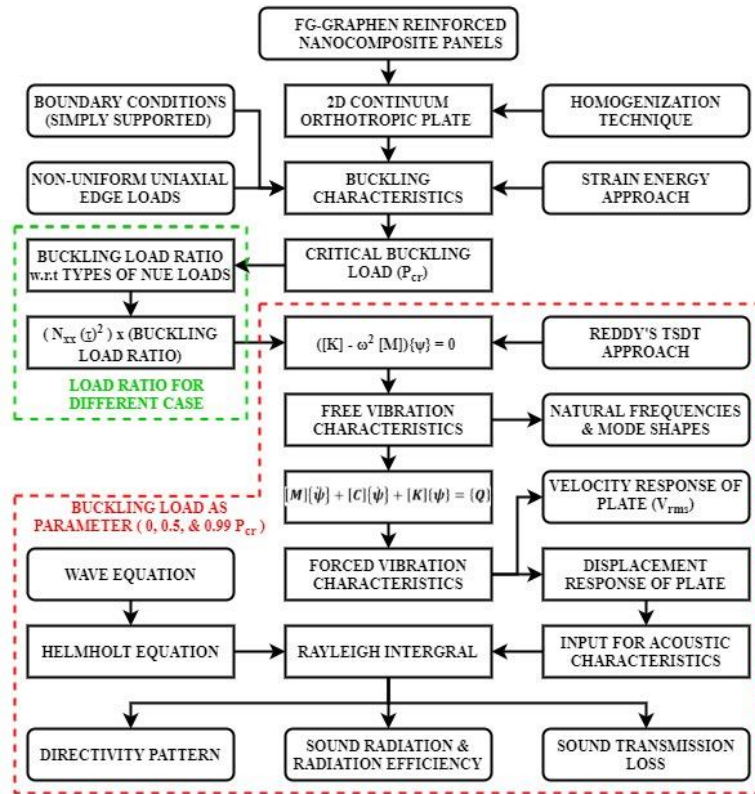
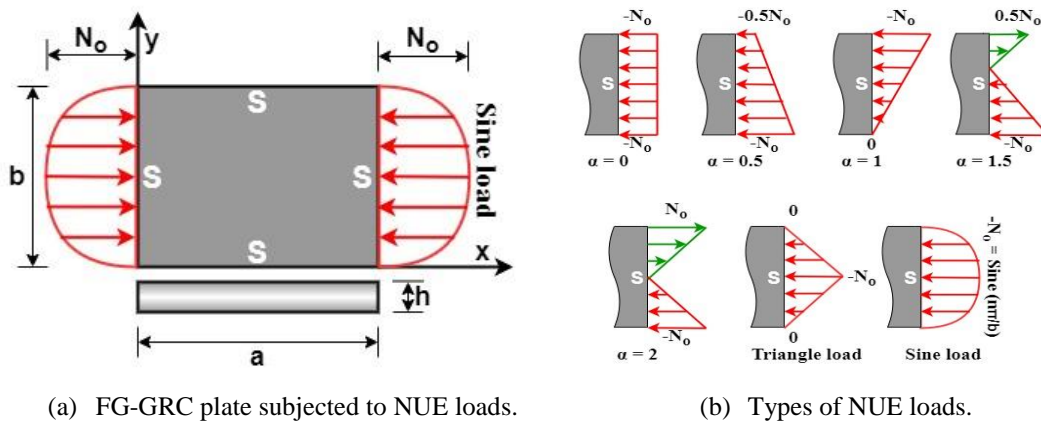


Figure 2.1: Flowchart of the detailed work process of the current thesis.



(a) FG-GRC plate subjected to NUE loads.

(b) Types of NUE loads.

Figure 2.2: Types of NUE loads used in current investigation.

towards the centre). Similarly, the plate with less porosity volume at the centre and more porosity volume at the surfaces is termed as VPS (increasing porosity towards the surface) and the plate with uniform porosity is termed as UP.

In the FG-GRC_{VPC} case, the smallest value of Young's modulus (E), shear modulus (G), and density (ρ) occurs at the middle of the plate, while in FG-GRC_{VPS} case, the smallest values of the properties occur at the top and bottom surface of the

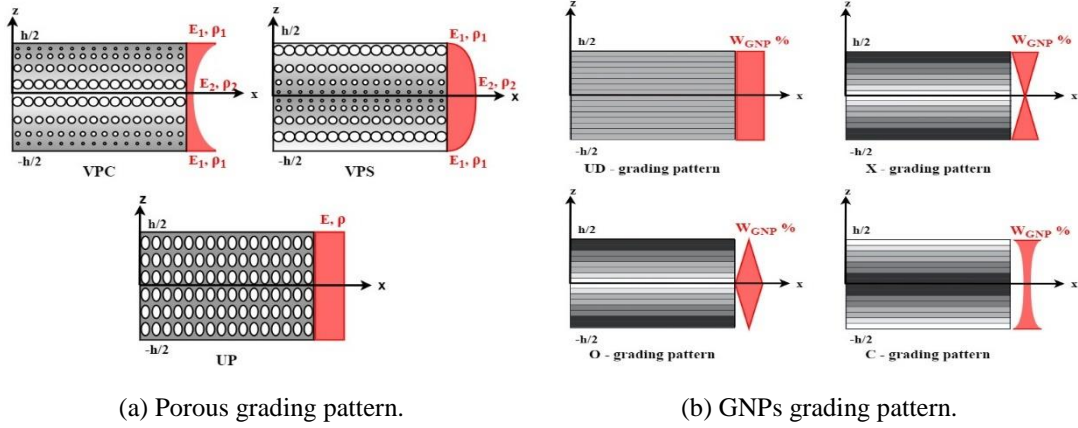


Figure 2.3: Types of porosity distribution and *GNPs* grading of FG-GRC plate used in current investigation.

plate and in FG-GRC_{UP} case, the values of the properties remain constant through the thickness. Figure 2.3 (a) shows the graphical representation of a porous distribution pattern along with the variation of material properties, which are shown in red colour. Material properties for the selected porous distribution pattern of FG-GRC plate are given in Figure 2.3 (a).

$$\text{VPC} = \begin{cases} E(z) = [1 - \eta \cos(\pi z/h)]E^*, \\ G(z) = [1 - \eta \cos(\pi z/h)]G^*, \\ \rho(z) = \left[1 - \left(\frac{1 - \sqrt{1 - \eta \cos(\pi z/h)}}{\cos(\pi z/h)}\right) \cos(\pi z/h)\right] \rho^*, \end{cases} \quad (2.1)$$

$$\text{VPS} = \begin{cases} E(z) = [1 - \eta^* (1 - \cos(\pi z/h))]E^*, \\ G(z) = [1 - \eta^* (1 - \cos(\pi z/h))]G^*, \\ \rho(z) = \left[1 - \left(\frac{1 - \sqrt{1 - \eta^* (1 - \cos(\pi z/h))}}{(1 - \cos(\pi z/h))}\right) (1 - \cos(\pi z/h))\right] \rho^*, \end{cases} \quad (2.2)$$

$$\text{UP} = \begin{cases} E(z) = \gamma E^*, \\ G(z) = \gamma G^*, \\ \rho(z) = \sqrt{\gamma} \rho^*. \end{cases} \quad (2.3)$$

By maintaining the same mass for the graphene reinforced nanocomposite plates with different porosity patterns the porosity coefficients are obtained using the following equation:

$$\int_0^{h/2} \sqrt{1 - \eta^* (1 - \cos(\pi z/h))} dz = \int_0^{h/2} \sqrt{1 - \eta (1 - \cos(\pi z/h))} dz \quad (2.4)$$

$$\int_0^{h/2} \sqrt{\gamma} dz = \int_0^{h/2} \sqrt{1 - \eta \cos(\pi z/h)} dz \quad (2.5)$$

From Eq. 2.4 and Eq. 2.5, porosity coefficients η^* and γ are obtained for the given values of η [0.2, 0.4, 0.6], and given in Table 2.1. It is observed that increase in the value of η increases the porous nature of the graphene reinforced nanocomposite plate.

The FG - Graphene reinforced nanocomposites plate is assumed to be a layered structure, in which weight fraction (W_{GNP}) of the graphene nanoplatelets ($GNPs$) continuously vary in each layer alongside the thickness direction. It is also assumed that $GNPs$ are evenly distributed in longitudinal direction, but randomly slanted towards the transverse direction of plate. Four distinctive gradings (i.e., UD, X, O, and C patterns of $GNPs$) considered for the current investigation are shown in Figure 2.3 (b) and variation of $GNPs$ weight percentage for different grading patterns through-thickness direction is highlighted in the red colour. Plate in which every layer with constant W_{GNP} is designated as FG-GRC^{UD}, while plate in which layers having least W_{GNP} at the middle and high W_{GNP} at the extreme surfaces is designated with FG-GRC^X. Similarly, a plate in which layers having high W_{GNP} at the extreme surface is designated as FG-GRC^C is similar to FG-GRC^X, instead of a linear variation of $GNPs$ grading is quadratic.

By following the rules of mixture, the volume fractions associated with UD, X, O and C grading patterns of $GNPs$ used in current investigation are given by

$$FG - GRC^{UD}: V_{GNP}^n = \left(\frac{W_{GNP}}{W_{GNP} + \left(\frac{\rho_{GNP}}{\rho_{ma}}\right)(1 - W_{GNP})} \right) \quad (2.6)$$

$$FG - GRC^X: V_{GNP}^n = 2 \left(\frac{W_{GNP}}{W_{GNP} + \left(\frac{\rho_{GNP}}{\rho_{ma}}\right)(1 - W_{GNP})} \right) \left(\frac{|2n - N_L - 1|}{N_L} \right) \quad (2.7)$$

Table 2.1: Porosity coefficients for different porous grading of porous FG-GRC plate.

	Porosity coefficients		
	VPC (η)	VPS (η^*)	UP (γ)
1	0.2	0.3442	0.8716
2	0.4	0.6708	0.7404
3	0.6	0.9612	0.6047

$$FG - GRC^O: V_{GNP}^n = 2 \left(\frac{W_{GNP}}{W_{GNP} + \left(\frac{\rho_{GNP}}{\rho_{ma}} \right) (1 - W_{GNP})} \right) \left(1 - \frac{|2n - N_L - 1|}{N_L} \right) \quad (2.8)$$

$$FG - GRC^c: V_{GNP}^n = 3 \left(\frac{W_{GNP}}{W_{GNP} + \left(\frac{\rho_{GNP}}{\rho_{ma}} \right) (1 - W_{GNP})} \right) \left(\frac{(2n - N_L - 1)^2}{N_L} \right)^2 \quad (2.9)$$

Where V_{GNP}^n is the volume fraction, N_L represents number of graphene layers and W_{GNP} denotes the overall weight percentage of *GNPs*.

Based on the analytical models proposed by Voigt Reves (Villoria and Miravete (2007)) and Halpin Tsai model (Affdl and Kardos (1976)), Young's modulus of the FG-graphene reinforced nanocomposites plate is obtained as follows

$$E = \frac{3}{8} \left[\frac{1 + \left(2 \frac{a_{GNP}}{h_{GNP}} \right) \left(\frac{\left(\frac{E_{GNP}}{E_{ma}} \right) - 1}{\left(\frac{E_{GNP}}{E_{ma}} \right) + 2 \left(\frac{a_{GNP}}{h_{ma}} \right)} \right) V_{GNP}}{1 - \left(\frac{\left(\frac{E_{GNP}}{E_{ma}} \right) - 1}{\left(\frac{E_{GNP}}{E_{ma}} \right) + 2 \left(\frac{a_{GNP}}{h_{ma}} \right)} \right) V_{GNP}} \right] E_{ma} \quad (2.10)$$

$$+ \frac{5}{8} \left[\frac{1 + \left(2 \frac{b_{GNP}}{h_{GNP}} \right) \left(\frac{\left(\frac{E_{GNP}}{E_{ma}} \right) - 1}{\left(\frac{E_{GNP}}{E_{ma}} \right) + 2 \left(\frac{b_{GNP}}{h_{GNP}} \right)} \right) V_{GNP}}{1 - \left(\frac{\left(\frac{E_{GNP}}{E_{ma}} \right) - 1}{\left(\frac{E_{GNP}}{E_{ma}} \right) + 2 \left(\frac{b_{GNP}}{h_{GNP}} \right)} \right) V_{GNP}} \right] E_{ma},$$

where E is Young's modulus, while suffix *ma* and *GNP* represents matrix and single graphene layer respectively. Using Eq. (2.10) effective Young's modulus of FG-GRC plate with a particular grading pattern can be obtained. Based on rule of mixture as given in Eq. (2.11) - Eq. (2.13), where the effective density (ρ^*), Poisson's ratio (ν^*) and shear modulus (G^*) of FG-GRC plate can be obtained.

$$\rho^* = \rho_{ma} V_{ma} + \rho_{GNP} V_{GNP} \quad (2.11)$$

$$\nu^* = \nu_{ma} V_{ma} + \nu_{GNP} V_{GNP} \quad (2.12)$$

$$G^* = \frac{E^*}{2(1 + \nu^*)} \quad (2.13)$$

The material properties of FG-graphene reinforced nanocomposites panels are given in Table 2.2.

Table 2.2: FG-graphene reinforced nanocomposites panel properties.

	Young's modulus	Poisson's ratio	Density
Copper matrix (Yang <i>et al.</i> (2018))	$E_{ma} = 130$ GPa	$\nu_{ma} = 0.34$	$\rho_{ma} = 8960$ kg/m ³
Polymer matrix (Yasmin and Daniel (2004))	$E_{ma} = 3.0$ GPa	$\nu_{ma} = 0.34$	$\rho_{ma} = 1200$ kg/m ³
Graphene nanoplates (Rafiee <i>et al.</i> (2009))	$E_{GNP} = 1.01$ TPa	$\nu_{GNP} = 0.34$	$\rho_{GNP} = 1060$ kg/m ³
Physical measurement of graphene	$a_{GNP} = 2.5$ μ m	$b_{GNP} = 1.5$ μ m	$h_{GNP} = 1.5$ μ m

Using Eq. (2.1) – (2.3) the effective material properties of different types of FG-graphene reinforced nanocomposites are calculated for the further analysis.

2.2.2. Buckling load calculation for FG-graphene reinforced nanocomposites

A detailed description about the estimation of the buckling characteristics of FG-GRC plates using 2D continuum orthotropic plate model is presented in this section. The nature of variation of the non-uniform uniaxial edge (NUE) loads is given as follows

$$N_x = N_0[1 - \alpha(y/b)] \quad (2.14)$$

α is a numerical factor. By changing α , we can obtain various particular cases. For example, by taking $\alpha = 0$ we obtain the case of uniformly distributed compressive force as shown in Figure 2.2(b). again, for $\alpha = 2$ we obtain the case of pure bending. If α is less than 2, we have a combination of bending and compression as shown in Figure 2.2(b).

By adopting the strain energy method, the buckling load of FG-GRC plate is obtained by unifying the bending strain energy ($\delta^2 U_b$) and work done by external force ($\delta^2 U_m$) as follows

$$\delta^2 \phi = \delta^2 U_b + \delta^2 U_m = 0 \quad (2.15)$$

$$\delta^2 U_b = \left(\frac{ab}{4}\right) \pi^4 \sum_{m=1}^{\infty} \sum_{n=1}^{\infty} \left[D_{11} \left(\frac{m}{a}\right)^4 + 2(D_{12} + 2D_{66}) \left(\frac{mn}{ab}\right)^2 + D_{22} \left(\frac{n}{b}\right)^4 \right] \quad (2.16)$$

$$\delta^2 U_m = \frac{1}{2} \int_0^a \int_0^b N_0 [1 - \alpha(y/b)] \delta w_{xx}^2 dx dy \quad (2.17)$$

By applying the buckling criterion, a non-trivial solution equation to calculate the value of N_o for a given NUE load case is obtained as follows

$$\frac{\partial}{\partial w_{mn}}(\delta^2 \phi) = \frac{\partial}{\partial w_{mn}}(\delta^2 U_b + \delta^2 U_m) = 0 \quad (2.18)$$

$$\begin{aligned} & \sum_{m=1}^{\infty} \sum_{n=1}^{\infty} w_{mn} \left(\frac{ab}{4}\right) \pi^4 \left[D_{11} \left(\frac{m}{a}\right)^4 + 2(D_{12} + 2D_{66}) \left(\frac{mn}{ab}\right)^2 + D_{22} \left(\frac{n}{b}\right)^4 \right] \\ & + \sum_{m=1}^{\infty} \sum_{n=1}^{\infty} w_{mn} N_o \frac{b}{2a} m^2 \pi^2 \left[\frac{\alpha}{2} - 1 \right] - \sum_{m=1}^{\infty} \sum_{n=1}^{\infty} \sum_i w_{mi} 4N_o \alpha m^2 \frac{b}{a} \left(\frac{ni}{(n^2 - i^2)^2} \right) = 0 \end{aligned} \quad (2.19)$$

where D_{11} , D_{12} , D_{66} and D_{22} are the bending stiffness components of respective FG-graphene reinforced nanocomposites panels and for i only such numbers are taken that $n \pm i$ is always odd. Load variation N_x for the *triangle* and *sine* load cases are given in Eq. (2.20) and Eq. (2.21) respectively and the corresponding equation used to obtain buckling strength of the FG-GRC plate under *triangle* and *sine* load are given in Eq. (2.22) and Eq. (2.23) respectively.

$$N_x = \begin{cases} 2N_o \frac{y}{b}, & 0 \leq y \leq \frac{b}{2} \\ -2N_o \frac{y}{b} + 2N_o, & \frac{b}{2} \leq y \leq b \end{cases} \quad (2.20)$$

$$N_x = N_o \sin \frac{\pi y}{b} \quad (2.21)$$

$$\begin{aligned} & \sum_{m=1}^{\infty} \sum_{n=1}^{\infty} w_{mn} 4N_o \left(\frac{m\pi}{a}\right)^2 \left(\frac{a}{2}\right) \left[\left(\frac{3b}{16} - \frac{b}{16} - \frac{b}{4}\right) + \left(\frac{b}{4n^2\pi^2} (\cos(n\pi - 1))\right) \right] \\ & + \sum_{m=1}^{\infty} \sum_{n=1}^{\infty} w_{mn} \left(\frac{ab}{2}\right) \pi^4 \left[D_{11} \left(\frac{m}{a}\right)^4 + 2(D_{12} + 2D_{66}) \left(\frac{mn}{ab}\right)^2 + D_{22} \left(\frac{n}{b}\right)^4 \right] \\ & + 2N_o \sum_{m=1}^{\infty} \sum_i w_{mi} \left(\frac{m\pi}{a}\right)^2 \left(\frac{a}{4}\right) \left[\frac{b}{\pi^2(n+i)^2} \left(2 \cos(n+i) \frac{\pi}{2} - \cos \pi(n+i) - 1 \right) \right] \\ & - 2N_o \sum_{m=1}^{\infty} \sum_i w_{mi} \left(\frac{m\pi}{a}\right)^2 \left(\frac{a}{4}\right) \left[\frac{b}{\pi^2(n+i)^2} \left(2 \cos(n-i) \frac{\pi}{2} - \cos \pi(n-i) - 1 \right) \right] = 0 \\ & \sum_{m=1}^{\infty} \sum_{n=1}^{\infty} w_{mn} \left[\left(\frac{ab}{2}\right) \pi^4 \left[D_{11} \left(\frac{m}{a}\right)^4 + 2(D_{12} + 2D_{66}) \left(\frac{mn}{ab}\right)^2 + D_{22} \left(\frac{n}{b}\right)^4 \right] \right] \end{aligned} \quad (2.22)$$

$$\sum_{m=1}^{\infty} \sum_{n=1}^{\infty} w_{mn} \left[\left(\frac{ab}{2}\right) \pi^4 \left[D_{11} \left(\frac{m}{a}\right)^4 + 2(D_{12} + 2D_{66}) \left(\frac{mn}{ab}\right)^2 + D_{22} \left(\frac{n}{b}\right)^4 \right] \right] \quad (2.23)$$

$$\begin{aligned}
& + \sum_{m=1}^{\infty} \sum_{n=1}^{\infty} w_{mn} \left[\frac{N_0 4 b m^2 n^2 \pi}{1 - 4 n^2} \right] \\
& + \sum_{m=1}^{\infty} \sum_i^{\infty} N_0 w_{mi} m^2 2 \pi b \left(\frac{ni}{[(n+i)^2 - 1][(n-i)^2 - 1]} \right) = 0
\end{aligned}$$

To obtain dynamic and acoustic responses of FG-graphene reinforced nanocomposites panels under different types of NUE loads, buckling load ratio (*BLR*) corresponding to a specific non-uniform edge load case is calculated by using the following equation:

$$\text{Buckling load ratio} = \frac{\text{Critical buckling load under uniform load case}}{\text{Critical buckling load under nonuniform load case}} \quad (2.24)$$

2.2.3. Buckling mode shape calculation

A double trigonometric series adopted to define the deflection of the buckled plates is given as follows

$$\delta w_{mn} = \sum_{m=1}^{\infty} \sum_{n=1}^{\infty} W_{mn} \sin\left(\frac{m\pi x}{a}\right) \sin\left(\frac{n\pi y}{b}\right) \quad (2.25)$$

By applying the third order approximation on Eq. (2.25). Obtained Eq. (2.26) – Eq. (2.28) is substitute on Eq. (2.29) to plot the buckling mode shapes of the respective plate with the dimension (*a*, *b*) under the different buckling load fraction (*P_{cr}*).

$$\begin{aligned}
\delta w_{m1} = \sum_{m=1}^3 W_{11} \sin\left(\frac{\pi x}{a}\right) \sin\left(\frac{\pi y}{b}\right) + W_{21} \sin\left(\frac{2\pi x}{a}\right) \sin\left(\frac{\pi y}{b}\right) \\
+ W_{31} \sin\left(\frac{3\pi x}{a}\right) \sin\left(\frac{\pi y}{b}\right)
\end{aligned} \quad (2.26)$$

$$\begin{aligned}
\delta w_{m2} = \sum_{m=1}^3 W_{12} \sin\left(\frac{\pi x}{a}\right) \sin\left(\frac{2\pi y}{b}\right) + W_{22} \sin\left(\frac{2\pi x}{a}\right) \sin\left(\frac{2\pi y}{b}\right) \\
+ W_{32} \sin\left(\frac{3\pi x}{a}\right) \sin\left(\frac{2\pi y}{b}\right)
\end{aligned} \quad (2.27)$$

$$\begin{aligned}
\delta w_{m3} = \sum_{m=1}^3 W_{13} \sin\left(\frac{\pi x}{a}\right) \sin\left(\frac{3\pi y}{b}\right) + W_{23} \sin\left(\frac{2\pi x}{a}\right) \sin\left(\frac{3\pi y}{b}\right) \\
+ W_{33} \sin\left(\frac{3\pi x}{a}\right) \sin\left(\frac{3\pi y}{b}\right)
\end{aligned} \quad (2.28)$$

$$\delta w_{mn} = \delta w_{m1} + \delta w_{m2} + \delta w_{m3} \quad (2.29)$$

2.2.4. Free vibration response for FG-graphene reinforced nanocomposites

Reddy's TSDT plate theory has been used to obtain the governing differential equation for the dynamic analysis. The displacement field of higher-order is defined by the following equation:

$$\begin{Bmatrix} u(x, y, z, t) \\ v(x, y, z, t) \\ w(x, y, z, t) \end{Bmatrix} = \begin{Bmatrix} u_0(x, y, t) \\ v_0(x, y, t) \\ w_0(x, y, t) \end{Bmatrix} + z \begin{Bmatrix} \phi_x(x, y, t) \\ \phi_y(x, y, t) \\ 0 \end{Bmatrix} - c_1 z^3 \begin{Bmatrix} (\phi_x + \frac{\partial w_0}{\partial x}) \\ (\phi_y + \frac{\partial w_0}{\partial x}) \\ 0 \end{Bmatrix} \quad (2.30)$$

The linear strain-displacement relation is

$$\begin{Bmatrix} \varepsilon_{xx} \\ \varepsilon_{yy} \\ \gamma_{xy} \\ \gamma_{yz} \\ \gamma_{xz} \end{Bmatrix} = \begin{Bmatrix} \frac{\partial u_0}{\partial x} \\ \frac{\partial v_0}{\partial y} \\ \frac{\partial u_0}{\partial y} + \frac{\partial v_0}{\partial x} \\ \frac{\partial w_0}{\partial y} + \phi_y \\ \frac{\partial w_0}{\partial x} + \phi_x \end{Bmatrix} + z \begin{Bmatrix} \frac{\partial \phi_x}{\partial x} \\ \frac{\partial \phi_y}{\partial y} \\ \frac{\partial \phi_x}{\partial y} + \frac{\partial \phi_y}{\partial x} \\ 0 \\ 0 \end{Bmatrix} - c_2 z^2 \begin{Bmatrix} 0 \\ 0 \\ 0 \\ \frac{\partial w_0}{\partial y} + \phi_y \\ \frac{\partial w_0}{\partial x} + \phi_x \end{Bmatrix} - c_1 z^3 \begin{Bmatrix} \frac{\partial \phi_x}{\partial x} + \frac{\partial^2 w_0}{\partial x^2} \\ \frac{\partial \phi_y}{\partial y} + \frac{\partial^2 w_0}{\partial y^2} \\ \frac{\partial \phi_x}{\partial y} + \frac{\partial \phi_y}{\partial x} + 2 \frac{\partial^2 w_0}{\partial x \partial y} \\ 0 \\ 0 \end{Bmatrix} \quad (2.31)$$

where

$$c_1 = \frac{4}{3h^2}, \quad c_2 = 3c_1 = \frac{4}{h^2} \quad (2.32)$$

The stress-strain relation for FG-graphene reinforced nanocomposites material with plane stress assumption is

$$\begin{Bmatrix} \sigma_{xx} \\ \sigma_{yy} \\ \tau_{yz} \\ \tau_{xz} \\ \tau_{xy} \end{Bmatrix} = \begin{bmatrix} Q_{11} & Q_{12} & 0 & 0 & 0 \\ Q_{21} & Q_{22} & 0 & 0 & 0 \\ 0 & 0 & Q_{44} & 0 & 0 \\ 0 & 0 & 0 & Q_{55} & 0 \\ 0 & 0 & 0 & 0 & Q_{66} \end{bmatrix} \times \begin{Bmatrix} \varepsilon_{xx} \\ \varepsilon_{yy} \\ \gamma_{yz} \\ \gamma_{xz} \\ \gamma_{xy} \end{Bmatrix} \quad (2.33)$$

where Q_{ij} denotes elastic stiffness components which can be expressed as

$$\begin{aligned}
Q_{11} = Q_{22} &= \frac{E(z)}{1 - \nu(z)^2}; \quad Q_{12} = Q_{21} = \frac{\nu(z)E(z)}{1 - \nu(z)^2}; \\
Q_{44} = Q_{55} = Q_{66} &= \frac{E(z)\nu(z)}{2(1 + \nu(z))}
\end{aligned} \tag{2.34}$$

Using Hamilton's principle, the final form of the differential equation of the FG-graphene reinforced nanocomposites panels is obtained using the following equation:

$$\int_0^l (\delta V_m + \delta V_b - \delta T) dt = 0 \tag{2.35}$$

The higher-order governing differential equations are determined by equating the coefficient of δu_o , δv_o , δw_o , $\delta \phi_x$, $\delta \phi_y$ into zero. The equilibrium equations are given by

$$\begin{aligned}
\delta u_o: \frac{\partial N_{xx}}{\partial x} + \frac{\partial N_{xy}}{\partial y} &= I_0 \ddot{u}_o + J_1 \ddot{\phi}_x - c_1 I_3 \frac{\partial \ddot{w}_o}{\partial x} \\
\delta v_o: \frac{\partial N_{yy}}{\partial y} + \frac{\partial N_{xy}}{\partial x} &= I_0 \ddot{v}_o + J_1 \ddot{\phi}_y - c_1 I_3 \frac{\partial \ddot{w}_o}{\partial y} \\
\delta w_o: \frac{\partial}{\partial x} \left(N_{xx} \frac{\partial w_o}{\partial x} + N_{xy} \frac{\partial w_o}{\partial y} \right) + \frac{\partial}{\partial y} \left(N_{xy} \frac{\partial w_o}{\partial x} + N_{yy} \frac{\partial w_o}{\partial y} \right) + \frac{\partial \bar{Q}_x}{\partial x} + \\
\frac{\partial \bar{Q}_y}{\partial y} + q + c_1 \left(\frac{\partial^2 P_{xx}}{\partial x^2} + 2 \frac{\partial^2 P_{xy}}{\partial x \partial y} + \frac{\partial^2 P_{yy}}{\partial y^2} \right) &= I_0 \ddot{w}_o - c_1^2 I_6 \left(\frac{\partial^2 \ddot{w}_o}{\partial x^2} + \frac{\partial^2 \ddot{w}_o}{\partial y^2} \right) + \\
c_1 I_3 \left(\frac{\partial^2 \ddot{u}_o}{\partial x^2} + \frac{\partial^2 \ddot{v}_o}{\partial y^2} \right) + c_1 J_4 \left(\frac{\partial^2 \ddot{\phi}_x}{\partial x^2} + \frac{\partial^2 \ddot{\phi}_y}{\partial y^2} \right) \\
\delta \phi_x: \frac{\partial \bar{M}_{xx}}{\partial x} + \frac{\partial \bar{M}_{xy}}{\partial y} - \bar{Q}_x &= J_1 \ddot{u}_o + K_2 \ddot{\phi}_x - c_1 J_4 \frac{\partial \ddot{w}_o}{\partial x} \\
\delta \phi_y: \frac{\partial \bar{M}_{yy}}{\partial y} + \frac{\partial \bar{M}_{xy}}{\partial x} - \bar{Q}_y &= J_1 \ddot{v}_o + K_2 \ddot{\phi}_y - c_1 J_4 \frac{\partial \ddot{w}_o}{\partial y}
\end{aligned} \tag{2.36}$$

It should be noted that N_o is the buckling load corresponding to the uniform uniaxial compression load case and it is varied according to the *BLR* of a particular load case to calculate the natural frequencies of the pre-stressed plate. For the simply supported boundary conditions, following Navier's solution procedure, the displacements can be expressed as follows:

$$\begin{Bmatrix} u \\ v \\ w \\ \phi_x \\ \phi_y \end{Bmatrix} = \sum_{m=1}^{\infty} \sum_{n=1}^{\infty} \begin{Bmatrix} u_{mn} \cos(\tau) \sin(\varepsilon) \\ v_{mn} \sin(\tau) \cos(\varepsilon) \\ w_{mn} \sin(\tau) \sin(\varepsilon) \\ \phi_{xmn} \cos(\tau) \sin(\varepsilon) \\ \phi_{ymn} \sin(\tau) \cos(\varepsilon) \end{Bmatrix} e^{(i\omega t)} \quad (2.37)$$

Where

$$(\tau) = \left(\frac{m\pi}{a}\right); \quad (\varepsilon) = \left(\frac{n\pi}{b}\right) \quad (2.38)$$

Grouping the terms corresponding to the unknown coefficients leads to the typical eigenvalue problem defined as follows

$$([K] - \omega^2[M])\{\psi\} = 0 \quad (2.39)$$

The reader is referred to Reddy (2006) for more details.

2.2.5. Forced vibration and sound radiation response for FG-graphene reinforced nanocomposites

Vibration response of FG-graphene reinforced nanocomposites panels under harmonic point load is given as an input value for Rayleigh integral to analyse acoustic behaviour of FG-graphene reinforced nanocomposites panels as shown in Figure 2.4. To get the forced vibration response the governing equation is given as follows:

$$[M]\{\ddot{\psi}\} + [C]\{\dot{\psi}\} + [K]\{\psi\} = \{Q\} \quad (2.40)$$

The transverse concentrated mechanical load is presumed to be a steady state harmonic load q_{mn} and expressed as Double Fourier Series as follows (Chandra *et al.* (2014)).

$$q_{mn} = \sum_{m=1}^{\infty} \sum_{n=1}^{\infty} P_{mn} \sin(\tau) \sin(\varepsilon) \quad (2.41)$$

The point load coefficient is denoted as

$$P_{mn} = \frac{4}{ab} \int_0^b \int_0^a p_0 \sin(\tau) \sin(\varepsilon) dx dy \quad (2.42)$$

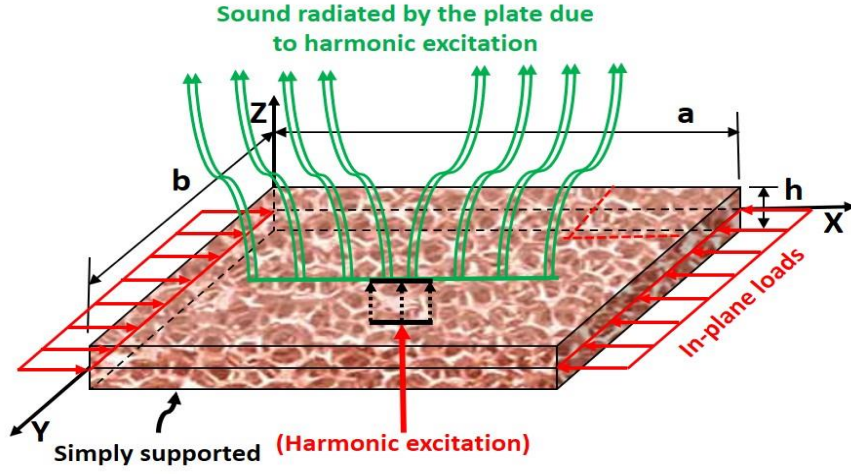


Figure 2.4: Schematics of sound radiation analysis.

The pressure load coefficient is denoted as

$$P_{mn} = 2pe \left(e^{j\omega/c_0(x \sin \theta_{inc} \cos \phi_{inc} - y \sin \theta_{inc} \sin \phi_{inc})} \right) e^{j\omega t} \quad (2.43)$$

The displacement and velocity along the normal direction are obtained by solving the governing differential Eq. (2.40) using two variable step techniques. The vibration response of the FG-graphene reinforced nanocomposites panels as function excitation frequencies is fed into Rayleigh integral to compute the acoustic radiation behaviour using the relation. For a flat FG-graphene reinforced nanocomposites plate, placed in a baffle, the Helmholtz integral equation (Chandra *et al.* (2014)) reduce to Rayleigh integral given by

$$p(r) = \frac{j\omega\rho_0}{2\pi} \int \dot{w}(r_s) \frac{e^{-jk|r-r_s|}}{|r-r_s|} ds \quad (2.44)$$

The time averaged sound intensity is given by

$$I(r) = \frac{1}{2} Re(p(r)\dot{w}^*(r_s)) \quad (2.45)$$

The sound power generated within a given volume is equal to the surface integral of the normal component of the sound intensity radiated (\bar{W}) is given by

$$\bar{W} = \oint I(r) n(r_s) ds \quad (2.46)$$

If the surface used for evaluation of this expression is chosen equal to the surface defining the vibrating body, the sound power can be written as

$$\bar{W} = \frac{1}{2} Re \left(\oint p(r) \dot{w}^*(r) ds \right) \quad (2.47)$$

Sound power level (*dB*) can be obtained using the relation

$$SWL = 10 \log \frac{\bar{W}}{W_{ref}} \quad (2.48)$$

The radiation efficiency is a measure for how well a vibrating object radiates sound. It is defined as the ratio of the sound power radiated per unit area by the object to the sound power radiated per unit area by a reference source. The reference source is a baffled piston vibrating at the same frequency with a velocity equal to the space and time-averaged squared normal velocity of the object. Sound radiation efficiency (σ) is obtained using

$$\sigma = \frac{\bar{W}}{\rho_0 c_0 S \langle \dot{w}^2 \rangle} \quad (2.49)$$

Transmission loss is the ratio of the incoming and transmitted sound powers. The sound transmission loss in decibels as shown in Figure 2.5 is obtained using

$$STL = 10 \log_{10} \left(\frac{1}{\left(\frac{\text{Transmitted power}}{\text{Incident power}} \right)} \right) \quad (2.50)$$

Transmitted sound power level is obtained by using Eq. (2.47) with pressure load (Eq. (2.43)) and incident sound power level is calculated from Eq. (2.51)

$$W_{inc} = \frac{p_{inc}^2 \cos\theta ab}{2\rho c} \quad (2.51)$$

2.2.6. Buckling load calculation for isotropic plate

To study the influence of non-uniform uniaxial edge loads on buckling characteristics of isotropic panels, where D_{11} , D_{12} , D_{66} and D_{22} are the bending stiffness components of Eq. (2.19), Eq. (2.22) & Eq. (2.23) are substituted by $D = Eh^3/12(1 - \nu^2)$. Then the non-trivial solution equation to calculate the value of N_o for a given NUE load case for isotropic plate is obtained as follows

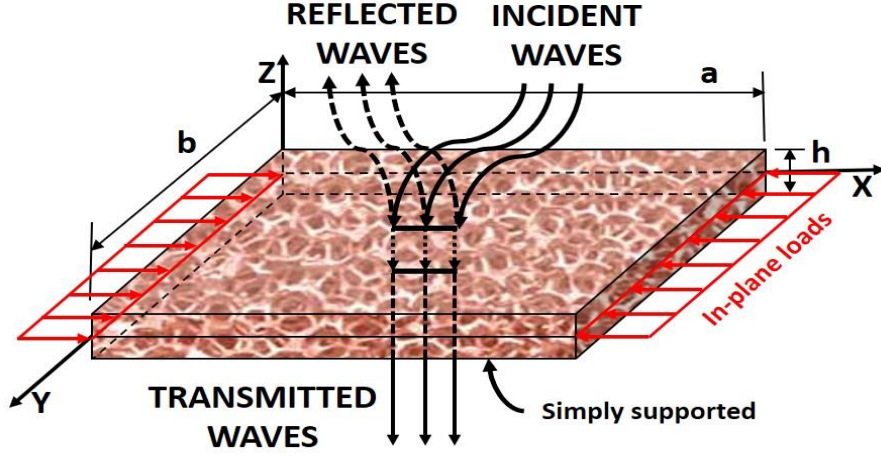


Figure 2.5: Schematics of sound transmission loss analysis.

$$\sum_{m=1}^{\infty} \sum_{n=1}^{\infty} w_{mn} \left[\left(D\pi^4 \left(\frac{m^2}{a^2} + \frac{n^2}{b^2} \right)^2 \right) - \left(N_o \frac{m^2 \pi^2}{a^2} \left(1 - \frac{\alpha}{2} \right) \right) \right] - 8\alpha \sum_{m=1}^{\infty} \sum_{n=1}^{\infty} \sum_{i=1}^{\infty} \frac{m^2}{a^2} w_{mi} \left(\frac{ni}{(n^2 - i^2)^2} \right) = 0 \quad (2.52)$$

$$\sum_{m=1}^{\infty} \sum_{n=1}^{\infty} w_{mn} \left[N_o \left(\frac{m\pi}{a} \right)^2 \left(\frac{4n^2}{\pi(1 - 4n^2)} \right) + \frac{D\pi^4}{2} \left[\left(\frac{m}{a} \right)^2 + \left(\frac{n}{b} \right)^2 \right]^2 \right] + \sum_{m=1}^{\infty} \sum_{n=1}^{\infty} \sum_{i=1}^{\infty} N_o \left(\frac{m\pi}{a} \right)^2 \left(\frac{2}{\pi} \right) \frac{w_{mi} ni}{[(n+i)^2 - 1][(n-i)^2 - 1]} \quad (2.53)$$

$$\sum_{m=1}^{\infty} \sum_{n=1}^{\infty} w_{mn} \left[N_o \left(\frac{m\pi}{a} \right)^2 \left(-\frac{1}{2} + \frac{1}{n^2 \pi^2} (\cos n\pi - 1) \right) + D\pi^4 \left[\left(\frac{m}{a} \right)^2 + \left(\frac{n}{b} \right)^2 \right]^2 \right] + \sum_{m=1}^{\infty} \sum_{n=1}^{\infty} \sum_{i=1}^{\infty} N_o \left(\frac{m\pi}{a} \right)^2 \left[\frac{(2 \cos(n+i) \frac{\pi}{2} - \cos(n+i) \pi - 1)}{\pi^2 (n+i)^2} - \frac{(2 \cos(n-i) \frac{\pi}{2} - \cos(n-i) \pi - 1)}{\pi^2 (n-i)^2} \right] \quad (2.54)$$

Where Eq. (2.52) is for different load factor (α) of NUE loads cases, Eq. (2.53) & Eq. (2.54) is for *sine* and *triangle* load case respectively.

2.3. Validation for analytical studies

2.3.1. Buckling load validation

A square non-porous simply supported FG-GRC plate ($0.45 \times 0.45 \times 0.045$ m, $W_{GNP} = 1\%$) with different graphene platelets distribution patterns investigated by Thai *et al.* (2019) using the NURBS formulation is considered for the validation of buckling load calculation. The material properties of a graphene/epoxy nanocomposite plate are mentioned in Table 2.2. Critical buckling change (%) calculated using Eq. (2.55) for non-porous FG-GRC plate subjected to uniform uniaxial in-plane compressive loads are set side by side comparison with the results reported by Thai *et al.* (2019) as shown in Table 2.3. The critical buckling change (%) predicted with respect to an overall number of graphene layers of the FG-GRC plate from the present approach using strain energy method is compared with Thai *et al.* (2019) shows good agreement.

$$\text{Critical buckling change (\%)} = \frac{\text{Critical buckling load with GNPs}}{\text{Critical buckling load without GNPs}} \quad (2.55)$$

In order to validate buckling load calculation procedure, a simply supported square porous FG-GRC plate with the different porosity patterns and $W_{GNP} = 1\%$ analysed by the Yang *et al.* (2018) based on Chebyshev-Ritz method is considered. The material properties used by Yang *et al.* (2018) are given in Table 2.4. Dimensionless buckling load (Eq. 2.56) of porous FG-GRC plate with various porosity distributions under uniform in-plane load (i.e., using strain energy method) matches very closely with the results reported by Yang *et al.* (2018) as seen in Table 2.4. The difference in results is due to the difference in the method followed to obtain the buckling load.

$$\bar{N} = N_x \frac{(1 - \nu_{ma}^2)}{E_{ma}h} \quad (2.56)$$

Table 2.3: Comparison of critical buckling change (%) result with Thai *et al.* (2019).

Number of graphene layers	FG-GRC ^{UD}			FG-GRC ^X			FG-GRC ^O		
	Thai <i>et al.</i> (2019)	Present	Absolute % error	Thai <i>et al.</i> (2019)	Present	Absolute % error	Thai <i>et al.</i> (2019)	Present	Absolute % error
25	433	432.4	0.13	562	567.4	0.96	287	284.2	0.97
30	433	432.4	0.13	563	567.7	0.83	285	283.8	0.42
35	433	432.4	0.13	566	568.9	0.51	284	281.8	0.77
40	433	432.4	0.13	567	568	0.17	282	281.2	0.28

Table 2.4: Validation of dimensionless buckling load results with Yang *et al.* (2018).

Thickness ratio (b/h)	VPC distribution ($\eta = 0.5$)			VPS distribution ($\eta^* = 0.8231$)			UP distribution ($\gamma = 0.6733$)		
	Yang <i>et al.</i> (2018)	Present	Absolute % error	Yang <i>et al.</i> (2018)	Present	Absolute % error	Yang <i>et al.</i> (2018)	Present	Absolute % error
20	0.00992	0.00964	2.8	0.00590	0.00575	2.5	0.00822	0.00821	0.1
30	0.00445	0.00439	1.3	0.00264	0.00259	1.8	0.00368	0.00366	0.5
40	0.00251	0.00248	1.1	0.00149	0.00147	1.3	0.00208	0.00207	0.4
50	0.00161	0.00160	0.6	0.00095	0.00094	1.1	0.00133	0.00133	0

2.3.2. Vibration frequencies validation

To validate calculation of free vibration frequencies of FG-GRC plate with different graded distribution patterns of *GNPs* and porosity the FG-GRC plates under simply supported condition studied by Xu *et al.* (2019) and Yang *et al.* (2018) are considered. The dimensionless natural frequencies predicted using Eq. (2.57) are compared with the results of Xu *et al.* (2019) for the validation of the frequencies of the plate with different *GNPs* grading pattern in Table 2.5. There is an exact matching of the results due to the same theory (i.e., TSDT method) and methodology used in the present work and Xu *et al.* (2019) study.

$$\bar{\omega} = \omega \left(\frac{a^2}{h} \right) \sqrt{\frac{\rho_{ma}(1 - \nu_{ma}^2)}{E_{ma}}} \quad (2.57)$$

$$\bar{\omega} = \omega a \sqrt{\frac{\rho_{ma}(1 - \nu_{ma}^2)}{E_{ma}}} \quad (2.58)$$

The dimensionless natural frequencies predicted using Eq. (2.58) are compared with the results of Yang *et al.* (2018) for the validation of the frequencies of the plate with different graded pattern of porosity in Table 2.6. There is a good agreement between the results with a minor error percentage, due to differences in the

Table 2.5: Validation of dimensionless natural frequencies (Eq. (2.57)) results with Xu *et al.* (2019).

W_{GNP}	Dispersion pattern	Xu <i>et al.</i> (2019)	Current study	Xu <i>et al.</i> (2019)	Current study	Xu <i>et al.</i> (2019)	Current study
0%	Matrix	5.6 ^(1,1)	5.6 ^(1,1)	13.8 ^(2,1)	13.8 ^(2,1)	21.1 ^(2,2)	21.1 ^(2,2)
	UD	9.1 ^(1,1)	9.1 ^(1,1)	22.6 ^(2,1)	22.6 ^(2,1)	35.7 ^(2,2)	35.7 ^(2,2)
0.5%	X	10.4 ^(1,1)	10.4 ^(1,1)	25.7 ^(2,1)	25.7 ^(2,1)	40.4 ^(2,2)	40.4 ^(2,2)
	O	7.6 ^(1,1)	7.6 ^(1,1)	18.9 ^(2,1)	18.9 ^(2,1)	30.0 ^(2,2)	30.0 ^(2,2)
	C	11.1 ^(1,1)	11.1 ^(1,1)	27.6 ^(2,1)	27.6 ^(2,1)	42.9 ^(2,2)	42.9 ^(2,2)

Note: The modal indices of the respective natural frequencies are denoted by the superscript number.

Table 2.6: Validation of dimensionless natural frequencies (Eq. (2.58)) results with Yang *et al.* (2018).

Thickness ratio (b/h)	VPC distribution ($\eta = 0.5$)			VPS distribution ($\eta^* = 0.8231$)			UP distribution ($\gamma = 0.6733$)		
	Yang <i>et al.</i> (2018)	Present	Absolute % error	Yang <i>et al.</i> (2018)	Present	Absolute % error	Yang <i>et al.</i> (2018)	Present	Absolute % error
20	0.357	0.354	0.8	0.275	0.272	1.1	0.325	0.322	0.9
30	0.239	0.238	0.4	0.184	0.183	0.5	0.217	0.215	0.9
40	0.180	0.180	0	0.138	0.138	0	0.163	0.163	0
50	0.144	0.144	0	0.110	0.110	0	0.131	0.131	0

theory used in present (i.e., TSDT method) and Yang *et al.* (2018) study (i.e., Chebyshev-Ritz method).

2.3.3. Validation of acoustic response

A metallic plate with dimension of $0.5 \times 0.4 \times 0.003 \text{ m}^3$ under simply supported condition inspected by Chandra *et al.* (2014) is examined for the validation of sound radiation and sound transmission loss response. The structure is supposed to be vibrating in air ($\rho_0 = 1.21 \text{ kg/m}^3$, $c_o = 343 \text{ ms}^{-1}$) due to the harmonic excitation and consequent acoustic response is analysed in terms of sound power level (SWL). A concentrated force with a magnitude of 1 N is applied at the centre of the plate over the frequency range of 0-500 Hz. A constant loss factor of 0.01 is considered for the response studies. Sound power level response result predicted from present TSDT approach compared with the response reported by Chandra *et al.* (2014) using FSDT method in Figure 2.6 (a). Similarly, the sound transmission loss response results of the plate due to the normal incidence of 1 N/m^2 pressure wave also compared in Figure 2.6 (b). Both the sound power level and sound transmission loss responses obtained using the present approach matches well with the responses reported by Chandra *et al.* (2014).

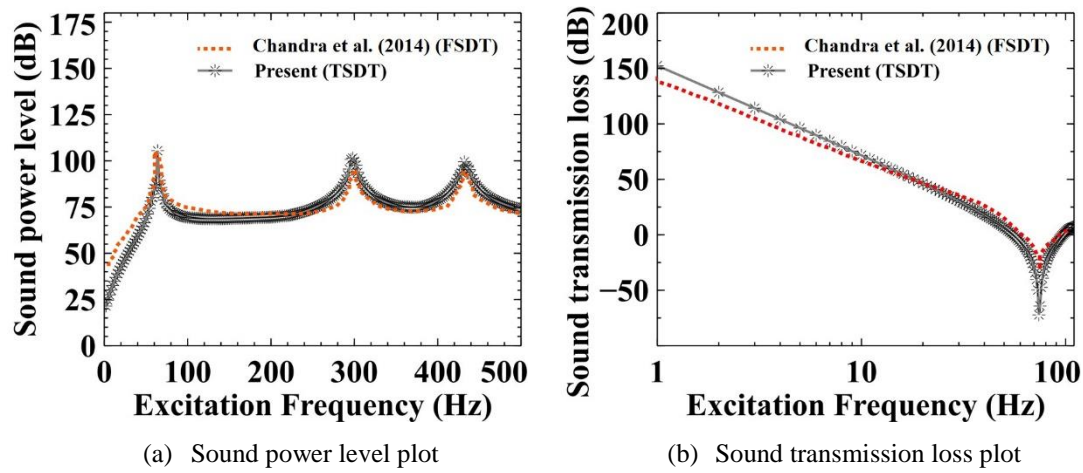


Figure 2.6: Comparison of sound power level (dB) and sound transmission loss with Chandra *et al.* (2014).

2.4. Closure

In this chapter, the methodology adopted to predict buckling, vibration and acoustic characteristics is presented. This is followed by validation studies carried out to ensure the accuracy of results based on 2D continuum orthotropic plate model. The predicted buckling, vibration and acoustic characteristic results of FG-graphene reinforced nanocomposites plates by using the 2D continuum orthotropic plate model is compared with the published results and shows the good agreement with the present approach.

CHAPTER 3

3. VIBRO-ACOUSTIC STUDIES OF ISOTROPIC PANEL UNDER NON-UNIFORM UNIAXIAL EDGE LOADS

3.1. Introduction


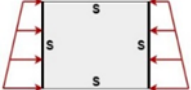





A detailed literature survey places of interest that vibration and airborne noise on human comfort and health on pilots/passengers is noteworthy. Henceforth, it is necessary to design the aerospace structures which take care of the acoustic comfort. However, a design which involves the acoustic comfort is always done without considering the pre-stress effect caused by the edge loads. This drawback can be overcome by exploring the influence of in-plane stresses on vibration and acoustic response of the engineering structure. In this aspect, the present chapter focuses on the study of influence of non-uniform uniaxial edge loads on vibration and acoustic response characteristics of isotropic panels. A rectangular isotropic plate (all edges are simply supported) with dimensions $0.5 \times 0.4 \times 0.01$ m³ is considered for the contemporary investigation. An aluminium plate with Young's modulus 70 GPa, Poisson's ratio 0.3 and density 2700 kg/m³ is considered. Following Eq. (3.1) is used to obtain the buckling coefficient (k)

$$k = \frac{N_o b^2}{\pi^2 D} \quad (3.1)$$

3.2. Buckling characteristics of isotropic plate

The buckling coefficient and buckling load ratio of the metal plate subjected to different types of axial compressive loading cases are given in Table 3.1. From Table 3.1, it is noted that the nature of edge loading has a remarkable effect on the buckling coefficient (k). The buckling coefficient values are obtained by using a second approximation to the respective characteristic equation except for the load factor $\alpha = 2$ in which the third approximation is used. It is noted that the buckling coefficient values increases with load factor (α). The load factor case $\alpha = 2$ yields maximum critical buckling load compared to the other cases as part of the plate is under the tensile force which enhances

Table 3.1: Buckling coefficient and buckling load ratio for different types of loading for isotropic plate.

Types of loading	Loading factor (α)	Buckling coefficient (k)	Buckling load ratio
	0	10.50 ¹	1 ¹
	0.5	13.97 ¹	0.7515 ¹
	1	20.63 ¹	0.5090 ¹
	1.5	36.74 ¹	0.2858 ¹
	2	60.00 ²	0.2062 ²
	Triangle	21.00 ¹	0.5001 ¹
	Sine	12.37 ¹	0.8479 ¹

The superscript number indicates the modal indices of buckling mode.

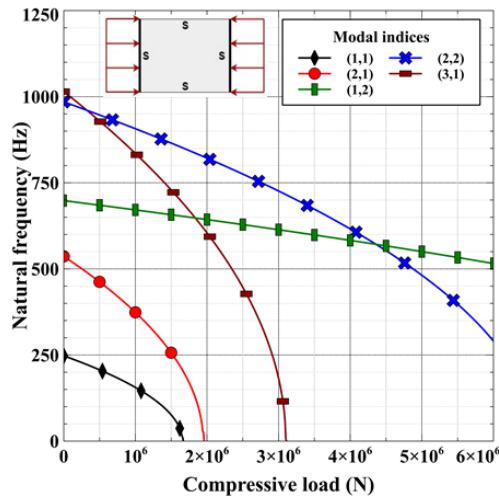
the stability of the isotropic plate. It should be noted that the buckling load ratio reported in Table 3.1 is used to obtain the free and forced vibration responses based on HSDT as described earlier.

3.3. Vibration response of the isotropic plate

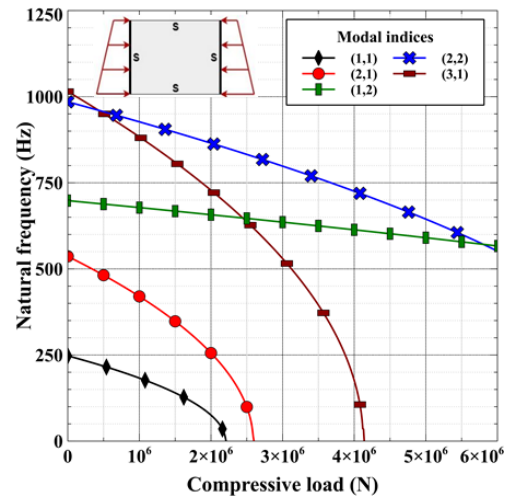
3.3.1. Free vibration characteristics of the isotropic plate

Variations of natural frequencies of the first five modes with an increase in axial compressive load for different load cases are given in Figure 3.1. The natural frequency reduces due to the increase in axial compressive load for all the loading cases as reported by several researchers. The natural frequency of a mode approach zero when the metal plate is subjected to corresponding buckling load as seen in Figure 3.1. The plate buckles with (1,1) mode for all the loading cases except for $\alpha = 2$ loading case under which the plate buckles with (2,1) mode. It should be noted that the mode for which the natural frequency approaches zero frequency for the lowest uniaxial compressive load is called buckling mode.

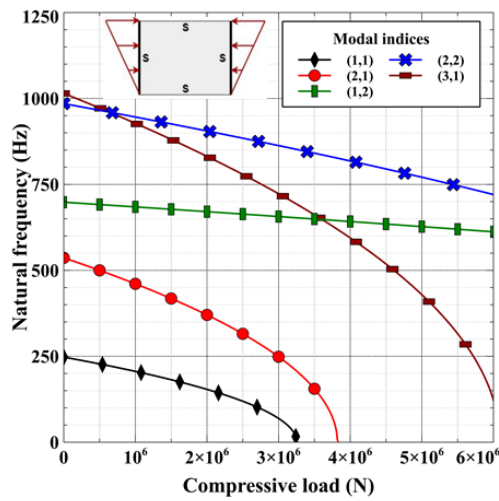
For $\alpha = 2$ loading case, the buckling mode is (2,1) because tensile force along half of the edge stabilizes the plate while compressive force along the remaining half of the edge destabilizes it. Changes in free vibration mode shapes (1,1) and (2,1) with increase in axial-load for $\alpha = 2$ is shown in Figure 3.2. Symmetry of the modes about the horizontal axis vanishes with increase in axial-load and the maximum amplitude position also shifting downwards. This is attributed to the load configuration in which the combined effect of compressive and tensile forces is pushing the maximum amplitude position downwards. Furthermore, for the better understandings the natural frequency reduction for the first three fundamental modes under different non-uniform edge loads are given in Table 3.2.



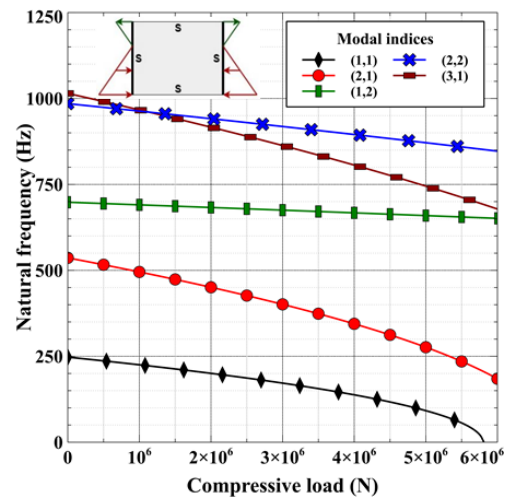
(a) Loading factor $\alpha = 0$



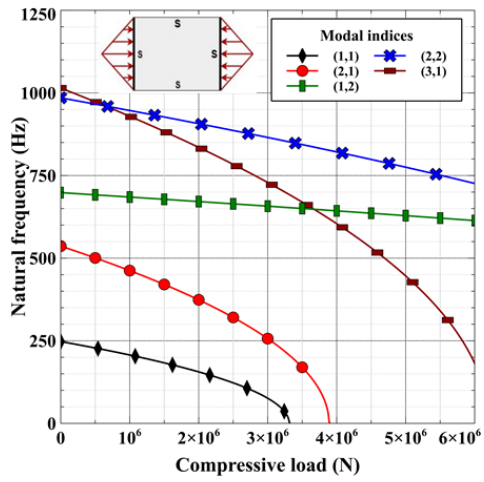
(b) Loading factor $\alpha = 0.5$



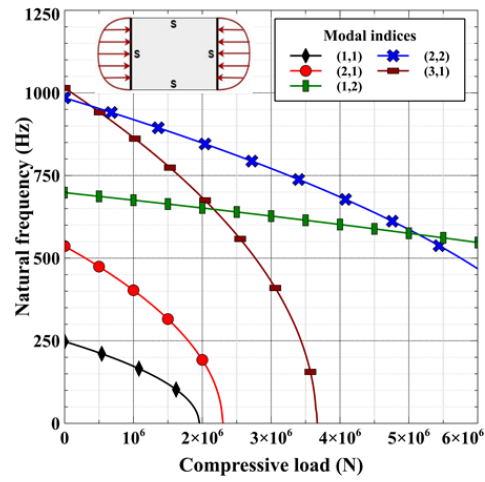
(c) Loading factor $\alpha = 1$



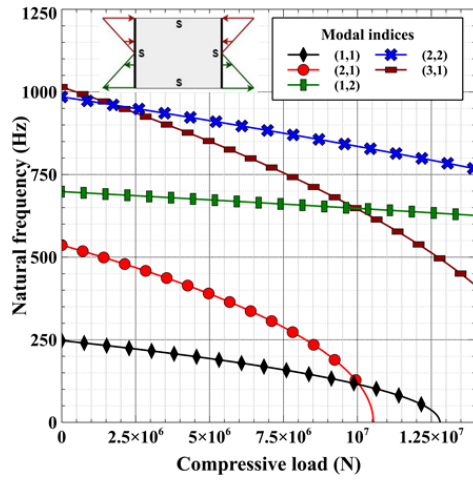
(d) Loading factor $\alpha = 1.5$



(e) Triangle load

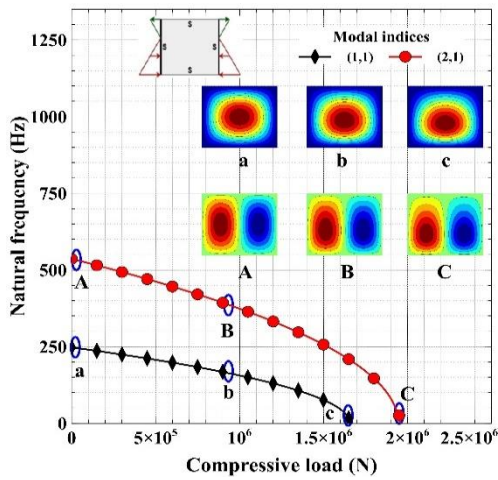


(f) Sine load

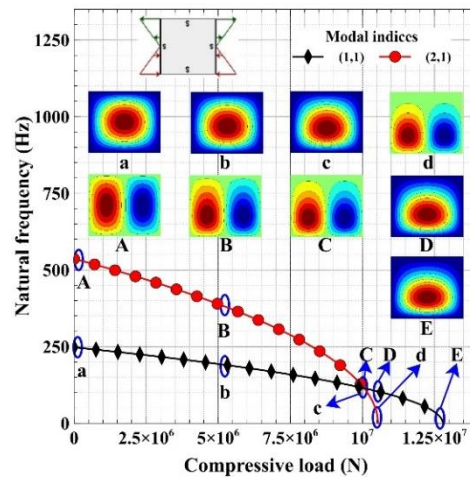


(e) Loading factor $\alpha = 2$

Figure 3.1: Variation of natural frequencies with NUE loads for various edge loading cases.



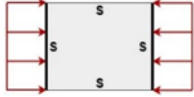


(a) $\alpha = 1.5$ load case



(b) $\alpha = 2$ load case

Figure 3.2: Variation on the natural frequencies and associated mode shapes of the isotropic plate with increase in axial load intensity under $\alpha = 2$ case.

Table 3.2: Variations on the natural frequencies of the isotropic plate with increase in non-uniform load intensity.

Types of loads	Load fractions	Mode numbers		
		(1,1)	(2,1)	(1,2)
No load	$0 P_{cr}$	247.72	536.57	698.50
	$0.5 P_{cr}$	175.18(29.28)*	406.59(24.22)	676.22(3.19)
	$0.97 P_{cr}$	43.13(82.59)	223.87(58.28)	654.59(6.29)
	$0.5 P_{cr}$	175.16(29.29)	406.56(24.23)	676.21(3.19)
	$0.97 P_{cr}$	42.94(82.67)	223.72(58.31)	654.58(6.29)
	$0.5 P_{cr}$	196.93(20.50)	379.45(29.28)	682.17(2.34)
	$0.97 P_{cr}$	132.46(46.53)	93.03(82.66)	666.44(4.59)

The superscript * indicates the difference in % with references to the present solution.



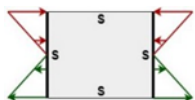
3.3.2. Forced vibration characteristics

In this section, the forced vibration response of the plate under the non-uniform mechanical loading cases is investigated. The plate is excited with a time-varying harmonic force of 1 N in 0 to 1500 Hz frequency range (with 0.5 Hz resolution) at (0.125, 0.1) with the respective x and y-axis from the origin. The upper limit of excitation frequency is chosen as 1500 Hz as the coincidence frequency of the plate analysed is around 1200 Hz. The first ten modes have been considered for the forced vibration characteristics to investigate the influence of mode shifting behaviour and intensity of non-uniform edge load on the dynamic response.

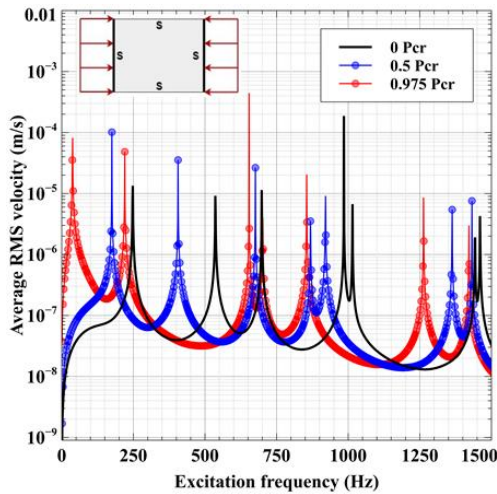
In order to understand the effect of NUE loads on vibration response of the plate, two separate load fraction cases have been considered. In *Case 1* the response is analysed by keeping P_{cr} of the respective loading cases in fraction ($0 P_{cr}$, $0.5 P_{cr}$ and $0.975 P_{cr}$). However, in *Case 2*, P_{cr} of the uniform load (for which the P_{cr} is lowest) case is kept as the load fraction for all the loading types ($0 P_{cr}^{uni}$, $0.5 P_{cr}^{uni}$ and $0.975 P_{cr}^{uni}$). Variation of average RMS velocity with respect to excitation frequency is considered to analyse the influence of nature of variation of edge load on the forced vibration response. Forced vibration responses for selected edge loading under *Case 1* and *Case 2* are given in Figure 3.3. These NUE loads cause a reduction in structural stiffness and it is anticipated that resonant amplitude should increase with a rise in applied edge load magnitude. For the better understandings the forced vibration

response peak amplitude reduction for the first three fundamental modes under different non-uniform edge loads are given in Table 3.3.

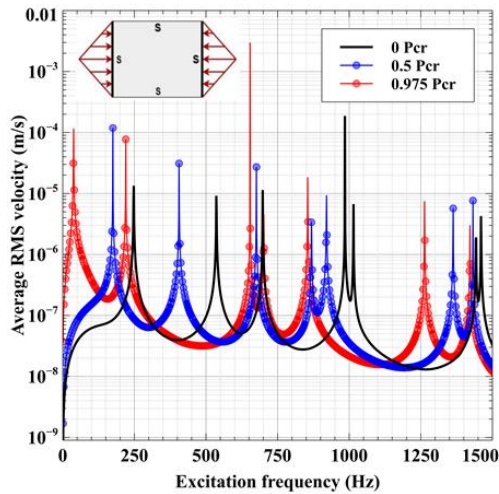
Table 3.3: Variations on the forced vibration response peaks of the isotropic plate with increase in non-uniform load intensity.

Types of loads	Load fractions	Mode numbers		
		(1,1)	(2,1)	(1,2)
No load	$0 P_{cr}$	1.34×10^{-5}	9.18×10^{-6}	1.14×10^{-5}
	$0.5 P_{cr}$	1.01×10^{-4} (0.1326)*	3.54×10^{-5} (0.2593)	2.66×10^{-6} (0.0428)
	$0.97 P_{cr}$	8.17×10^{-5} (0.1640)	4.83×10^{-5} (0.1900)	4.42×10^{-4} (0.0257)
	$0.5 P_{cr}$	2.45×10^{-5} (0.5469)	1.51×10^{-5} (0.6079)	6.71×10^{-6} (1.6989)
	$0.97 P_{cr}$	8.11×10^{-5} (0.1652)	4.59×10^{-5} (0.2000)	8.21×10^{-6} (1.3885)
	$0.5 P_{cr}$	1.85×10^{-5} (0.7243)	1.42×10^{-5} (0.6464)	1.86×10^{-5} (0.6129)
	$0.97 P_{cr}$	1.17×10^{-3} (0.0114)	1.21×10^{-4} (0.0758)	1.12×10^{-5} (1.0178)

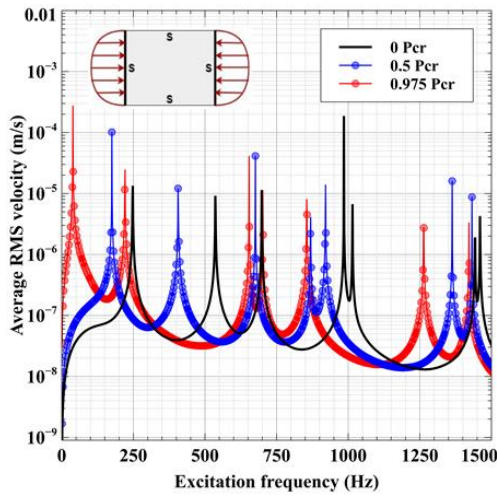
The superscript * indicates the increment in multiples with references to the present solution.



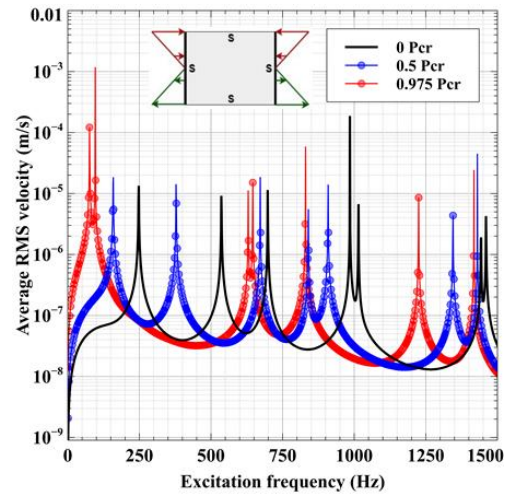
(a) $\alpha = 0$ (uniform), case 1 & case 2



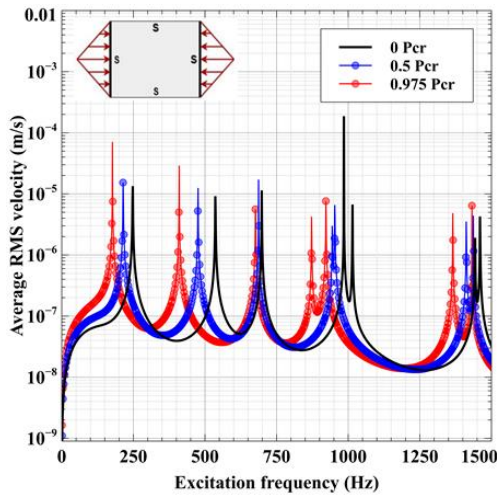
(b) Triangle load, case 1



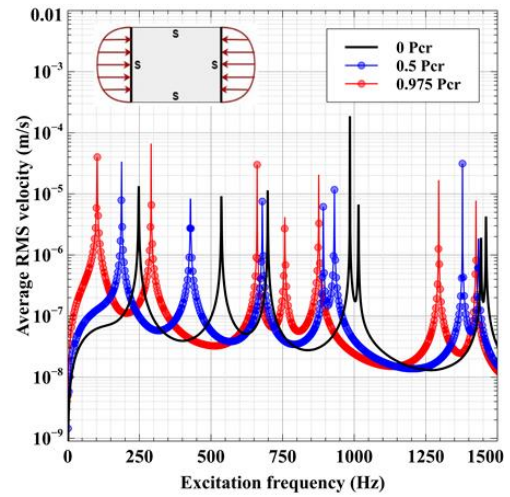
(c) Sine load, case 1



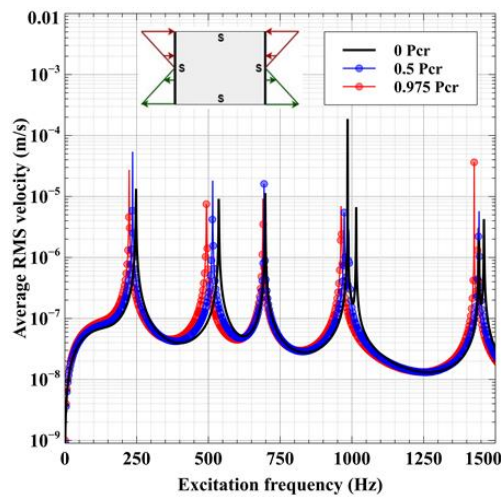
(d) $\alpha = 2$, case 1



(e) Triangle load, case 2



(f) Sine load, case 2



(g) $\alpha = 2$, case 2

Figure 3.3: Effect of NUE loads on forced vibration response.

From Figure 3.3, it is observed that an increase in the amplitude of the fundamental resonant peak with a rise in the edge load magnitude, in most of the cases. However, similar variation is not observed in the resonant amplitudes of the higher modes. Shifting of the natural frequencies towards the lower frequency, with increase in the axial load magnitude affects the resonant amplitude variation. Except for *sine* and $\alpha = 2$ loading cases, the same kind of variation in vibration response is observed as the resonant amplitude of the third mode is highest than the first two modes.

In $\alpha = 2$ case, one can witness the shifting of first (1,1) and second (2,1) modes with increase in the magnitude of the edge load. It is clearly noted that mode shifting and amplitude of the respective modes are judged very poorly in *Case 2* when compared to the *Case 1*. In *Case 1* the load fraction value is set to its respective load configuration such that the mode shifting of the respective load is observed clearly. However, in *Case 2* the load fraction to the different NUE load types will be corresponding to the $\alpha = 0$ (uniform) loading case. For *Case 2* loading, the load intensity is very low hence the shifting of modes is not clearly observed, as the mode shifting phenomenon occurs when the magnitude of the edge load is around the critical buckling load. The 3D representation of the effects of NUE load $\alpha = 2$, *Case 1* on forced vibrational response is shown in Figure 3.4. for the better understanding of mode shifting phenomenon.

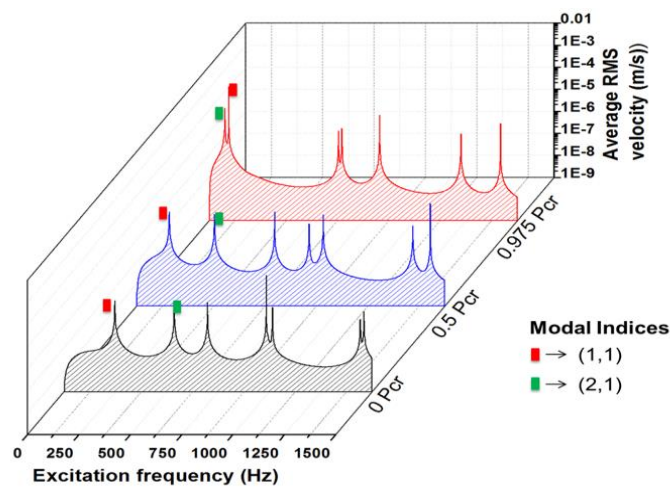


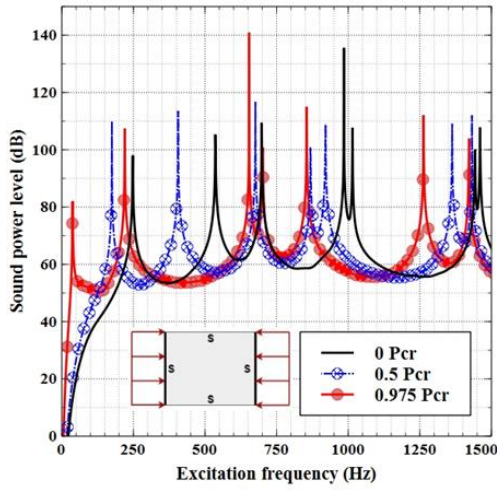
Figure 3.4: 3D representation of effect of increase in axial load magnitude on the forced vibration response for $\alpha = 2$, *Case 1* loading.

3.4. Sound radiation characteristics

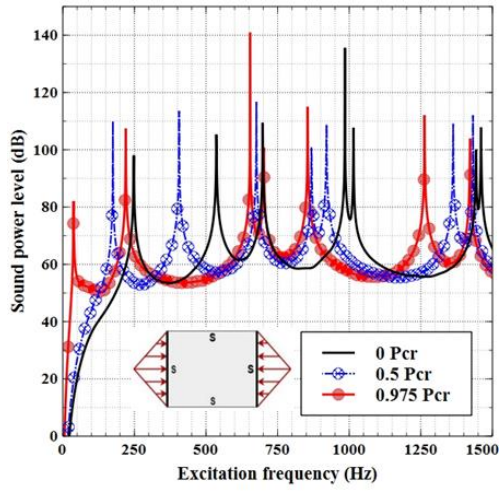
In this section, acoustic response characteristics such as sound power level, sound radiation efficiency and spatial sound pressure variation of the isotropic plate are investigated. Acoustic response analysis is performed for the same excitation conditions which are considered for the forced vibration response analysis. The vibration response predicted in Section 3.3.2. is fed as an input value to the Rayleigh integral to predict the acoustic radiation behaviour. The load fraction in *Case 1* (i.e., by keeping P_{cr} of the respective loading cases in fraction like $0 P_{cr}$, $0.5 P_{cr}$ and $0.975 P_{cr}$) is considered for the better analysis of the acoustic characteristics as mentioned in Section 3.3.2.

Sound power level radiated by the isotropic plate as a function of excitation frequency for $\alpha = 0$ (uniform), *triangle*, *sine* and $\alpha = 2$ loading cases are shown in Figure 3.5 with the excitation ranging from 0 to 1500 Hz. It has been shown that the NUE load has a significant influence on sound radiation of the metal plate. It is witnessed that the peak of the response floats towards the low frequency with the increase in the buckling load fraction. When compared to the forced vibration response plot, the acoustic power level plot has a different trend and noted that amplitude of the fundamental peak has been drastically reduced when compared to the second and third mode peaks. The reduction in structural stiffness is significant when the magnitude of the applied NUE load is around the buckling load.

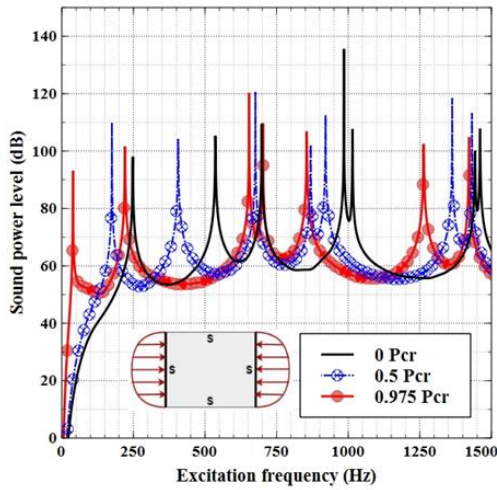
Similarly, the sound power radiated is function of excitation frequency and normal velocity of the plate. Due to these reasons, reduction in natural frequency and resonant amplitude of fundamental mode is significant compared to the other modes. So, instead of an increase in peak value (as seen in forced vibration response), the peak value of the fundamental mode reduces for $0.975 P_{cr}$ case. For the better understandings the sound power level peak amplitude reduction for the first three fundamental modes under different non-uniform edge loads are given in Table 3.4.



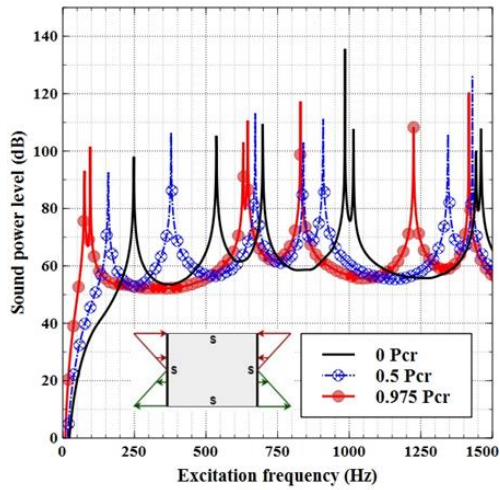
(a) $\alpha = 0$ (uniform), case 1



(b) Triangle load, case 1



(c) Sine load, case 1



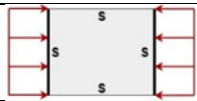

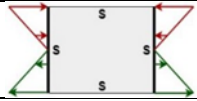
(d) $\alpha = 2$, case 1

Figure 3.5: Effect of NUE load on sound power level (dB).

It is found that, except for $\alpha = 2$ and *sine* load cases, the variation of resonant amplitude of the fundamental mode with increase in the compressive load is same for the other cases. However, for $\alpha = 2$ case, increase in fundamental peak is observed for $0.5 P_{cr}$ load and significant reduction in the peak is observed for $0.975 P_{cr}$ load. For $\alpha = 2$ case, it is also noted that fundamental SWL peak shifts from mode (1,1) to the mode (1,2) and second mode dominates over the fundamental mode near the buckling load. Effect of increase in magnitude of the NUE load and shifting of mode on SWL of the plate under $\alpha = 2$ loading case is shown in a 3D plot as seen in Figure 3.6 for the better understanding.

Figure 3.7 shows the sound pressure level variation of the plate with and without axial edge loads. In order to understand the SPL distribution pattern, the plate is excited at the fundamental frequency. It is observed that for all the load cases the SPL distribution is symmetrical (i.e., fundamental mode is (1,1)) and centre align, except for $\alpha = 2$ load case it is unsymmetrical (i.e., partially shifted towards left side) due to that the plate fundamental mode is (2,1).

Table 3.4: Variations on the sound power level peaks of the isotropic plate with increase in non-uniform load intensity.

Types of loads	Load fractions	Mode numbers		
		(1,1)	(2,1)	(1,2)
No load	$0 P_{cr}$	97.99	105.29	109.45
	$0.5 P_{cr}$	109.95 (11.96)	113.53 (8.24)	116.70 (7.25)
	$0.97 P_{cr}$	82.03 (15.96)	107.35 (2.06)	140.90 (31.45)
	$0.5 P_{cr}$	110.01 (12.02)	113.47 (8.18)	116.71 (7.26)
	$0.97 P_{cr}$	82.15 (15.84)	107.51 (2.22)	141.26 (31.81)
	$0.5 P_{cr}$	91.32 (6.67)	106.43 (1.14)	113.12 (3.67)
	$0.97 P_{cr}$	101.46 (3.47)	93.07 (12.22)	103.00 (6.45)

The superscript * indicates the difference in dB level with references to the present solution.

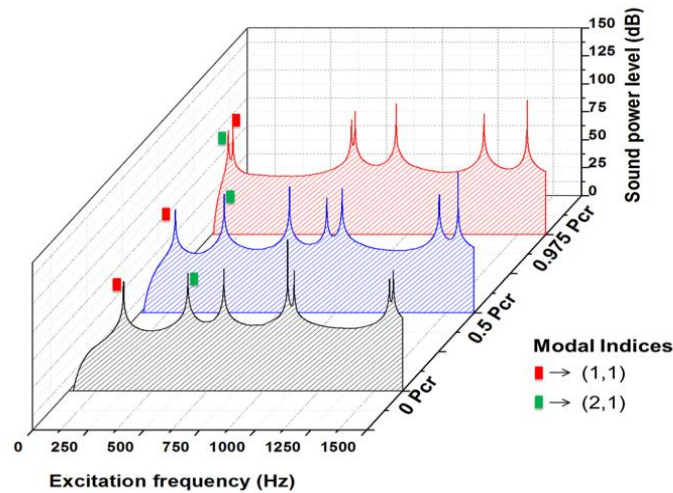


Figure 3.6: 3D representation of effect of increase in axial load magnitude on the sound power level response for $\alpha = 2$, Case 1 loading.

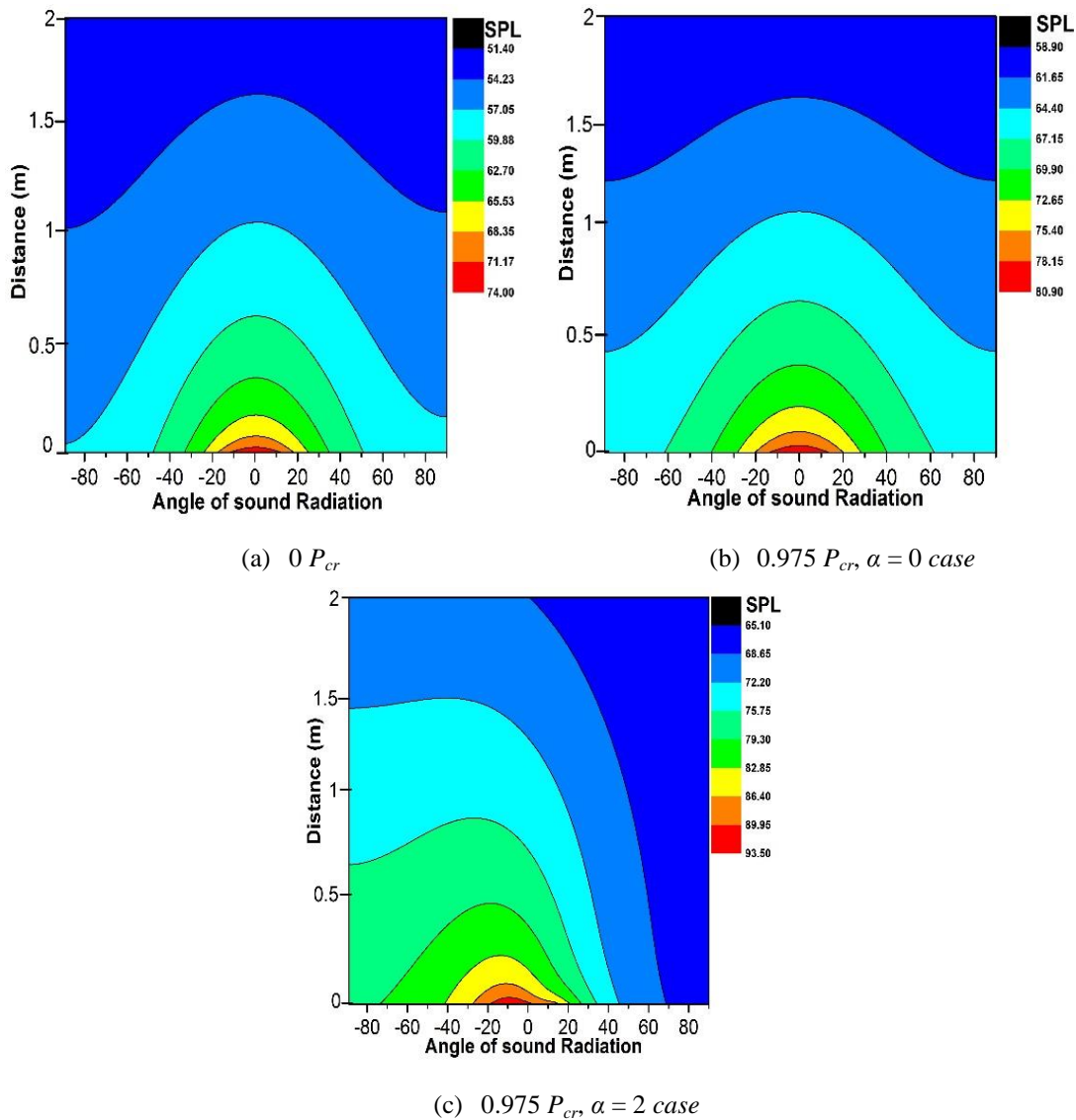
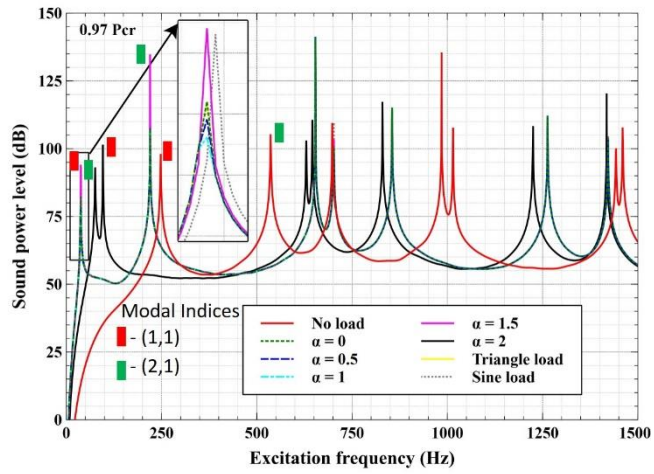
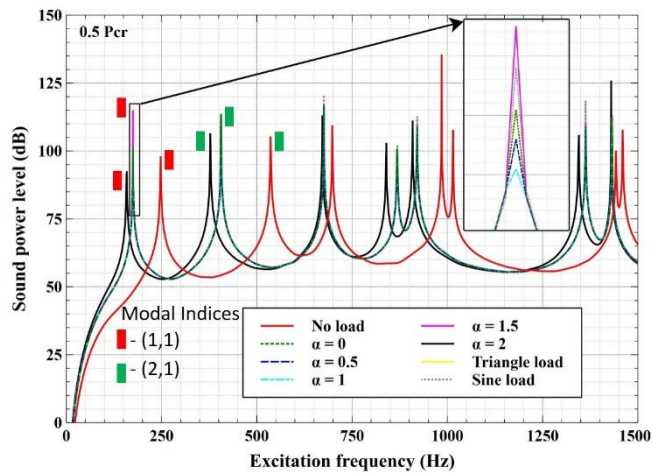


Figure 3.7: Contour representational effect of NUE load on sound pressure level radiated.

Figure 3.8, shows the comparison study of sound radiation characteristics of the isotropic plate under different NUE loads. It is observed that there is a significant influence on the change of resonate frequency peaks, due to the increase in magnitude of the applied load, when compared to the no load condition. However, $\alpha = 2$ case has distinctive pattern of sound power level and change resonance peak when compared to the other load cases. Whereas for the other load cases (i.e., excluding $\alpha = 2$ case) same kind of change in resonance peaks, varying in the range of 5-15 dB level is observed. Increase in magnitude of the axial load and nature of variation of the axial load does not have any significant effect on the sound radiation efficiency as observed in Figure 3.9.

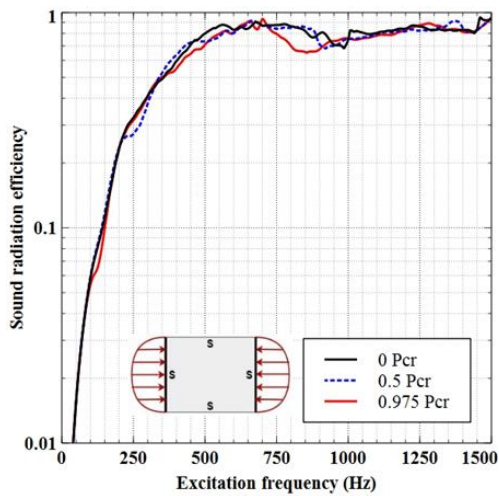


(a) $0.975 P_{cr}$, Case 1

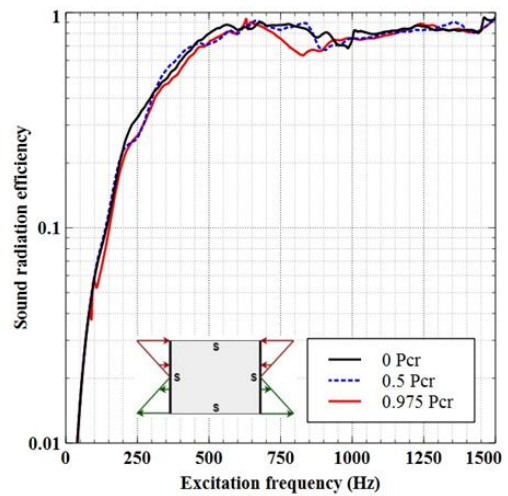


(b) $0.5 P_{cr}$, Case 1

Figure 3.8: Effect of different NUE load on sound power level (dB).



(a) Sine load, Case 1



(b) $\alpha = 2$, Case 1

Figure 3.9: Effect of non-uniform loads on sound radiation efficiency.

Figure 3.10, represents the change of sound power level in constant octave bands. Figure 3.10, clearly shows that SWL increase with an increase in compressive load in the lower frequency bands. This can be attributed to the significant reduction in the fundamental frequency with increase in applied axial load magnitude. However, there is no specific trend in SWL that corresponds to mid and higher frequency bands. Figure 3.11, shows the overall sound power level corresponding load fraction $0P_{cr}$, $0.5P_{cr}$ & $0.975P_{cr}$ for the different edge loading cases analysed. Variation in overall SWL with an increase in compressive load is significant and also profound to the load configuration. From Figure 3.11, it is also observed that the SWL at a particular load

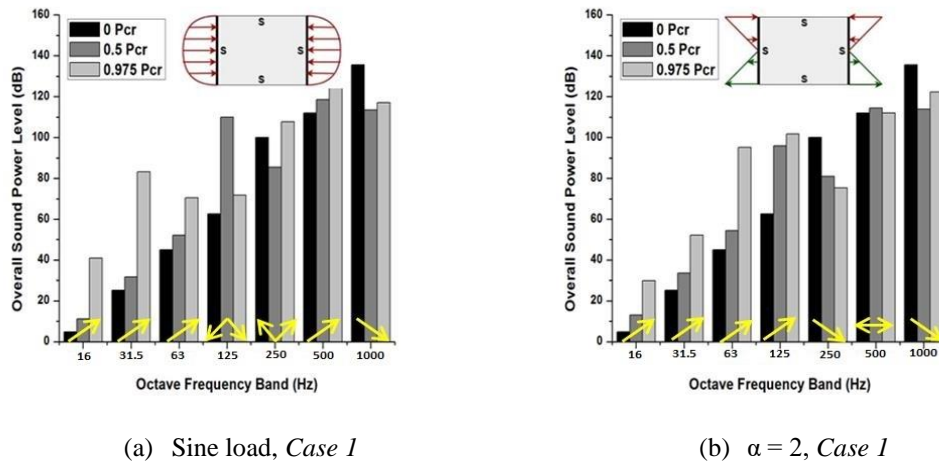


Figure 3.10: Effect of non-uniform load on sound power level (dB) vs octave frequency band.

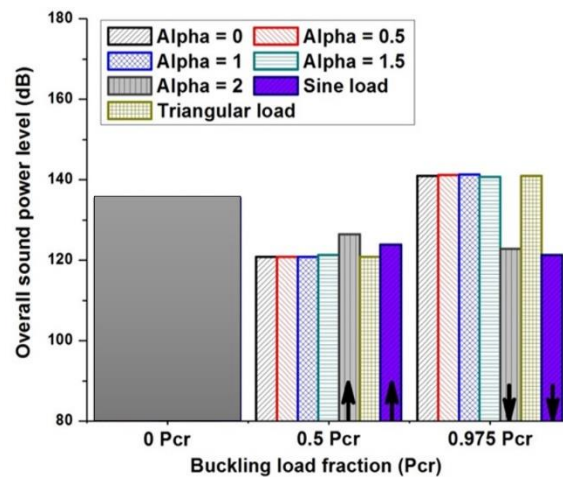


Figure 3.11: Effect of NUE load on the overall sound power level (dB).

fraction is more or less same for the different load cases except for $\alpha = 2$ and *sine* load cases. The directivity pattern of the plate is obtained at a one-meter radius above the centre of the plate for 240 Hz and 1440 Hz excitation frequencies and shown in Figure 3.12. for $\alpha = 0$ and $\alpha = 2$, loading cases respectively. It is seen from Figure 3.12 that the directivity pattern is symmetry for all the loading cases for 240 Hz excitation as the excitation frequency is around the fundamental mode frequency of the plate. However, a non-symmetrical directivity pattern is observed for 1440 Hz excitation due to the involvement of higher modes. It is also observed that an increase in the load fraction reduces the SPL distribution level for all the cases. This can be attributed to the non-uniformity of NUE load interference in the stiffness of the plate.

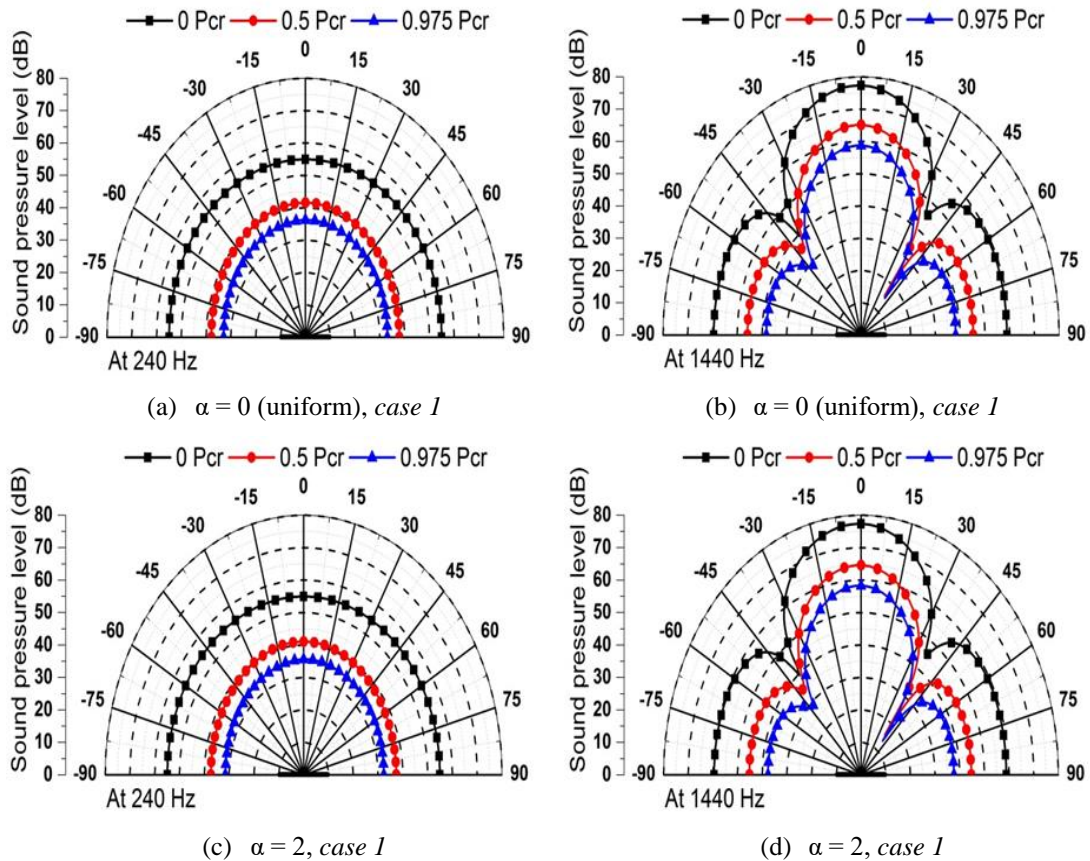
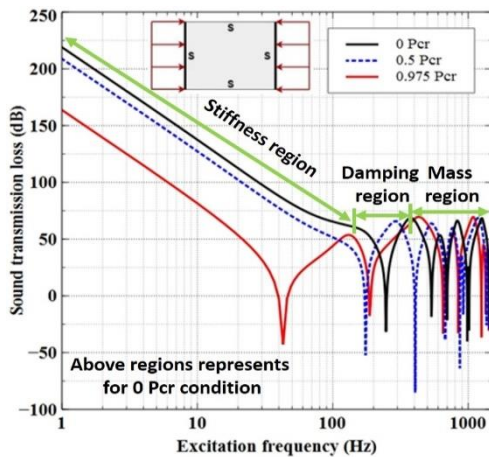


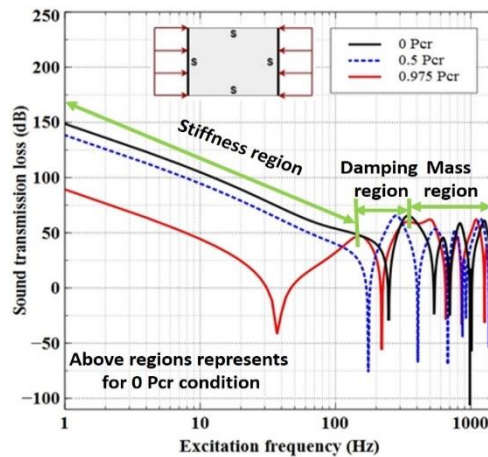
Figure 3.12: Effect of NUE load on the sound directivity pattern is obtained at a one-meter radius above the centre of the plate (z-axis).

3.5. Sound transmission loss characteristics

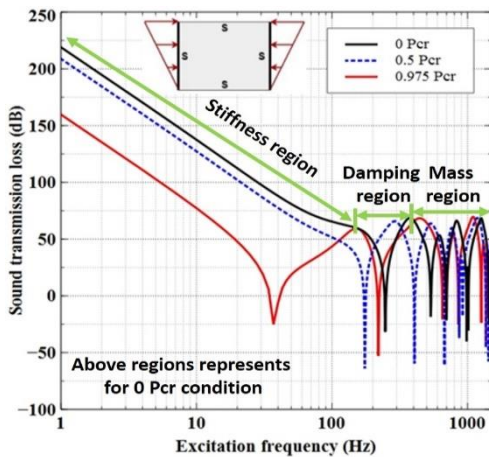
For the sound transmission loss analysis of the isotropic plate under NUE loading conditions, a sound pressure wave with the intensity of 1 N/m^2 is considered. The effect of various load fractions on sound transmission loss for normal incidence and angle incidence of the sound waves, i.e., θ is 0° and 45° are presented in Figure 3.13. The transmission loss curve is divided into three distinctive zones which are sensitive concerning the stiffness, mass, and damping of the structure. The region of the STL curve corresponds to zero to fundamental frequency is known as stiffness section. It is noted that the increase in buckling load fraction on the plate reduces the stiffness by the occurrence of buckling criterion which caused the reduction of dB level with respective exciting frequencies. Significant amount of reduction in STL is observed with increase in the axial load magnitude. Reduction of 11 dB level in $0.5P_{cr}$



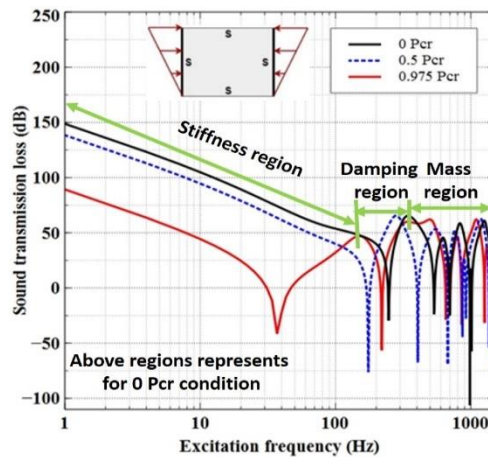
(a) Normal incidence, $\alpha = 0$



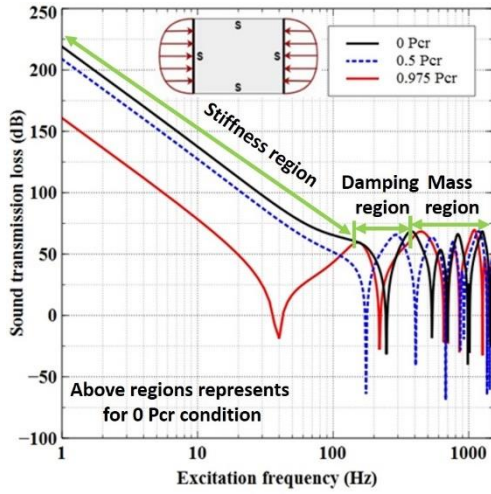
(b) Angle incidence, $\alpha = 0$



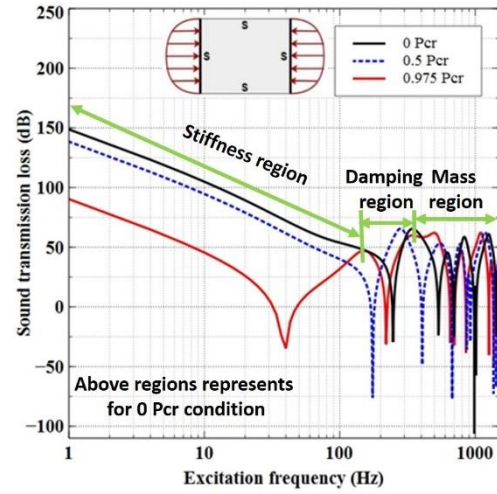
(c) Normal incidence, $\alpha = 1$



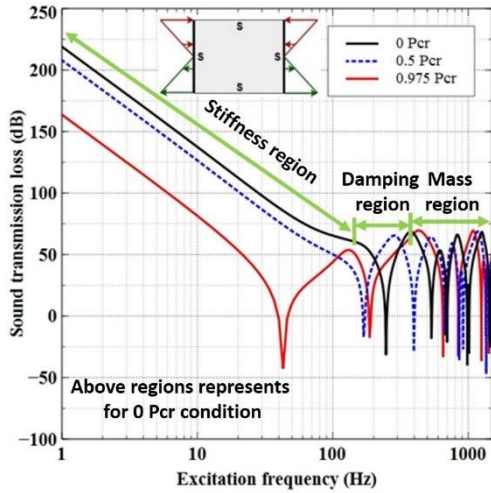
(d) Angle incidence, $\alpha = 1$



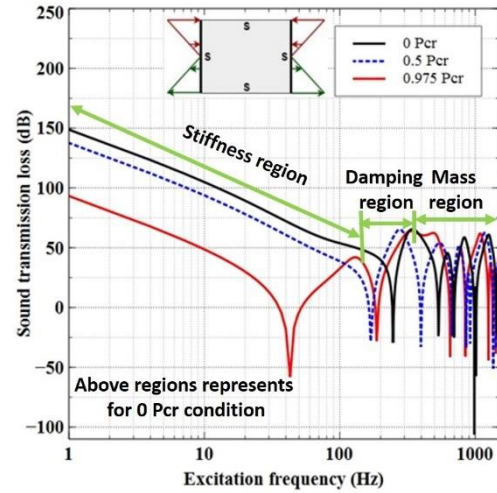
(e) Normal incidence, *Sine load*



(f) Angle incidence, *Sine load*



(g) Normal incidence, $\alpha = 2$



(h) Angle incidence, $\alpha = 2$

Figure 3.13: Effect of NUE load on sound transmission loss for normal and angle incidence.

and 56 dB level in $0.975P_{cr}$ occurred when compared to the zero in-plane load condition is noted.

The reason is that the NUE load softens the stiffness of structure due to the formation of in-plane stress. Increase in magnitude of applied non-uniform edge load reduces the peak value of the fundamental mode. Due to this STL of the plate decreases with increase in the buckling load fraction value. Then the damping region represents the narrow bandwidth of the resonance peak, this part of the curve signifies the amount of damping which causes the negative region of STL. However, it is noted that sound transmission loss value ends up in negative value due to the various characteristic reasons for the isotropic plate. Furthermore, it has been noticed that the

damping influence of fundamental mode is dominating than the higher modes for $\alpha = 2$, but the rest of the cases the behaviour is noticed in reverse vice versa trend.

It is observed that the transmission loss is negative at the resonance frequency and happens due to several reasons for finite plates. The vibration response of a finite plate can be theoretically infinite at the resonance for an undamped case and is mainly controlled by the damping of the material and structure. A small damping value may result in sharp dips in the STL curve as reported by Assaf *et al.* (2008) and Fuller (1990). Also, based on the findings of Thompson *et al.* (2009), STL value greater than unity (or negative), should not necessarily be viewed as error in the calculation and the statement is supplemented by the present results. The part of the curve after the fundamental frequency peak represents the mass sensitive region. Since there no significant change in mass of the plate for all the loading conditions so an only a small amount of change in dB level is noted. Figure 3.14., shows the comparison study of sound transmission loss of the isotropic plate under different non-uniform compression loads.

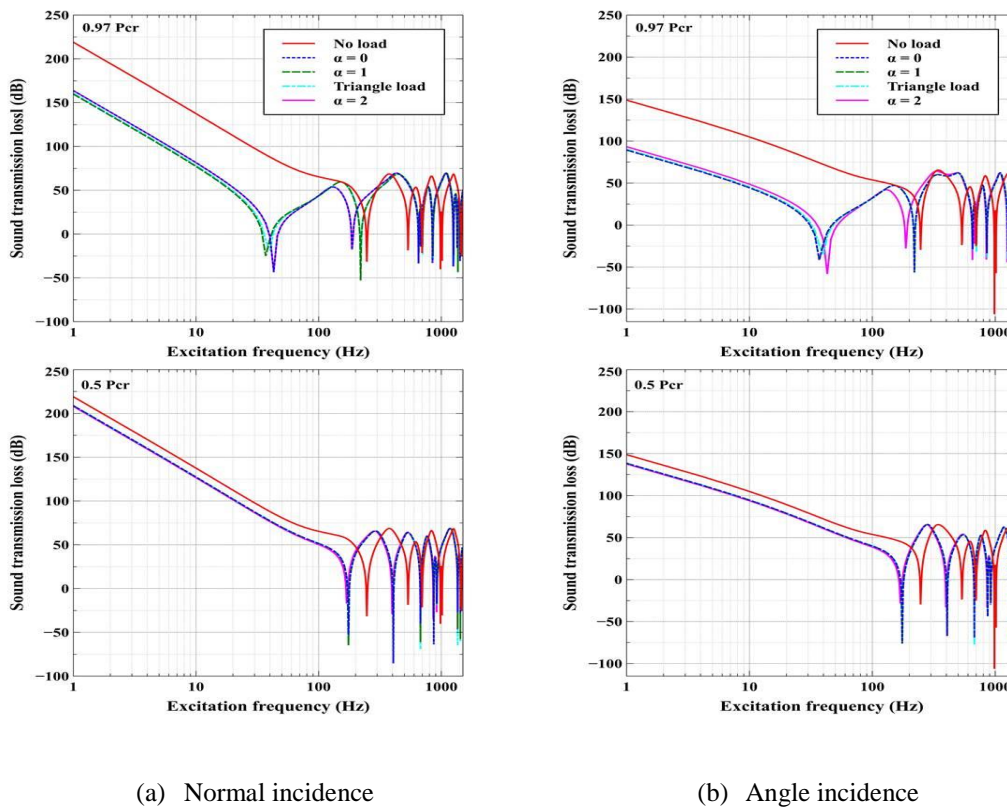


Figure 3.14: Effect of different NUE loads on sound transmission loss.

3.6. Closure

The buckling and vibroacoustic responses of an isotropic plate with simply supported boundary conditions under non-uniform edge loading are studied based on the analytical method. The strain energy approach is adopted to estimate the buckling load (P_{cr}). Free and forced vibration response of the plate is obtained using an analytical method based on Reddy's TSDT while sound radiation behaviour is analysed using Rayleigh Integral. It is found that the buckling load parameter is significantly influenced by the nature of NUE load variation. The fundamental buckling mode for $\alpha = 2$ is (2,1) while for the remaining cases it is (1,1). Due to the structural stability obtained by the combined effect of tensile and compressive forces $\alpha = 2$ case has a higher buckling load. Better variation in average RMS velocity with increase in edge load is observed when the plate is analysed by varying P_{cr} of the respective edge load case. In acoustical radiation characteristics, the effect of NUE load has a major role which signifies the 17 dB level of SWL level reduces at $0.975P_{cr}$ of fundamental frequency peak when compared to the no-load condition, and slight increase in amplitude of fundamental frequency peak for the $0.5P_{cr}$ due to the stiffness interference of the structure. In sound radiation efficiency, no significant variation has been observed concerning the magnitude of the axial load applied and type of the NUE load. However, overall sound power level plot indicates when load fraction increases the overall SWL also increased in lower frequencies, but diminished for the higher frequencies. The effect of applied NUE load is significant only in the stiffness region hence remarkable change in STL is observed only in the stiffness region compared to the damping and mass regions.

CHAPTER 4

4. BUCKLING AND FREE VIBRATION STUDIES OF FG-GRC PANEL UNDER NON-UNIFORM UNIAXIAL EDGE LOADS

4.1. Introduction

Form the above in-depth literature study, it is found that no analyses have been performed to study the effect of NUE loading on free vibration characteristics of FG-GRC structures. The non-uniform compressive load develops the mechanical pre-stress, as a result, it alters the stiffness and dynamic behaviour of the structure. Hence, it is necessary to examine the dynamic performance of the FG-GRC structure under NUE loads for design enhancement. In this present study, an analytical approach based on the strain energy method and Reddy's TDST approach has been carried out to investigate the free vibration behaviour of a rectangular FG-GRC plate subjected to the different edgewise compressive load.

A rectangular FG-GRC flat plate where all edges under a simply supported condition with dimension $0.5 \times 0.4 \times 0.01 \text{ m}^3$ is considered for the current investigation. Considering the real-time manufacturing and precision of the results *12 layers* of *GNPs* are considered in this study. The plate is considered to be a functionally graded graphene-reinforced nanocomposite whose material properties are shown in Table 2.2. The effect of *GNPs* grading arrangement, the weight fraction of the graphene platelets and geometric parameters of the FG-GRC plate on buckling strength and free vibration characteristics of rectangular FG-GRC plates are examined in this section. Values of buckling load ratio used to analyse free vibration characteristics of a plate under different NUE load cases are shown in Table 4.1. The dimensionless buckling load and natural frequency are defined as

$$\bar{P}_{cr} = P_{cr}^x \frac{b^2}{E_{ma} h^3} \quad (4.1)$$

$$\bar{\omega} = \omega \sqrt{\frac{\rho_{ma}}{E_{ma}}} \left(\frac{b^2}{h} \right) \quad (4.2)$$

Table 4.1: Buckling load ratio of FG-GRC plate under NUE loads.

Loading factor (α)	0	0.5	1	1.5	2	Triangle	Sine
Buckling load ratio	1 ¹	0.7515 ¹	0.5090 ¹	0.2857 ¹	0.2058 ²	0.5001 ¹	0.8484 ¹

The superscript number indicates the modal indices of buckling mode.

4.2. Investigation on buckling characteristics of the FG-GRC plate

4.2.1. Effect of *GNPs* pattern and weight fraction on FG-GRC plate under NUE load

Dimensionless buckling load values of rectangular FG-GRC plate under different types NUE loadings with different *GNPs* distribution patterns are given in Table 4.2 and graphical illustration of the same is shown in Figure 4.1. As of the data shown in Table 4.2 and Figure 4.1 it can be noticed that the load factor (α) of compressive loading has notable impact on buckling load of rectangular FG-GRC plate. By using a second-order approximation to the corresponding characteristic equation of the strain energy method the buckling load is obtained except for the load factor $\alpha = 2$, for which third-order approximation is used. It is evident that the rise of load factor α , increases the buckling strength of the FG-GRC plate subjected to the NUE load. This is due to an increase of tensile force intensity of load as the α increases on the FG-GRC plate, ultimately area subjected to tensile force enhances the structural stiffness of the plate. Due to this reason, the FG-GRC plate under $\alpha = 2$ load case obtains better stability and withstand higher buckling load when compared to uniform compressive load because of addition stiffness gained by the tensile force. Compared to the rest of the cases $\alpha = 2$ yields maximum buckling load due to the one-half part of the plate is under the tensile force which enhances the stability of rectangular FG-GRC plate. It should be noted that the buckling load ratio reported in Table 4.1 is used to obtain the free vibration frequencies based on TSDT as described earlier.

Table 4.2: Dimensionless buckling load of FG-GRC plate under NUE load.

W_{GNP}	Grading pattern	Alpha (α)					Triangle	Sine
		0	0.5	1	1.5	2		
0	Matrix	3.91 ¹	5.20 ¹	7.68 ¹	13.68 ¹	22.38 ²	7.82 ¹	4.60 ¹
0.3%	UD	7.81 ¹	10.39 ¹	15.34 ¹	27.34 ¹	44.71 ²	15.62 ¹	9.20 ¹
	X	9.71 ¹	12.92 ¹	19.07 ¹	33.98 ¹	55.56 ²	19.41 ¹	11.44 ¹
	O	5.91 ¹	7.87 ¹	11.62 ¹	20.70 ¹	33.85 ²	11.83 ¹	6.97 ¹
	C	10.80 ¹	14.37 ¹	21.21 ¹	37.79 ¹	61.80 ²	21.59 ¹	12.73 ¹
0.6%	UD	11.71 ¹	15.58 ¹	23.01 ¹	40.98 ¹	67.02 ²	23.42 ¹	13.80 ¹
	X	15.50 ¹	20.63 ¹	30.46 ¹	54.26 ¹	88.73 ²	31.00 ¹	18.27 ¹
	O	7.92 ¹	10.53 ¹	15.55 ¹	27.71 ¹	45.32 ²	15.83 ¹	9.33 ¹
	C	17.68 ¹	23.53 ¹	34.74 ¹	61.89 ¹	101.20 ²	35.36 ¹	20.84 ¹
0.9%	UD	15.61 ¹	20.77 ¹	30.66 ¹	54.62 ¹	89.32 ²	31.21 ¹	18.30 ¹
	X	21.29 ¹	28.33 ¹	41.83 ¹	74.52 ¹	121.87 ²	42.58 ¹	25.10 ¹
	O	9.92 ¹	13.20 ¹	19.49 ¹	34.72 ¹	56.78 ²	19.84 ¹	11.69 ¹
	C	24.56 ¹	32.68 ¹	48.25 ¹	85.96 ¹	140.57 ²	49.11 ¹	28.95 ¹

The superscript number indicates the mode number (m) of buckling.

From Figure 4.1 shows the effect of W_{GNP} and distribution pattern of graphene platelets on buckling strength of the FG-GRC plate. Figure 4.1, it is clearly illustrated that the buckling strength of the graphene reinforced plate has a significant effect by weight fraction, types of NUE loading and functional grading of graphene. For the same W_{GNP} content, the order of buckling load of the four patterns from low to high is FG-GRC O, UD, X and C. This is due to the more dispersion of graphene platelets towards the top and bottom surface of FG-GRC plate, which enhances the bending stiffness of the plate. Also, Figure 4.1 notifies that the percentage increase of buckling load with respect to load factor (α) remains the same. Where the buckling load increases 51.27% for FG-GRC_O when compared to the neat epoxy plate, 99.77% for FG-GRC_{UD}, 148.28% for FG-GRC_X and 176.15% for FG-GRC_C when the W_{GNP} is 0.3%. Similarly, 100% and 200% increases in the buckling strength of rectangular FG-GRC plate is observed for $W_{GNP} = 0.6\%$ and 0.9% respectively when compared to W_{GNP} is 0.3%.

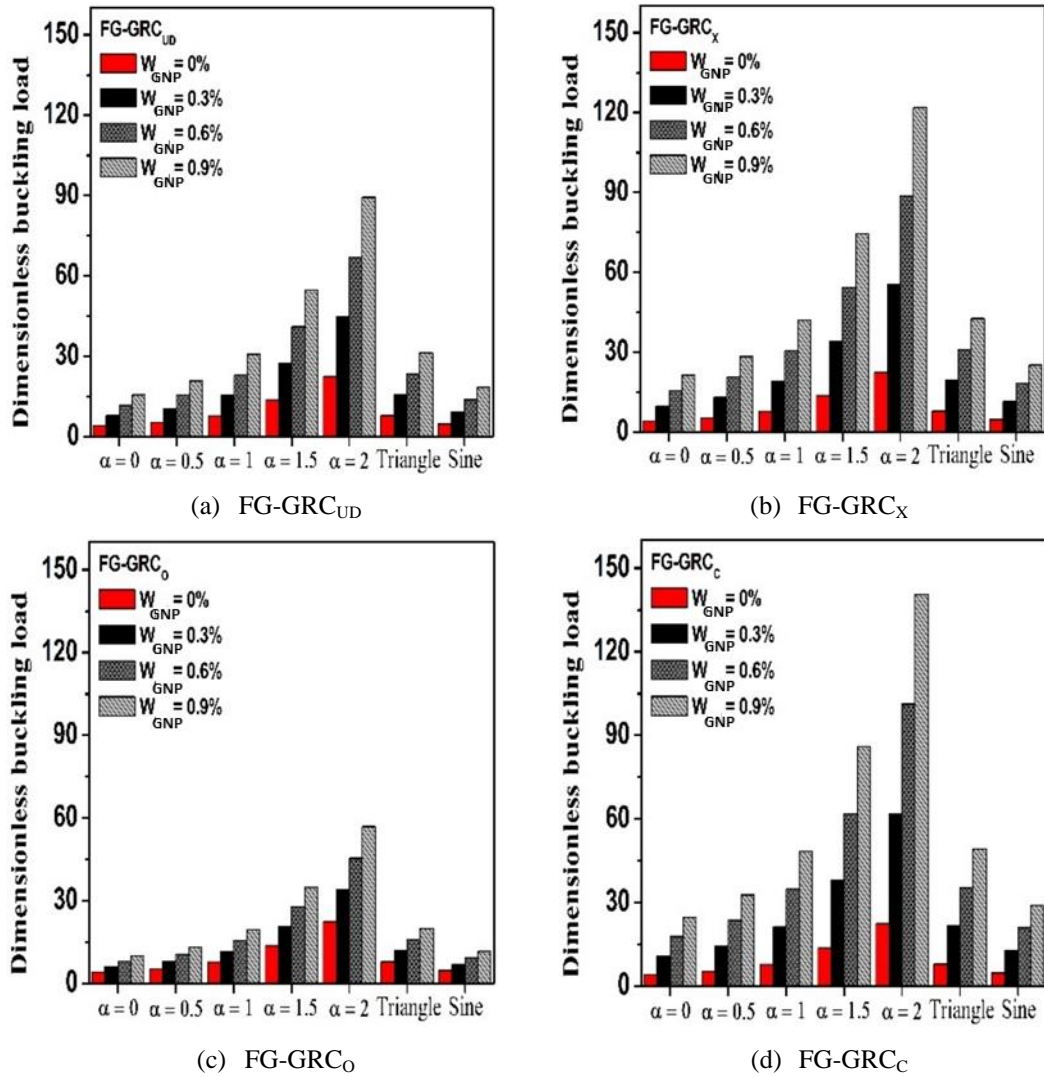


Figure 4.1: Effect of distribution pattern and weight fraction (W_{GNP}) on dimensionless buckling load of the FG-GRC plate under NUE load.

4.2.2. Effect of aspect ratio (a/b), GNP's pattern and weight fraction on dimensionless buckling load

The effect of aspect ratio (a/b) and functional grading of graphene platelets on the buckling strength of plate is shown in Figure 4.2. Four different dispersion patterns of GNP's are considered and noticed that similar order of buckling load increases (i.e., FG-GRC O, UD, X, and C when compared to the neat matrix) and the curve has a slight leftward excursion in the case of $\alpha = 2$ as seen in Figure 4.2 clearly. However, for the other cases very minor excursion of the curve is noted. This shows that for $\alpha = 2$ case the predicted buckling load possesses a small numeral value of half-waves towards the respective loading direction.

It is also noticed that FG-GRC plates with small a/b value have the least numeral value of half-waves in the buckling mode along the respective loading direction. For a larger aspect ratio, more numeral value of half-waves is witnessed in the buckling mode and critical load approaches a constant value. Figure 4.3 shows the weight fraction and aspect ratio (a/b) ratio influence on buckling load which highlights well known smoothen curve of buckling load for rectangular FG-GRC plate subjected to the uniform load when compared to the rest of the loading cases. Figure 4.4 shows the load factor (α) and aspect ratio influence on buckling strength and clearly denotes that load

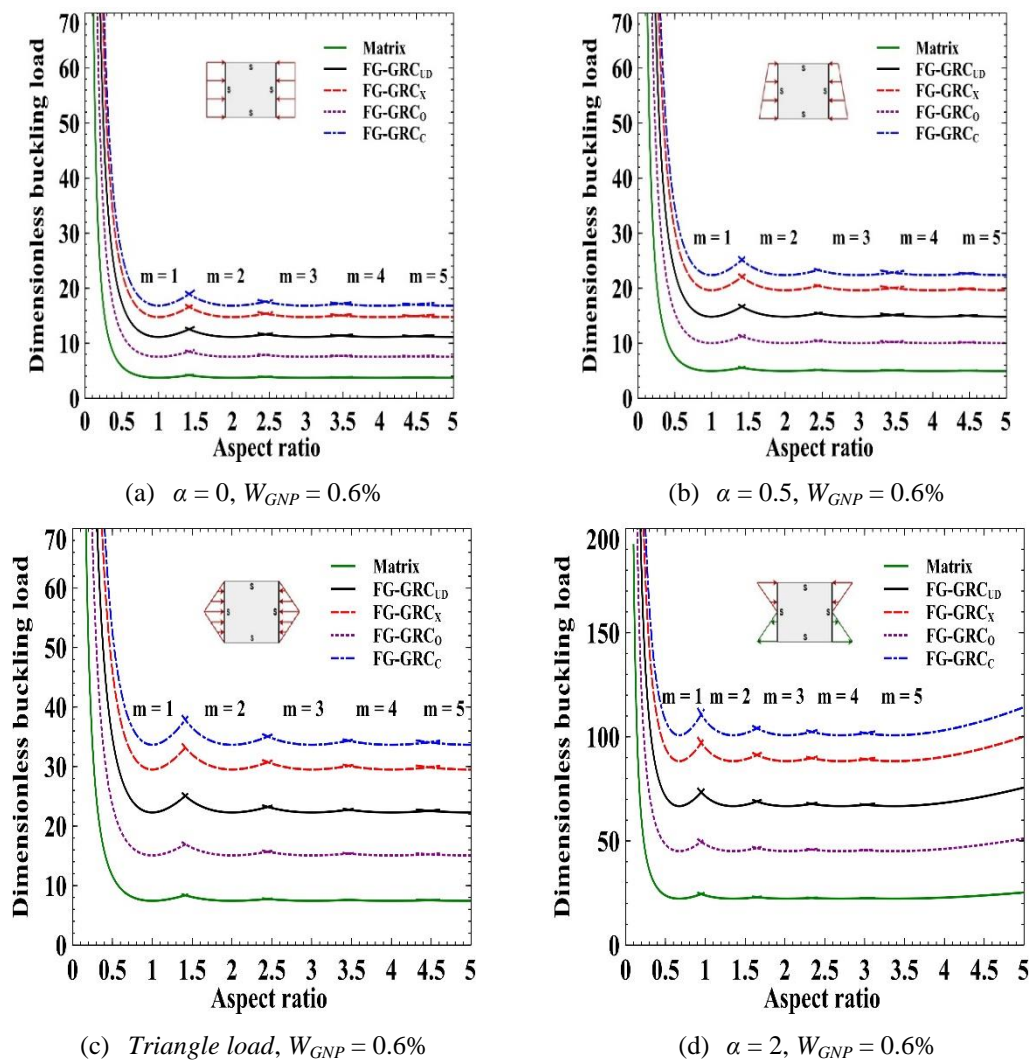
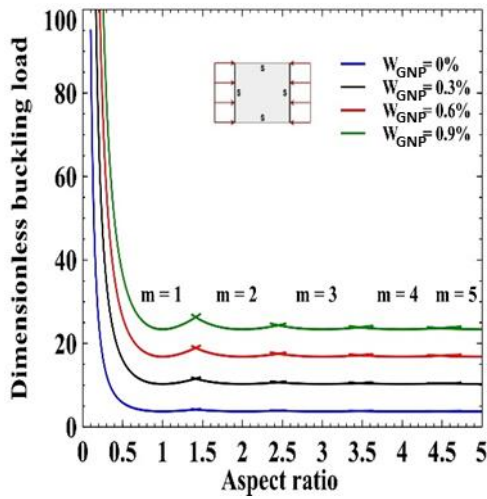
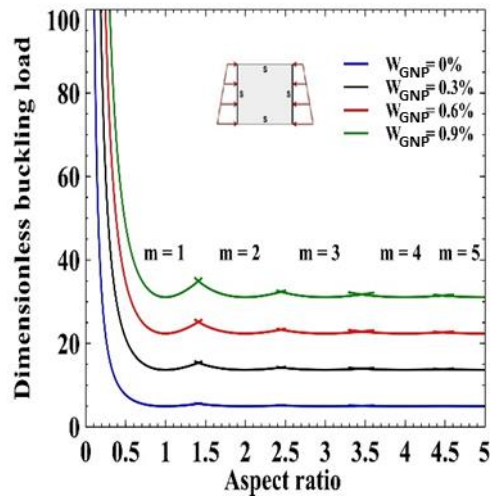


Figure 4.2: Effect of aspect ratio (a/b) and distribution pattern on dimensionless buckling load of FG-GRC plate under NUE load.

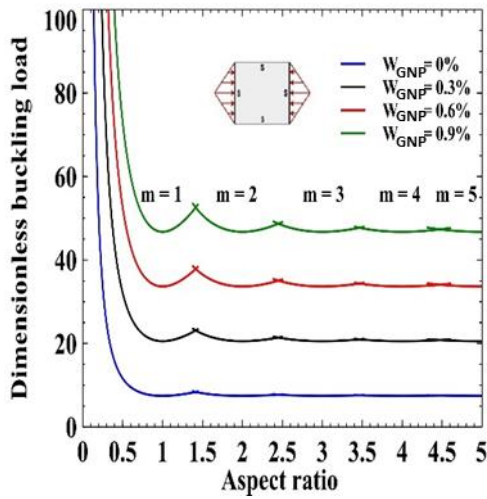
case with $\alpha=1$ and *triangle* load have close matching buckling curve trend. This is due to the fact that both load factors $\alpha=1$ and *triangle* loading has more or less same amount of load intensity. Furthermore, for $\alpha=1$ the load variation is antisymmetric while for the *triangle* case the load variation is symmetry.



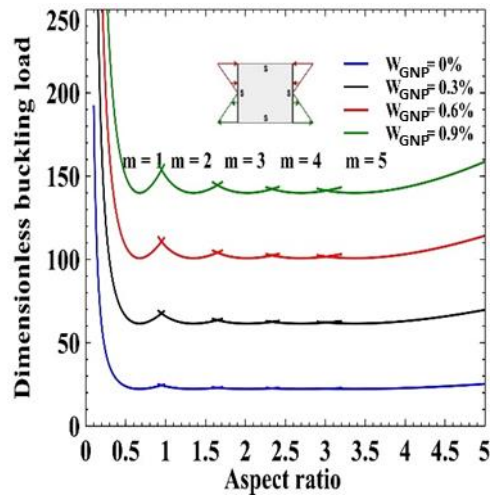
(a) $\alpha = 0$, FG-GRC_C



(b) $\alpha = 0.5$, FG-GRC_C

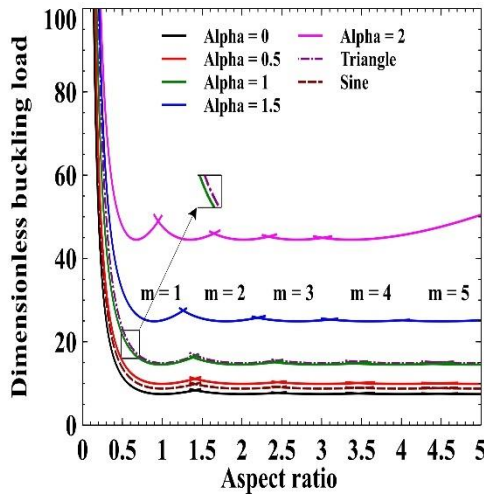


(c) *Triangle* load, FG-GRC_C

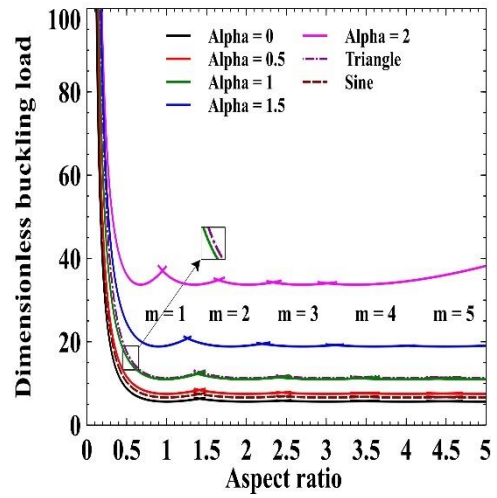


(d) $\alpha = 2$, FG-GRC_C

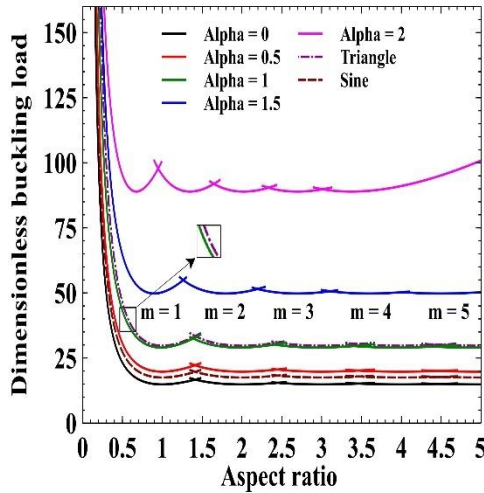
Figure 4.3: Effect of aspect ratio (a/b) and weight fraction W_{GNP} on dimensionless buckling load of FG-GRC plate under NUE load.



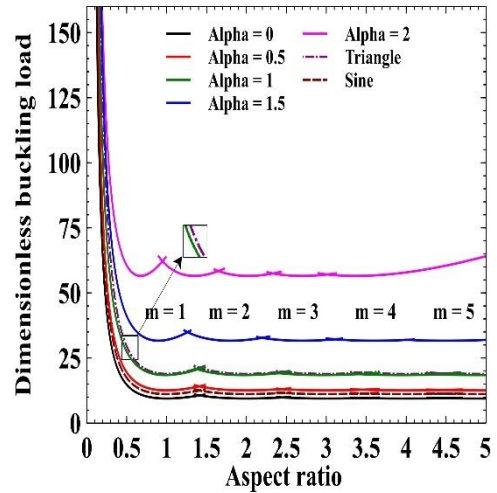
(a) FG-GRC_{UD}, $W_{GNP} = 0.3\%$



(b) FG-GRC_O, $W_{GNP} = 0.3\%$



(c) FG-GRC_{UD}, $W_{GNP} = 0.9\%$



(d) FG-GRC_O, $W_{GNP} = 0.9\%$

Figure 4.4: Effect of NUE load on aspect ratio (a/b) vs buckling load.

4.2.3. Effect of width to thickness ratio (b/h) on dimensionless buckling load

The variation of buckling strength of graphene reinforced plate under different NUE loading conditions with respect to a different width-thickness ratio ($b/h = 20, 50$ and 100) and different functional grading of $GNPs$ is shown in Figure 4.5. Similarly, the influence of b/h proportion and weight fraction of graphene platelets on a buckling load of FG-GRC_{UD} plate is shown in Figure 4.6. It clearly illustrates that the b/h ratio of rectangular FG-GRC plates has a substantial influence on buckling load. With a steady

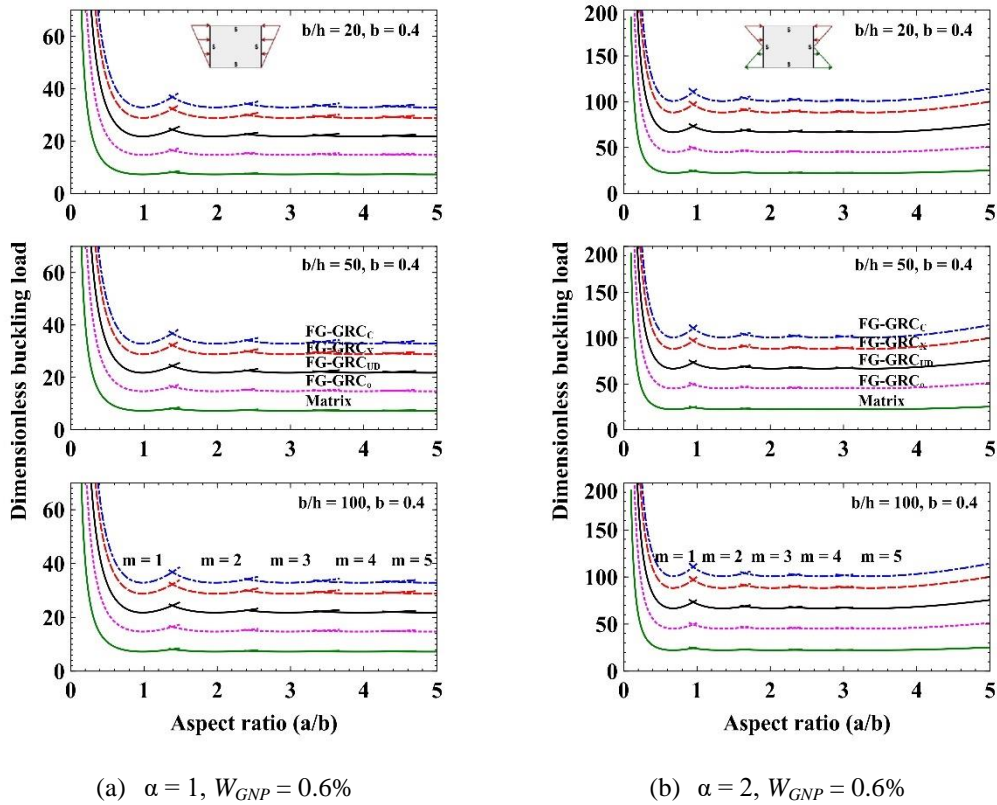


Figure 4.5: Effect of width to thickness ratio (b/h) and functional grading on the buckling load of the FG-GRC plate.

increase of b/h ratio, the stiffness effect of the rectangular FG-GRC plate is reduced which in turn causes a reduction in buckling strength.

4.3. Investigation on free vibration behaviour of the FG-GRC plate

4.3.1. Free vibration behaviour of the FG-GRC plate under NUE load

Deviations of dimensionless natural frequencies of first six modes with the increase in uniaxial compressive load for $\alpha=0$ and $\alpha=2$ are given in Figure 4.7. The natural frequency reduces due to increasing in compressive load for all loading cases are reported by numerous researchers. Natural frequency of the fundamental mode (1,1) approach zero when FG-GRC plate is subjected to corresponding buckling load as seen in Figure 4.8 to Figure 4.10. However, the NUE load case $\alpha=2$ is exceptional as the plate buckles with mode (2,1). It is noticed that the respective mode for which the natural frequency approaches zero frequency for the lowest uniaxial compressive load is called buckling mode. For $\alpha=2$ loading case, the buckling mode is (2,1). This is due to the fact that the presence of tensile force along half of the edge stabilizes the plate

while compressive force along the remaining half of the edge destabilizes it for $\alpha=2$ case.

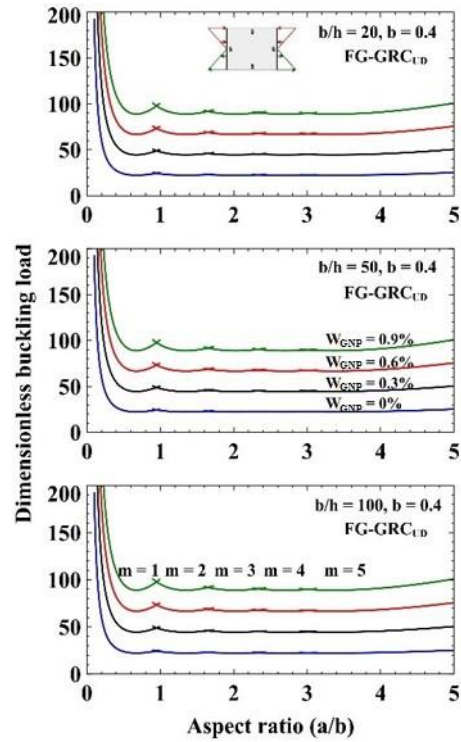


Figure 4.6: Effect of width to thickness ratio (b/h) and weight fraction on the buckling load of FG-GRC_{UD} plate under NUE load case $\alpha = 2$.

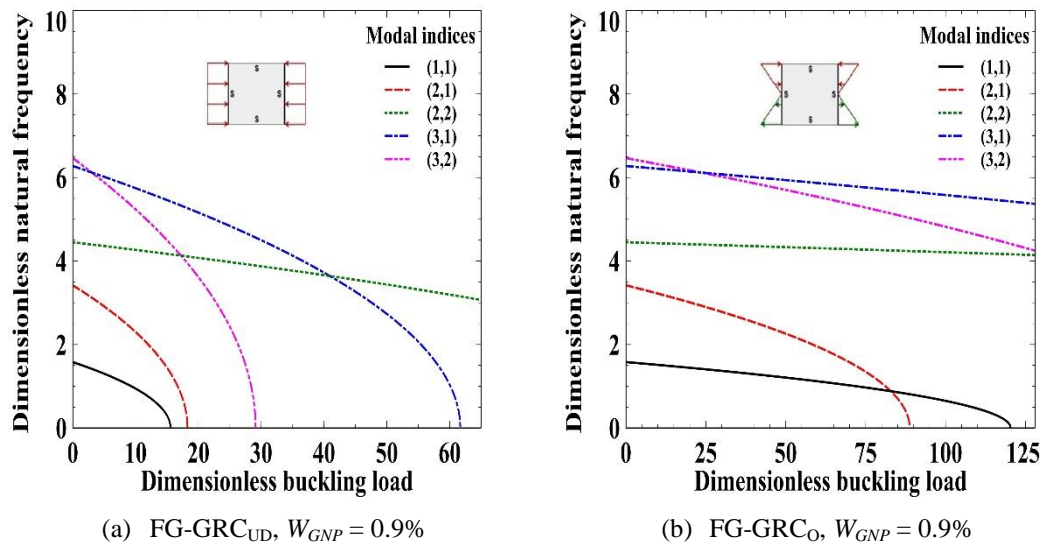


Figure 4.7: Effect of NUE load on free vibration frequencies.

4.3.2. Effect of *GNPs* pattern and weight fraction on dimensionless natural frequency

Effect of functional grading and weight fraction of *GNPs* on natural frequencies of FG-GRC plate shown in Figure 4.8. It is noted that distribution pattern has significant effect on the natural frequencies which is clearly shown in Figure 4.8 and similar order from buckling strength of FG-GRC plate from least to high (i.e., FG-GRC O, UD, X, and C) is also noticed same in rising of natural frequencies of graphene reinforced plate with respective functionally grading dispersion arrangement of *GNPs*. This order is formed due to the low dispersion of *GNPs* on the top and bottom layer for FG-GRC_O plate when compared to the UD, X and C pattern which results in a change in stiffness and mass of the FG-GRC plate as natural frequencies also varies. From Figure 4.8 and Figure 4.9 the interpretation of values signifies that the corresponding mode of natural frequency of plate can be enhanced up to 23%, 42% and 59% of FG-GRC_O plate for $W_{GNP} = 0.3, 0.6, 0.9\%$ respectively when compared to neat epoxy plate. However, it is 41%, 73% and 99% for FG-GRC_{UD} plate 57%, 98% and 133% for FG-GRC_X plate and 66%, 112% and 150% for FG-GRC_C plate. This is due to the physical properties of *GNPs* which tend to give higher stiffness to the FG-GRC plate. However, this stiffness effect tends to increase the overall stiffness of graphene reinforced plates because of increase in weight fraction of *GNPs*.

Figure 4.10 presents the effects of NUE load on natural frequencies of graphene reinforced plate. the natural frequency of a mode approach zero when the plate is subjected to corresponding buckling load as seen in Figure 4.10. the plate buckles with (1,1) mode for all the loading cases except for $\alpha = 2$ loading case under which the plate buckles with (2,1) mode, which is similar to the buckling characteristics.

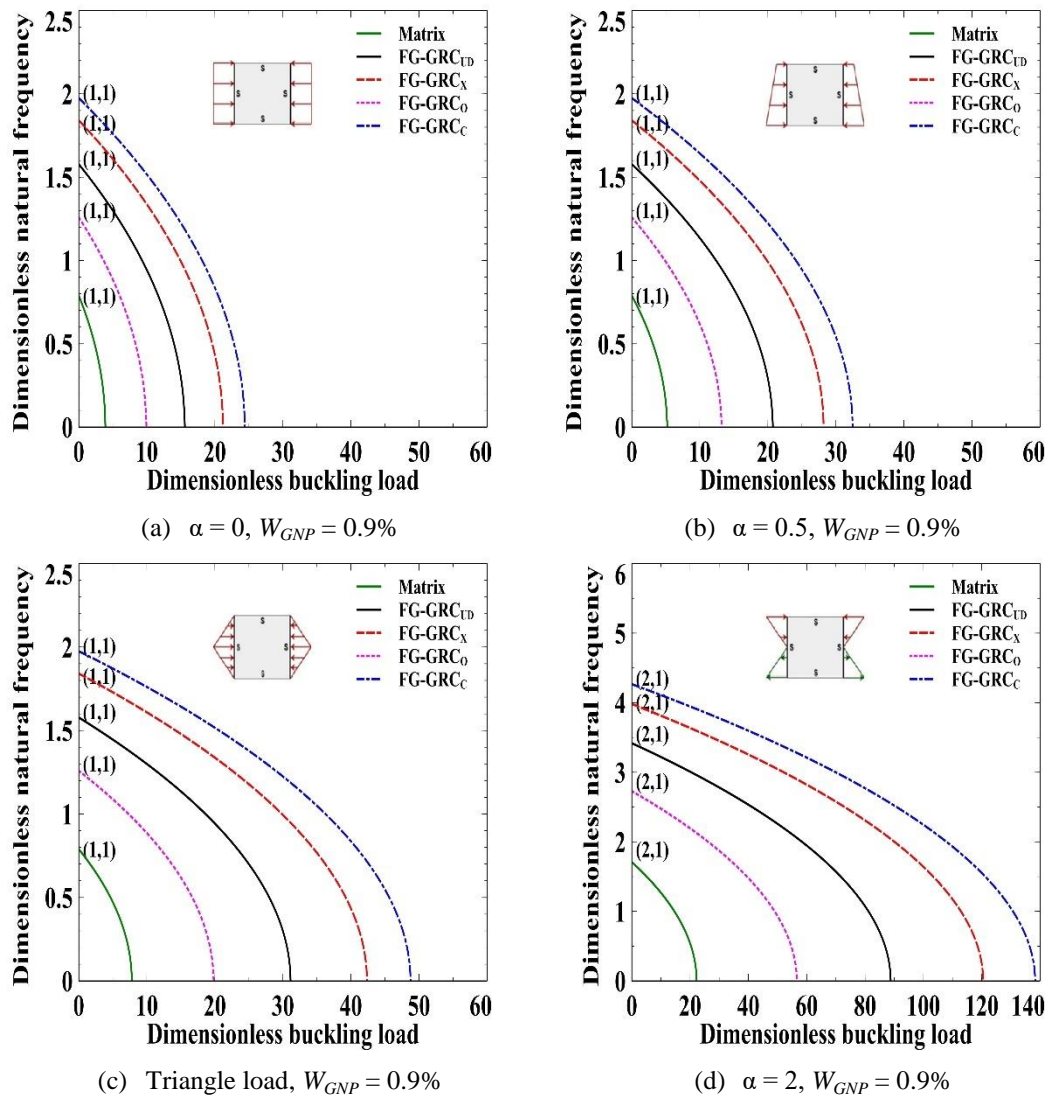
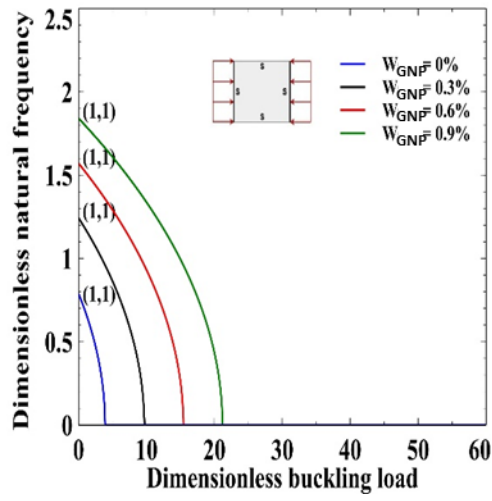
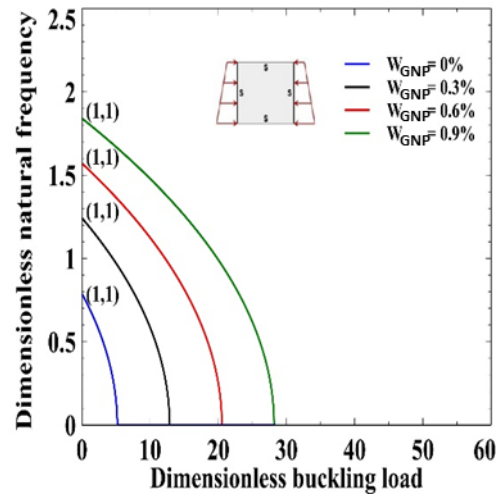


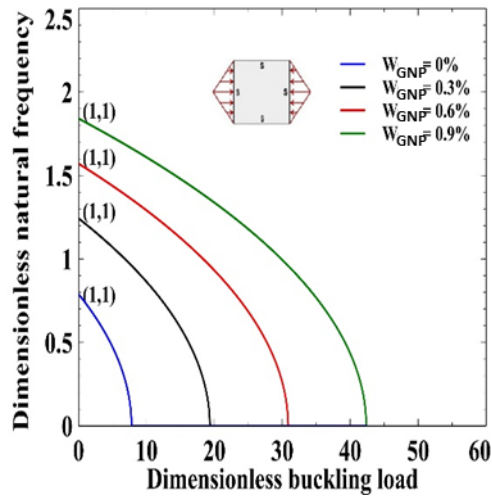
Figure 4.8: Effect of the distribution pattern of *GNPs* and NUE load on the fundamental natural frequency.



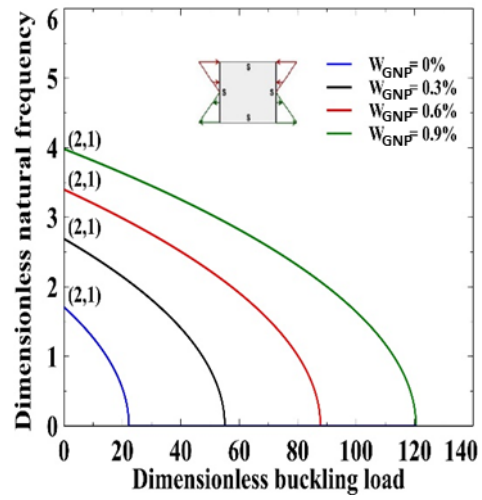
(a) $\alpha = 0$, FG-GRC_X



(b) $\alpha = 0.5$, FG-GRC_X

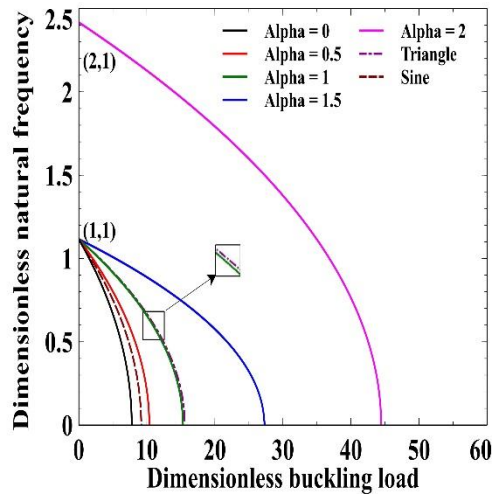


(c) *Triangle load*, FG-GRC_X

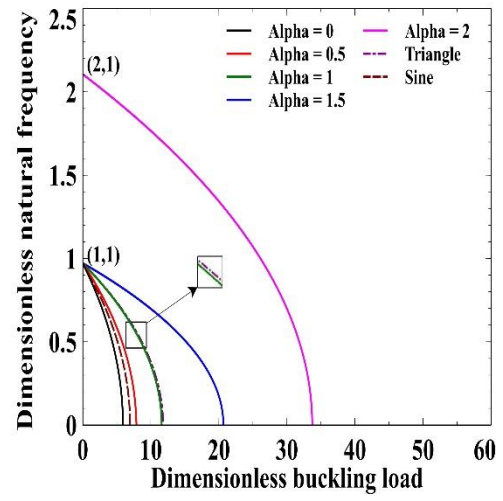


(d) $\alpha = 2$, FG-GRC_X

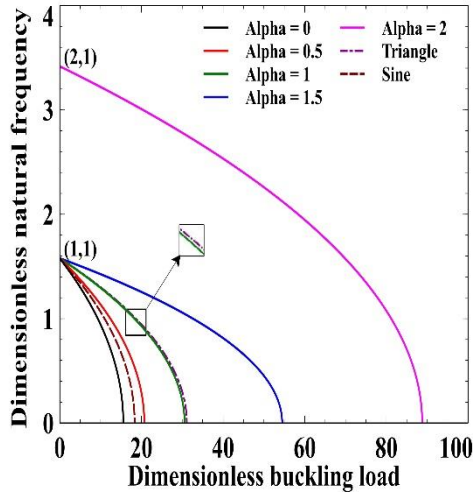
Figure 4.9: Effect of weight fraction and NUE load on the fundamental natural frequency of the FG-GRC plates.



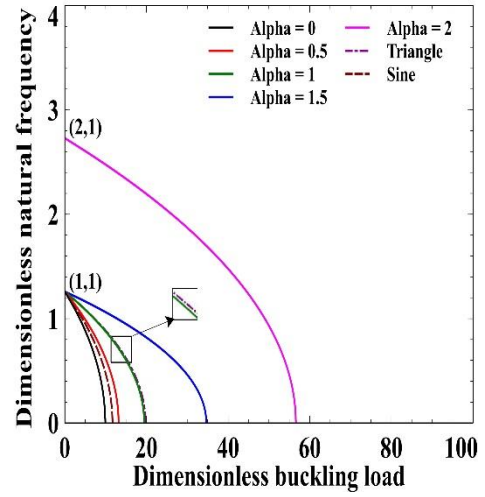
(a) FG-GRC_{UD}, $W_{GNP} = 0.3\%$



(b) FG-GRC_{UD}, $W_{GNP} = 0.3\%$



(c) FG-GRC_{UD}, $W_{GNP} = 0.9\%$



(d) FG-GRC_{UD}, $W_{GNP} = 0.9\%$

Figure 4.10: Effect of type of NUE load on the fundamental natural frequency of FG-GRC plates.

4.3.3. Effect of width to thickness ratio (b/h) on dimensionless natural frequency

Impact of width-thickness ratio ($b/h = 20, 50$ and 100) on natural frequencies of rectangular FG-GRC plate under NUE load is shown in Figure 4.11, which also illustrates that increase in b/h ratio decreases the stiffness of FG-GRC plate. Variation in the natural frequencies with respect to different types of $GNPs$ distribution pattern are shown in Figure 4.11. Similar behaviour is observed for the variations in weight fraction of $GNPs$, such that the natural frequencies decrease when the b/h ratio increases which are shown in Figure 4.12. Due to reduction in stiffness in thickness ratio ($b/h = 100$) has lower natural frequencies, when compared to the thickness ratio ($b/h = 10$) FG-GRC plate of higher natural frequencies. This clearly illustrates the similar behaviour of free vibration characteristics as observed in the buckling characteristics.

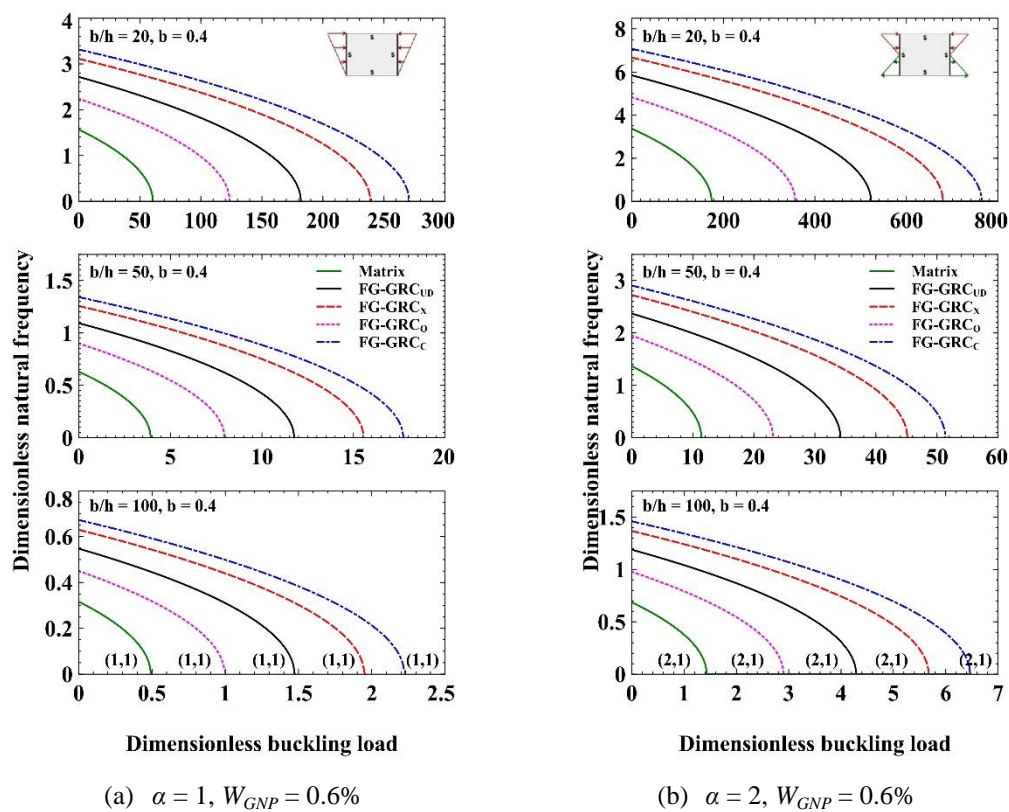


Figure 4.11: Effect of width to thickness ratio (b/h) and functional grading on the free vibration of the FG-GRC plate.

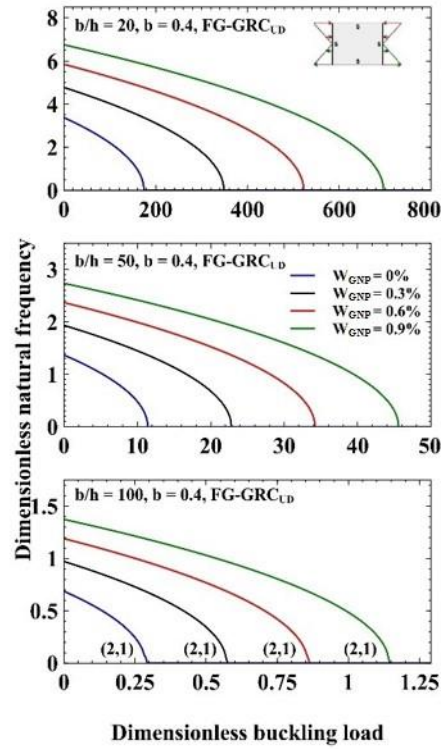


Figure 4.12: Effect of width to thickness ratio (b/h), weight fraction and NUE load on the natural frequency of FG-GRC plate.

4.4. Closure

Buckling and free vibration characteristics of different grading of graphene reinforced plates whose all edges are simply supported, which is subjected to different NUE loads are investigated based on analytical solutions. Influence of various important factors like nature of NUE loads, the weight fraction of graphene platelets, side to width aspect ratio (a/b), width to thickness aspect ratio (b/h) and nature of grading of GNP on buckling and free vibration frequencies are investigated. Based on a detailed analytical study, the critical buckling load parameter is significantly influenced by the nature of the NUE load. Due to the structural stability obtained by the combined effect of tensile and compressive forces $\alpha=2$ load case results in higher buckling load. The fundamental buckling mode for $\alpha=2$ load case is (2,1) while for the remaining load case it is (1,1). It is noted that minute increase in W_{GNP} of $GNPs$ results in a significant increase of the stiffness parameter of rectangular FG-GRC plate, as an outcome it leads to increase in buckling load and natural frequencies. The distribution pattern of $GNPs$ for a given fraction of GNP has a huge impact on the stiffness

parameter of the rectangular FG-GRC plate. It is noted that the FG-GRC_C pattern shows the superior buckling and free vibration characteristics when compared to the other cases due to the enhanced bending stiffness associated with FG-GRC_C pattern.

CHAPTER 5

5. VIBRO-ACOUSTIC STUDIES OF FG-GRC PANEL UNDER NON-UNIFORM UNIAXIAL EDGE LOADS

5.1. Introduction

The NUE loads create the in-plane mechanical pre-stress and changes the stiffness and dynamic properties of the FG-GRC structure. So, it is crucial to analyse dynamic and acoustic response of structure subjected to nonuniform compressive loads subjected to steady-state mechanical excitation for the better design consideration. In this current analytical investigation, the effective material properties of FG-Graphene reinforced plate with different grading patterns and weight percentage of *GNPs* are obtained by grouping of modified Halpin-Tsai model and rule of mixture.

In the current investigation an FG-Graphene reinforced plate whose all edges are simply supported is considered. It is presumed that the FG-Graphene reinforced plate consists of 12 *GNPs* layers by considering real time manufacturing criteria. The plate is investigated for three aspect ratios $(a/b) = 0.5, 1.25 \text{ \& } 2$ with the constant slenderness ratio $(b/h = 100)$ by maintaining constant value of $b = 0.4$ m. The material properties for the *GNPs* reinforcement and polymer matrix given in Table 2.2 are considered. The combined effects of type of NUE loading, *GNPs* grading patterns, weight fraction percentage of *GNPs*, aspect ratio (a/b) and slenderness ratio (b/h) of FG-Graphene reinforced plate on the vibration and acoustic responses are detailly studied. Initially the buckling load ratios for different NUE load cases are calculated in order to find dynamic response as a function of the edge load intensity and the results are given in Table 5.1.

Table 5.1: Buckling load ratio of FG-GRC plate under NUE loads.

Aspect ratio (a/b)	Types of NUE loads						
	0	0.5	1	1.5	2	Triangle	Sine
0.5	1 ¹	0.7568 ¹	0.5370 ¹	0.3590 ¹	0.2436 ¹	0.5002 ¹	0.8485 ¹
1.25	1 ¹	0.7515 ¹	0.5091 ¹	0.2858 ¹	0.2059 ²	0.4996 ¹	0.8502 ¹
2	1 ²	0.7521 ²	0.5120 ²	0.2956 ²	0.1961 ³	0.5018 ²	0.8550 ²

The mode number(m) of respective buckling case is donated by the superscript number.

For the acoustic response, FG-GRC plate is presumed to be vibrating in air medium ($\rho_o=1.21 \text{ kg/m}^3$ and $c_o=343 \text{ m/s}$). A constant loss factor of 0.01 is assumed for all the response analysis. A 20 x 20 mesh division is considered for the acoustic response analysis based on the convergence studies which also satisfies the condition of “six element per wavelength” requirement for the numerical vibro-acoustic analysis. Also, frequency resolution study is done and based on that 0.5 Hz frequency resolution is adopted for the response studies. The dimensionless buckling load, exciting frequency and average RMS velocity are analysed and they are defined as

$$\bar{P}_{cr} = P_{cr}^x \left(\frac{b^2}{E_m \pi^2} \right) \times 10^8 \quad (5.1)$$

$$\bar{\omega}_{mn} = \omega_{mn} \sqrt{\frac{\rho_m}{E_m}} \left(\frac{b^2}{\pi^2} \right) \times 10^3 \quad (5.2)$$

$$\bar{V}_{rms} = V_{rms} \left(\frac{E_m h^3}{b^4 F_o} \right) \times 10^{-5} \quad (5.3)$$

5.2. Investigation of *GNPs* grading and weight fraction under no load condition

Influence of the slenderness ratio, dispersion pattern and weight fraction of *GNPs* on the forced vibration response (spatially averaged RMS velocity) of the FG-GRC plate without any pre-stress is studied first and results are given in Figure 5.1. A rectangular FG-GRC plate with the dimensions of 0.5 x 0.4 x ($b/h = 50, 100 \text{ \& } 200$) m³ is considered for this study. It is noticed that the amplitude of the resonating peak reduces and shifting rightwards with increase in the slenderness ratio and weight fraction of the *GNPs*, due to the structural stiffness enhancement. In the case of dispersion grading pattern of *GNPs*, FG-GRC_C has higher stiffness when compared to other grading patterns and neat epoxy plate. Based on this study, FG-Graphene reinforced plate with slenderness ratio of $b/h = 100$ has been selected for the detailed vibro-acoustic response studies on FG-Graphene reinforced plate subjected to the NUE loads and subjected to steady state harmonic excitation.

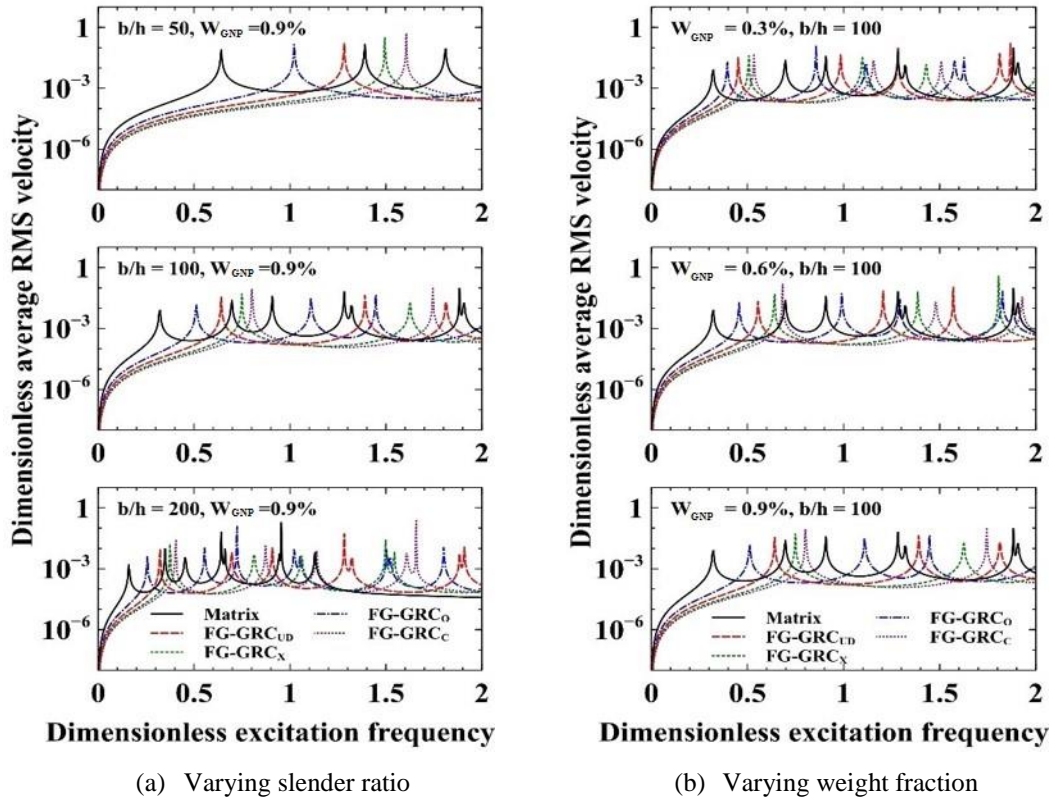


Figure 5.1: Effect of slenderness ratio (b/h) and weight percentage of GNP on different dispersion pattern of FG-GRC plate.

5.3. Buckling response of FG-GRC plate under NUE load

The buckling load ratios for the FG-GRC plate with different aspect ratios are given in Table 5.1. Effects of dispersion pattern, the weight fraction of $GNPs$ and aspect ratio (a/b) on the dimensionless buckling load of the FG-Graphene reinforced plates under the different NUE loads are given in Table 5.2. Third order approximation is used to obtain the buckling load for $\alpha=2$ case while second order approximation is used to obtain the buckling load for the remaining cases. It is observed that nature of NUE load along with the aspect ratios (a/b) of the plate has a huge impact on the dimensionless buckling loads. From Table 5.2, it is evident that dimensionless buckling load increases with the load factor (α) values, the increase in tensile forces and nonuniform intensity of the load configuration enhances buckling resilience of FG-Graphene reinforced plate. Due to this buckling resistance of FG-Graphene reinforced plate increases for the NUE loads compared to the typical uni-axial compression.

Table 5.2: Dimensionless buckling load of FG-graphene reinforced plate.

W_{GNP}	Pattern	Aspect ratio (a/b)	Aspect					Triangle	Sine
			0	0.5	1	1.5	2		
0%	Matrix	0.5	3.78 ¹	4.99 ¹	7.03 ¹	10.52 ¹	15.50 ¹	7.55 ¹	4.45 ¹
		1.25	2.54 ¹	3.38 ¹	4.99 ¹	8.88 ¹	14.53 ²	5.08 ¹	2.99 ¹
		2	2.42 ²	3.21 ²	4.72 ²	8.17 ²	14.46 ³	4.83 ²	2.85 ²
0.3%	UD	0.5	7.54 ¹	9.97 ¹	14.05 ¹	21.01 ¹	30.96 ¹	15.08 ¹	8.89 ¹
		1.25	5.07 ¹	6.75 ¹	9.96 ¹	17.75 ¹	29.02 ²	10.14 ¹	5.98 ¹
		2	4.83 ²	6.42 ²	9.43 ²	16.33 ²	28.90 ³	9.65 ²	5.69 ²
	X	0.5	9.37 ¹	12.39 ¹	17.46 ¹	26.12 ¹	38.48 ¹	18.74 ¹	11.05 ¹
		1.25	6.30 ¹	8.39 ¹	12.38 ¹	22.06 ¹	36.07 ²	12.60 ¹	7.43 ¹
		2	6.00 ²	7.98 ²	11.72 ²	20.30 ²	35.91 ³	12.00 ²	7.07 ²
	O	0.5	5.71 ¹	7.55 ¹	10.64 ¹	15.91 ¹	23.45 ¹	11.42 ¹	6.73 ¹
		1.25	3.84 ¹	5.11 ¹	7.54 ¹	13.44 ¹	21.98 ²	7.68 ¹	4.53 ¹
		2	3.66 ²	4.86 ²	7.14 ²	12.37 ²	21.88 ³	7.31 ²	4.31 ²
C	0.5	10.43 ¹	13.78 ¹	19.42 ¹	29.05 ¹	42.80 ¹	20.85 ¹	12.29 ¹	
	1.25	7.01 ¹	9.33 ¹	13.77 ¹	24.53 ¹	40.12 ²	14.02 ¹	8.26 ¹	
	2	6.67 ²	8.87 ²	13.03 ²	22.57 ²	39.94 ³	13.34 ²	7.87 ²	
0.6%	UD	0.5	11.31 ¹	14.94 ¹	21.06 ¹	31.50 ¹	46.42 ¹	22.61 ¹	13.33 ¹
		1.25	7.60 ¹	10.12 ¹	14.94 ¹	26.61 ¹	43.51 ²	15.20 ¹	8.96 ¹
		2	7.24 ²	9.62 ²	14.14 ²	24.48 ²	43.32 ³	14.47 ²	8.53 ²
	X	0.5	14.97 ¹	19.78 ¹	27.87 ¹	41.70 ¹	61.45 ¹	29.93 ¹	17.64 ¹
		1.25	10.07 ¹	13.39 ¹	19.77 ¹	35.22 ¹	57.60 ²	20.13 ¹	11.86 ¹
		2	9.58 ²	12.74 ²	18.71 ²	32.41 ²	57.34 ³	19.16 ²	11.29 ²
	O	0.5	7.65 ¹	10.10 ¹	14.24 ¹	21.30 ¹	31.39 ¹	15.29 ¹	9.01 ¹
		1.25	5.14 ¹	6.84 ¹	10.10 ¹	17.99 ¹	29.42 ²	10.28 ¹	6.06 ¹
		2	4.89 ²	6.51 ²	9.56 ²	16.55 ²	29.29 ³	9.78 ²	5.77 ²
C	0.5	17.07 ¹	22.56 ¹	31.79 ¹	47.57 ¹	70.09 ¹	34.14 ¹	20.12 ¹	
	1.25	11.48 ¹	15.28 ¹	22.55 ¹	40.17 ¹	65.69 ²	22.95 ¹	13.53 ¹	
	2	10.93 ²	14.53 ²	21.34 ²	36.96 ²	65.40 ³	21.85 ²	12.88 ²	
0.9%	UD	0.5	15.07 ¹	19.91 ¹	28.06 ¹	41.98 ¹	61.86 ¹	30.13 ¹	17.76 ¹
		1.25	10.13 ¹	13.48 ¹	19.91 ¹	35.46 ¹	57.98 ²	20.26 ¹	11.94 ¹
		2	9.64 ²	12.82 ²	18.84 ²	32.63 ²	57.73 ³	19.28 ²	11.37 ²
	X	0.5	20.56 ¹	27.17 ¹	38.29 ¹	57.28 ¹	84.40 ¹	41.11 ¹	24.23 ¹
		1.25	13.82 ¹	18.40 ¹	27.16 ¹	48.38 ¹	79.11 ²	27.64 ¹	16.29 ¹
		2	13.16 ²	17.50 ²	25.70 ²	44.51 ²	78.76 ³	26.31 ²	15.51 ²
	O	0.5	9.58 ¹	12.66 ¹	17.84 ¹	26.69 ¹	39.32 ¹	19.15 ¹	11.29 ¹
		1.25	6.44 ¹	8.57 ¹	12.65 ¹	22.54 ¹	36.86 ²	12.88 ¹	7.59 ¹
		2	6.13 ²	8.15 ²	11.97 ²	20.74 ²	36.70 ³	12.26 ²	7.23 ²
C	0.5	23.72 ¹	31.34 ¹	44.16 ¹	66.07 ¹	97.35 ¹	47.42 ¹	27.95 ¹	
	1.25	15.95 ¹	21.22 ¹	31.33 ¹	55.80 ¹	91.25 ²	31.88 ¹	18.79 ¹	
	2	15.18 ²	20.18 ²	29.65 ²	51.34 ²	90.85 ³	30.35 ²	17.89 ²	

The mode number (m) of respective buckling case is denoted by the superscript number.

Load factor $\alpha=2$ case tends to have the maximum critical buckling load when compared to other cases as half of the plate edge is subjected to the tensile force which increases buckling strength of the FG-Graphene reinforced plate. Vibro-acoustic response analysis of FG-Graphene reinforced plate is carried out using the buckling load ratio values given in Table 5.1 as discussed in the methodology section.

Table 5.2 shows that the nature of distribution and weight fraction of $GNPs$ has a significant effect on the buckling strength of the FG-Graphene reinforced plate. For the given W_{GNP} percentage, effect of dispersion pattern on the buckling load in ascending order is as follows FG-GRC C, X, UD and O. This is due to variation of stiffness of the FG-GRC plate according to the nature of distribution of $GNPs$ through the thickness. The buckling load increases 176.15, 148.28, 99.77, and 51.27% for FG-GRC C, X, UD and O for $W_{GNP}=0.3\%$, when compared to neat epoxy plate. Likewise, 100% and 200% improvement in the buckling strength is obtained for $W_{GNP}=0.6\%$ and 0.9% respectively when compared to the $W_{GNP}=0.3\%$. With regard to the aspect ratio (a/b) effect, it is observed that for the plates with smaller aspect ratio the critical buckling load is high and the buckling mode possess a smaller number of half-sine waves along the loading direction. However, vice-versa buckling behaviour is observed for the FG-GRC plates with higher aspect ratio. It is also observed that buckling strength of the FG-GRC plates under *triangle* load is very close to the buckling load under $\alpha=1$ case as seen in the case of metallic plate.

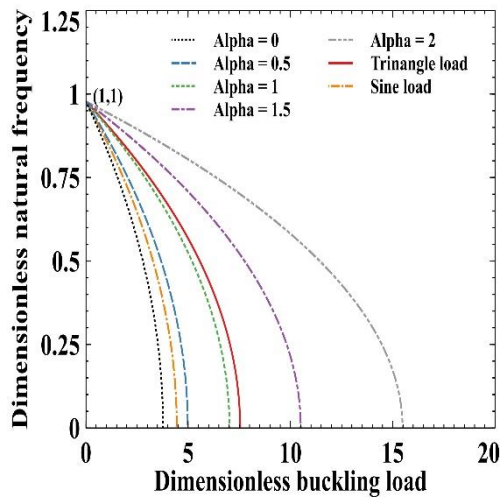
5.4. Vibration response of FG-GRC plate under NUE load

5.4.1. Free vibration characteristics

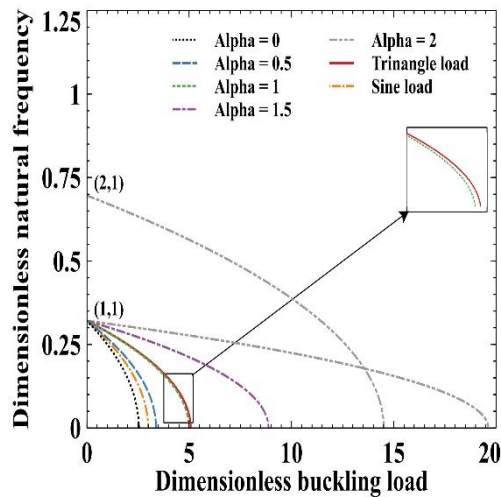
Variation of dimensionless fundamental natural frequency of the FG-GRC plate with the increase in magnitude of NUE loads for different aspect ratio, W_{GNP} and the dispersion pattern are shown in Figure 5.2. The natural frequency reduces with increase in the load as observed earlier for the isotropic plate. From Figure 5.2, it is observed that the natural frequency of a particular plate reduces to zero when the compressive load is equal to the corresponding buckling load. It is also noticed from Figure 5.2 that the fundamental frequency of plates with higher a/b aspect ratio approaches zero has mode with higher modal indices (2,1) not (1,1). This also

indicates that the modal indices of the free vibration mode at buckling load is same as that of the fundamental buckling mode. When the value of aspect ratio (a/b) is 0.5 the FG-GRC plate buckles with (1,1) mode for all the load factor cases. However, for $a/b= 1.25$ the plate buckles with (1,1) mode for all non-uniform load cases, except for $\alpha=2$ case for which the plate buckles with (2,1) mode due combined effect of tensile and compressive load for $\alpha=2$ case and larger length dimensions of the FG-GRC plate along the loading direction. Similarly, for the plates with higher aspect ratio, the plate buckles with higher modal indices. For example, for $a/b= 2$ the plate buckled with (3,1) for $\alpha = 2$ case and with (2,1) mode for the other load cases.

Effects of different dispersion pattern and weight fraction (W_{GNP}) of the GNPs on natural frequencies are also shown in Figure 5.2. It is noticed that the dispersion pattern has significant effect on the natural frequencies of the FG-GRC plate. The increase of the fundamental natural frequencies of the FG-GRC plate from least to higher are in the order of FG-GRC O, UD, X and C. As a result of the less amount of GNPs distribution near the outer surface of the polymer matrix results in lower stiffness for the FG-GRC_O pattern compared to other dispersion patterns. However, due to a greater number of GNPs on outer extreme surfaces compared to the neutral axis, FG-GRC_C has better buckling resistance compared to the other patterns.

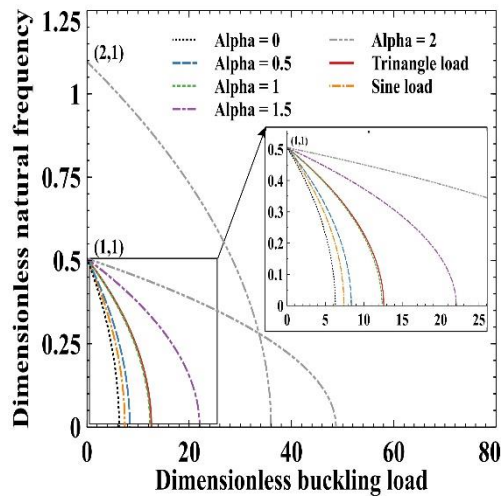


(a) Aspect ratio = 0.5, $W_{GNP} = 0\%$ (Matrix)

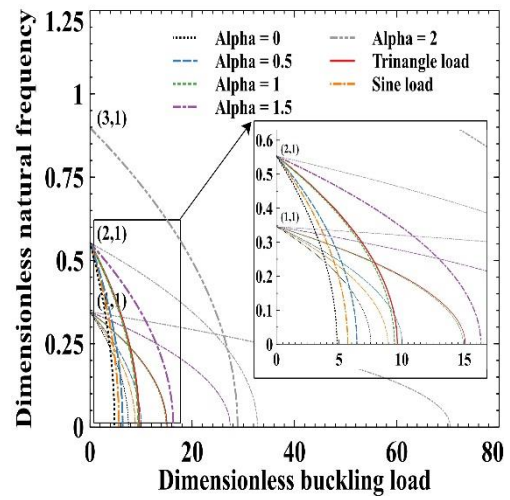


(b) Aspect ratio = 1.25, $W_{GNP}=0\%$ (Matrix)

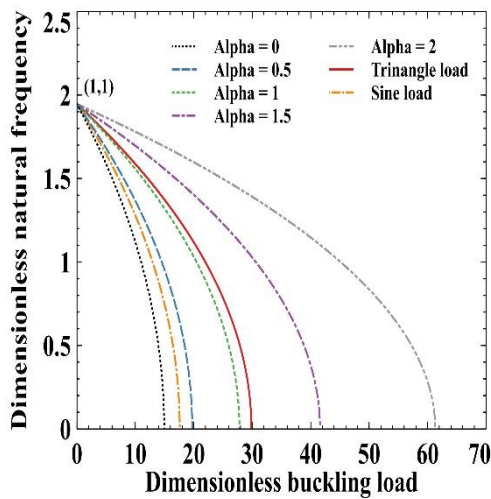
Continued...



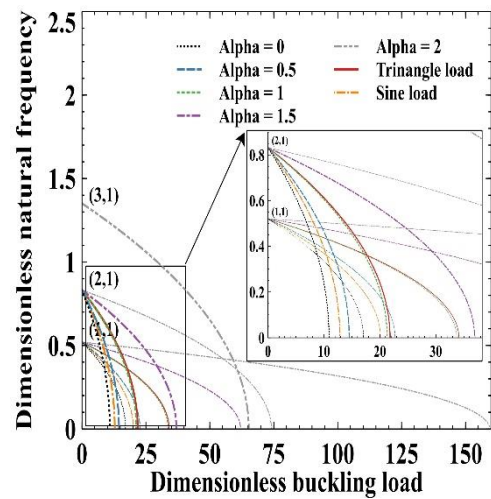
(c) Aspect ratio = 1.25, $W_{GNP} = 0.3\%$ (FG-GRC_X)



(d) Aspect ratio = 2, $W_{GNP} = 0.3\%$ (FG-GRC_{UD})

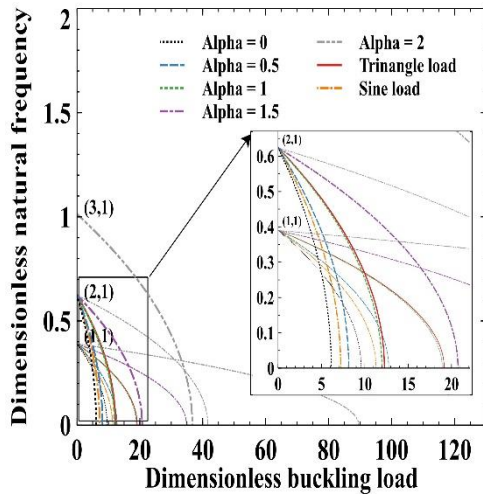


(e) Aspect ratio = 0.5, $W_{GNP} = 0.6\%$ (FG-GRC_X)

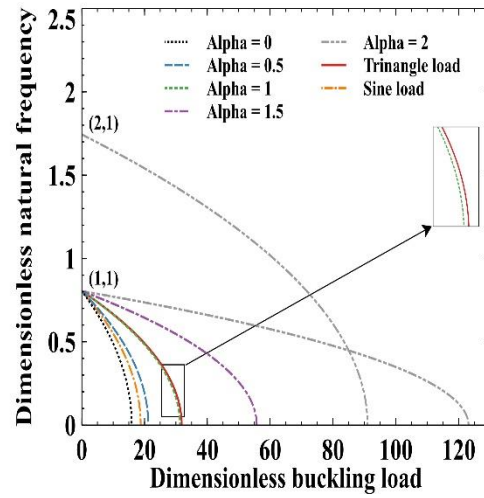


(f) Aspect ratio = 2, $W_{GNP} = 0.6\%$ (FG-GRC_C)

Continued...



(g) Aspect ratio = 2, $W_{GNP} = 0.9\%$ (FG-GRC_O)



(h) Aspect ratio = 1.25, $W_{GNP} = 0.9\%$ (FG-GRC_C)

Figure 5.2: Effect of NUE loads on dimensionless natural frequency.

Basically, the *GNPs* distribution pattern affects the bending moment of inertia and hence stiffness of the plate. A plate with the aspect ratio of 1.25 subjected to $\alpha=2$ load case is investigated to demonstrate the influence of increase in intensity of NUE load on the free vibration mode shifting behaviour. Effect of increase in axial load on natural frequencies and mode shapes of first two lowest frequencies of plate with aspect ratio 1.25 and $\alpha=2$ load case is shown in Figure 5.3. It is observed that the plate has the typical symmetric mode shapes of (1,1) and (2,1) under the no load condition, where (1,1) has the least natural frequency value when compared to the (2,1) mode. However, with the increase in the magnitude of the applied NUE load, it is found that jumping of the mode shapes occurs when the magnitude of the applied NUE load is around the buckling load. Because of this, natural frequency associated with (2,1) mode approaches zero earlier compared to the (1,1) mode. For $\alpha=2$ load case, the upper side of the plate is subjected to tensile load and the lower side is under compressive load. This leads to moving of anti-nodal positions towards the bottom of the plate with the increase in magnitude of the applied load.

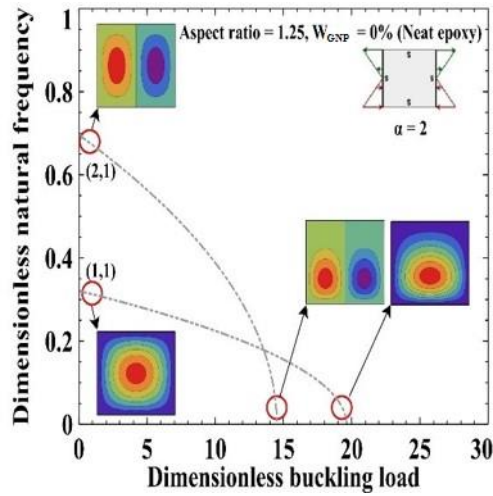
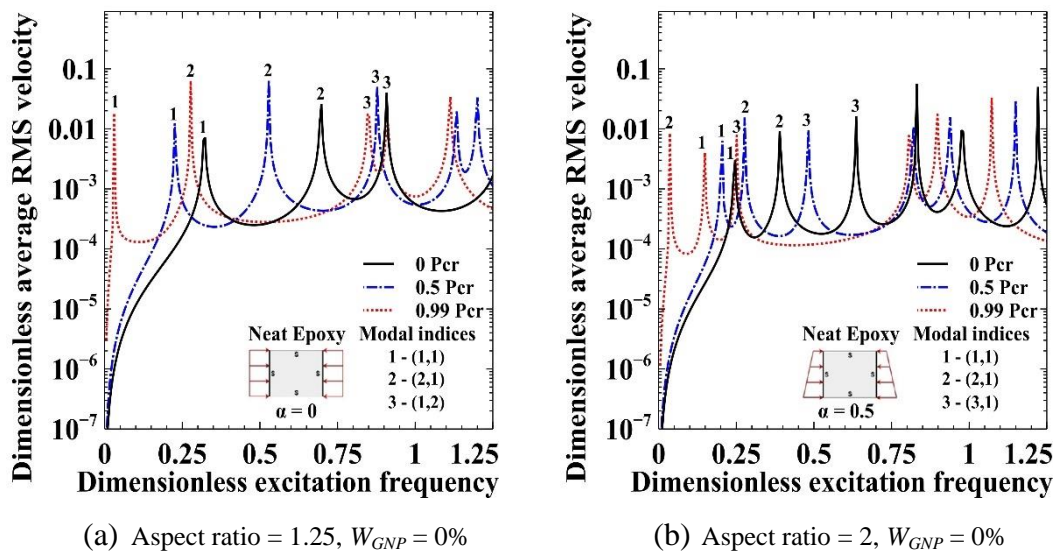


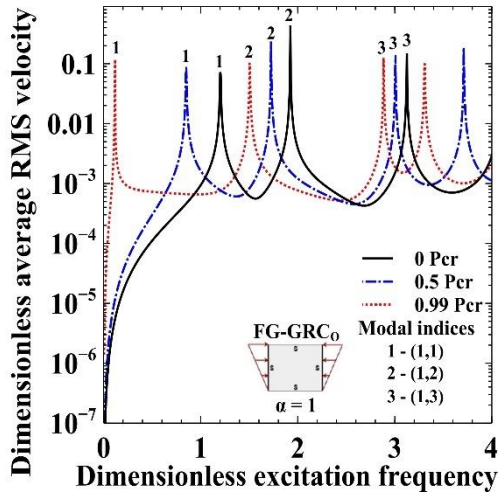
Figure 5.3: Effect of NUE loads on the mode shapes.

5.4.2. Forced vibration characteristics

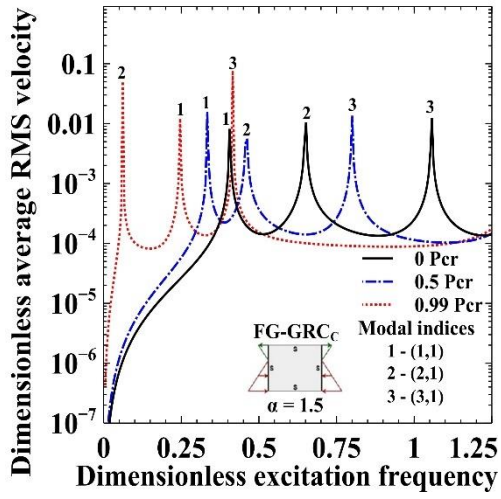
Forced vibration response of FG-Graphene reinforced plate subjected to NUE load and subjected to steady state mechanical harmonic excitation has been investigated in this section. For this, the FG-GRC plate is excited with a time dependent sinusoidal force of 1N in the frequency range of 0 to 1600 Hz along the frequency resolution value of 0.5 Hz at $(a/4, b/4)$ from the origin. The upper limit of excitation frequency is selected as 1600 Hz such that the acoustic coincidence frequency of the plate lies within the selected range. To investigate the impact of mode shifting on the response characteristics, the first ten modes have been considered throughout the investigation.



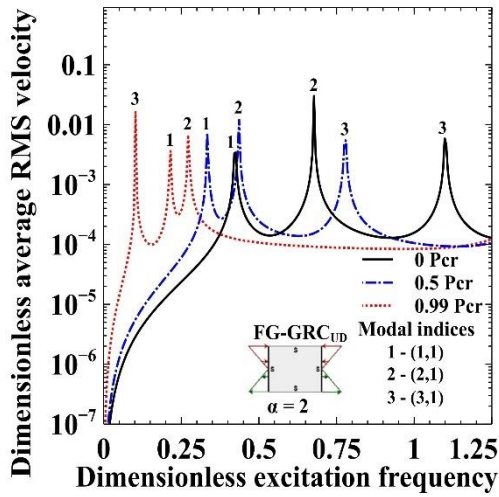
Continued...



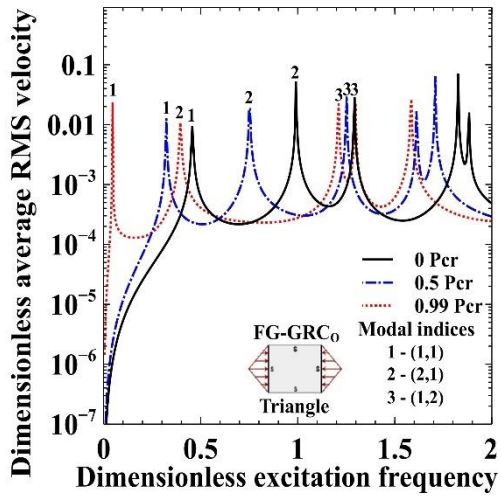
(c) Aspect ratio = 0.5, $W_{GNP} = 0.3\%$



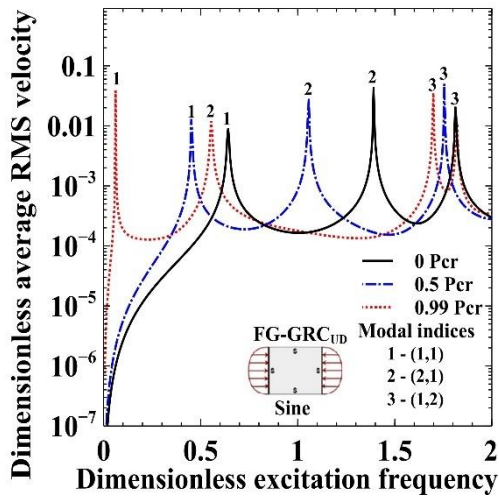
(d) Aspect ratio = 2, $W_{GNP} = 0.3\%$



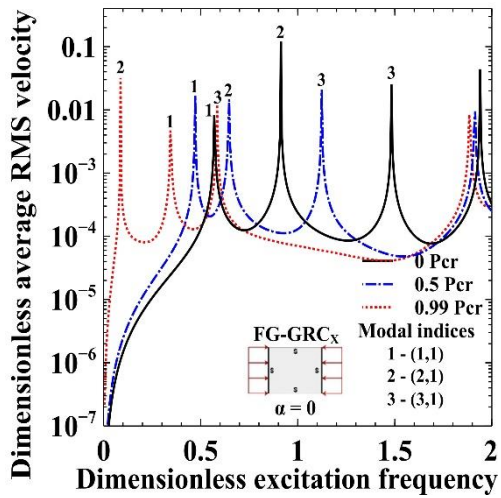
(e) Aspect ratio = 2, $W_{GNP} = 0.6\%$



(f) Aspect ratio = 1.25, $W_{GNP} = 0.6\%$



(g) Aspect ratio = 1.25, $W_{GNP} = 0.9\%$



(h) Aspect ratio = 2, $W_{GNP} = 0.9\%$

Figure 5.4: Effect of NUE loads on dimensionless average RMS velocity.

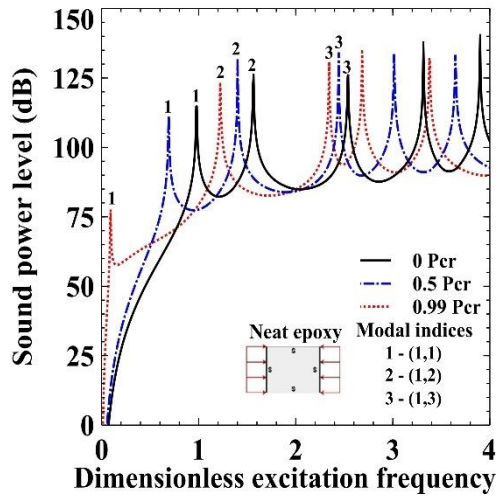
Load fractions like $0P_{cr}$, $0.5P_{cr}$ and $0.99P_{cr}$ are chosen to analyse the variation of the dimensionless average RMS velocity according to the nature and intensity of non-uniform edge loads. From Figure 5.4, it is noticed that dynamic response of the fundamental modes decreases with the increase in the intensity of the NUE load as a result of reduction in the structural stiffness. For FG-GRC plates whose $a/b=0.5$ mode shifting behaviour is not observed. However, a decrease in resonating peaks with the increase in the load intensity of respective NUE load is observed. But for $a/b=1.25$ case, one can clearly witness the shifting of first mode (1,1) to second mode (2,1) with increase in load intensity. For the $a/b=2$ and $\alpha=2$ case, the mode shifting happens from (1,1) to (3,1). By analysing the resonant amplitude one can realize that there is no specific trend with respect to increase in the load intensity for all the modes. However, it is anticipated that reduction in stiffness caused by increase in the intensity of the in-plane compressive load should increase the resonant amplitude. This behaviour in response is not observed due to the following reasons:

- (i) Due to the shifting of mode shapes, nodal and anti-nodal lines may come closer or move away from the excitation location.
- (ii) As the velocity is directly proportional to frequency, the reduction in frequency leads to reduction in the resonant amplitude.

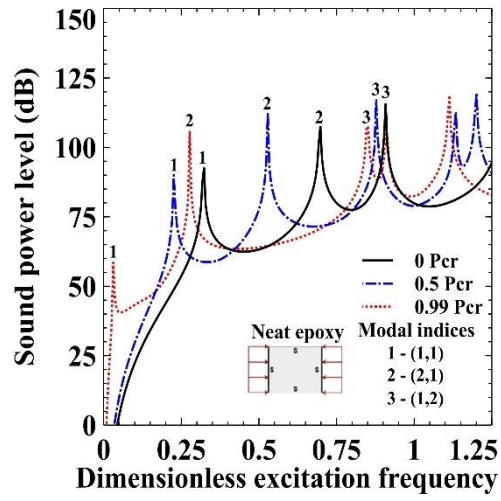
5.5. Sound radiation characteristics

In this section, the effect of nature of NUE load, aspect ratio, different dispersion patterns and weight fraction of the *GNPs* on acoustic response parameters such as sound power level, sound radiation efficiency and directivity pattern of the FG-GRC plate have been investigated. Acoustic response of the FG-GRC plate has been analysed under the same excitation condition used in the vibration analysis.

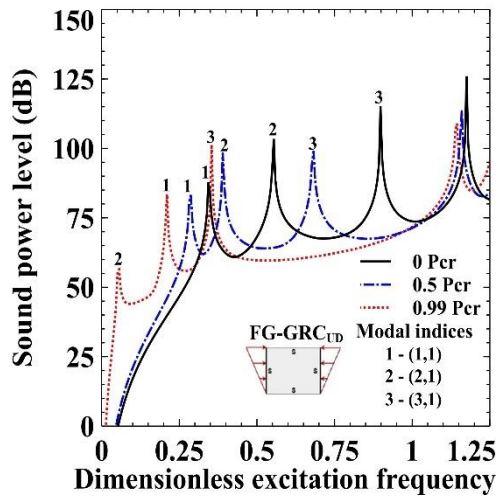
Sound power level radiated by the respective FG-GRC plates with different aspect ratios by the corresponding excitation frequency range for $\alpha=0$, $\alpha=1$, *sine* load and $\alpha=2$ cases are shown in Figure 5.5. It is observed that the peak associated with the fundamental vibration mode shifts towards the lower frequency side with increase in the magnitude of the applied edge load.



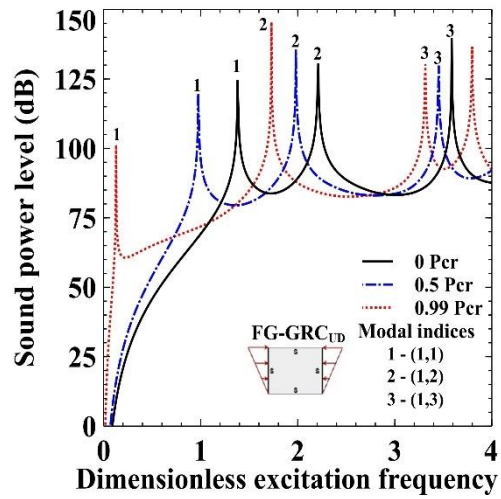
(a) Aspect ratio = 05, $W_{GNP} = 0\%$



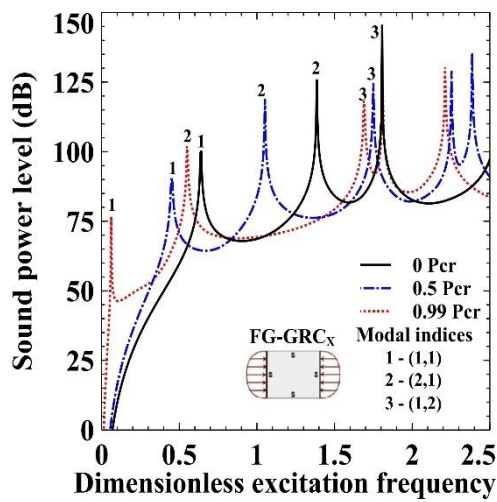
(b) Aspect ratio = 1.25, $W_{GNP} = 0\%$



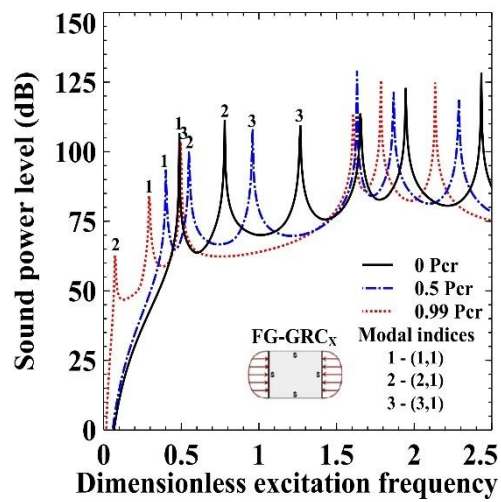
(c) Aspect ratio = 2, $W_{GNP} = 0.3\%$



(d) Aspect ratio = 0.5, $W_{GNP} = 0.3\%$



(e) Aspect ratio = 1.25, $W_{GNP} = 0.6\%$



(f) Aspect ratio = 2, $W_{GNP} = 0.6\%$

Continued...

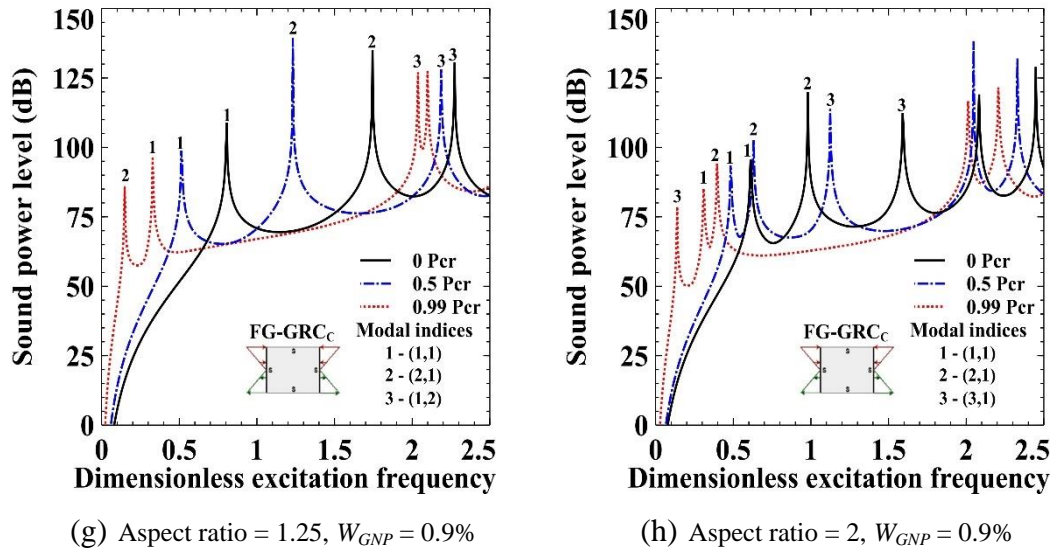


Figure 5.5: Effect of NUE loads on sound power level (dB).

By comparing with the forced vibration response plots, one can observe that the variation of sound power response follows the similar trend. However, very drastic reduction in sound power amplitude of the fundamental peak is observed when compared to the higher resonance frequency peaks. This is due the higher influence of NUE load on stiffness of FG-Graphene reinforced plate on the fundamental mode. Very low amplitude in fundamental peak for $0.99P_{cr}$ loading is also attributed to significant reduction in fundamental frequency at $0.99P_{cr}$ as the sound power is directly proportional to frequency also. Variation in resonant amplitude of sound power level with increase in load intensity of the in-plane load is similar for all the non-uniform load cases except for $\alpha=2$ case as seen in Figure 5.5.

It is also noticed that the fundamental frequency peak under the $0.5P_{cr}$ load reduces 5.23% and under $0.99P_{cr}$ load it reduces approximately 15 – 22.5% for all the aspect ratios. Figure 5.6 shows the effect of $GNPs$ dispersion pattern and weight percentage fraction on sound power level of the FG-Graphene reinforced plate. Figure 5.7 shows the sound radiation efficiency for the FG-GRC_X plate for $a/b=0.5$ and $\alpha=1.5$ case, which denotes that the intensity of in-plane loads doesn't have any significant effect on sound radiation efficiency. Similar trend in radiation efficiency with increase in in-plane load intensity is observed for other load cases also.

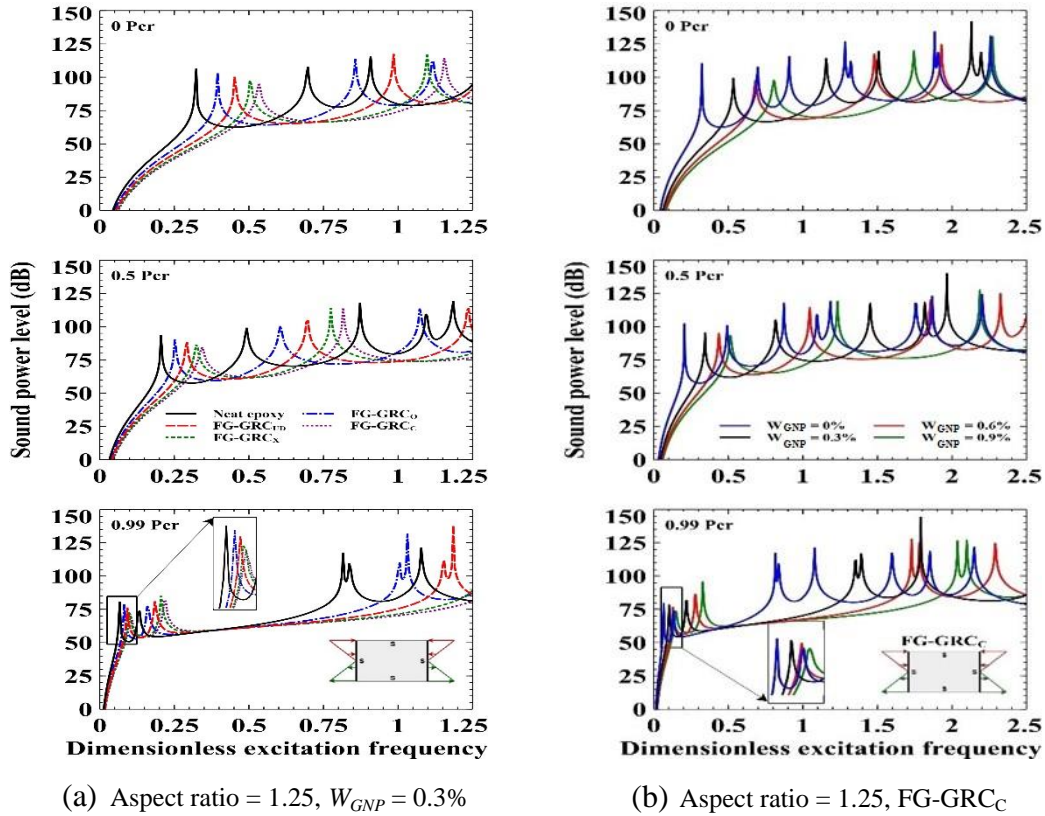


Figure 5.6: Effect of GNPs dispersion pattern and W_{GNP} on sound power level (dB).

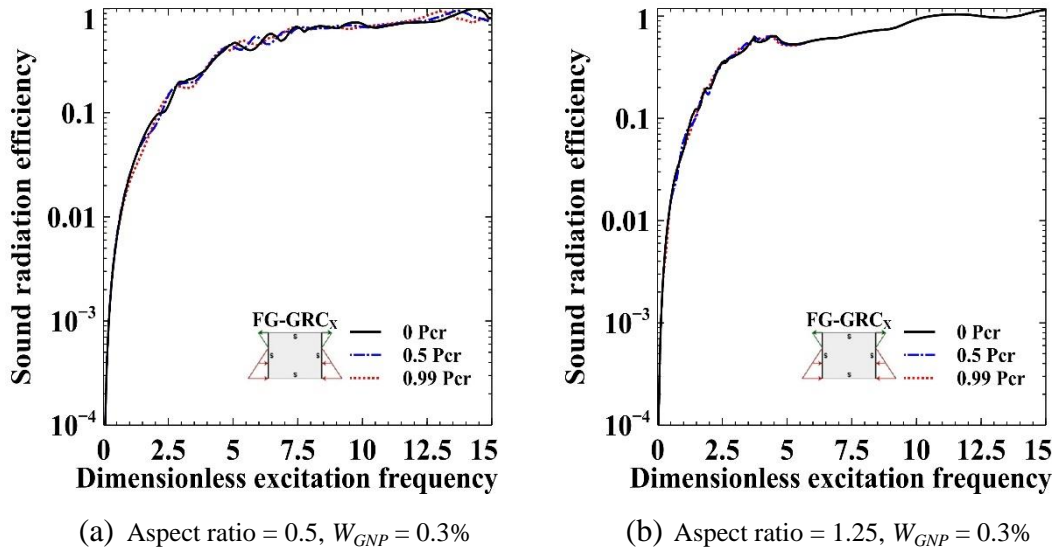


Figure 5.7: Effect of NUE load on sound radiation efficiency.

The effect of intensity of in-plane load on the sound power level in constant octave band is given in Figure 5.8, for $a/b=0.5$ and $\alpha=1.5$ case. Figure 5.8 clearly shows that increase of load fraction has a significant effect at lower frequencies when compared to mid and higher frequency bands. However, no distinctive trend in SWL

is observed in the higher frequency bandwidth. Effect of increase in load fraction values ($0P_{cr}$, $0.5P_{cr}$ and $0.99P_{cr}$) on overall sound power level (OSWL) associated with different non-uniform edge load cases is shown in Figure 5.9. It is noted that OSWL increases as the load fraction increases, it is around 6 dB for $0.5P_{cr}$ and around 16 dB for $0.99P_{cr}$ compared to no load condition.

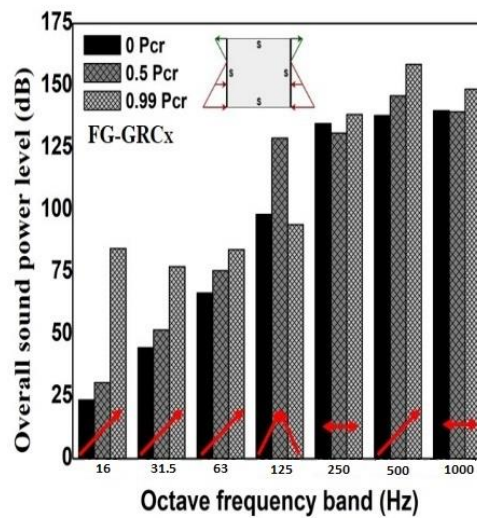


Figure 5.8: Effect of NUE loads on sound power level (dB) vs octave frequency band.

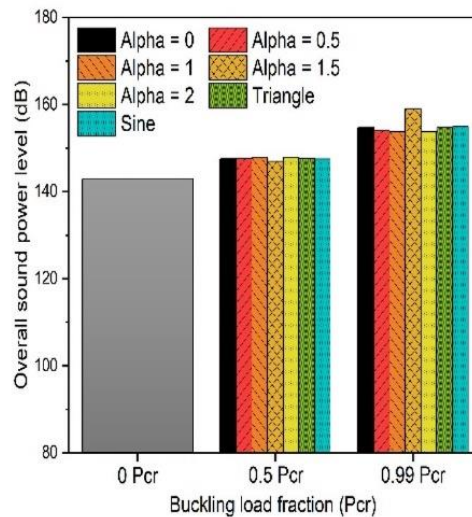


Figure 5.9: Effect of NUE loads on overall sound power level (dB).

The directivity pattern for FG-GRC plate is obtained at twice the radius distance of its maximum length above the centre of the plate for fundamental frequencies and is shown in Figure 5.10. A symmetry pattern is observed in the lower frequency, and the increase of load fraction and $W_{GNP}\%$ has significant effect by reducing the SPL distribution pattern level for all the cases. Figure 5.11 shows the contour plot representation on angle of sound radiation vs distance of the sound pressure level distribution pattern under NUE load. To understand the SPL distribution pattern the plate is excited with the fundamental frequency. A symmetry pressure level distribution pattern is observed for mode (1,1) and (3,1), whereas unsymmetrical SPL distribution pattern is observed for mode (2,1) (i.e., a shifted towards left side). In order to understand the influence of NUE loading on the directivity pattern, FG-GRC plate with $a/b=1.25$, $W_{GNP} = 0.6\%$, $\alpha=2$ case subjected to NUE load magnitude equal to $0.99P_{cr}$ is considered. The variation pattern of SPL distribution on both angle of sound radiation and distance of the FG-GRC_C plate has been represented in the adjacent 2D plot of the contour plot. Figure 5.12 shows the contour profile plot representational effect of NUE load on sound pressure level radiated for the better understanding of SPL distribution.

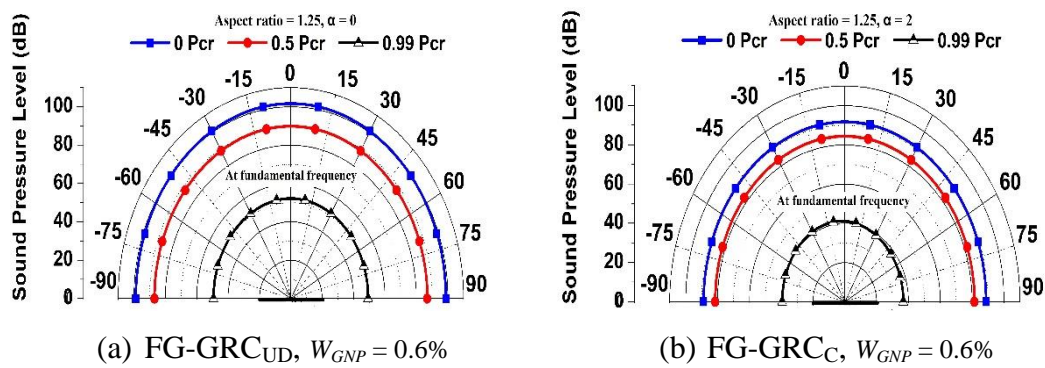
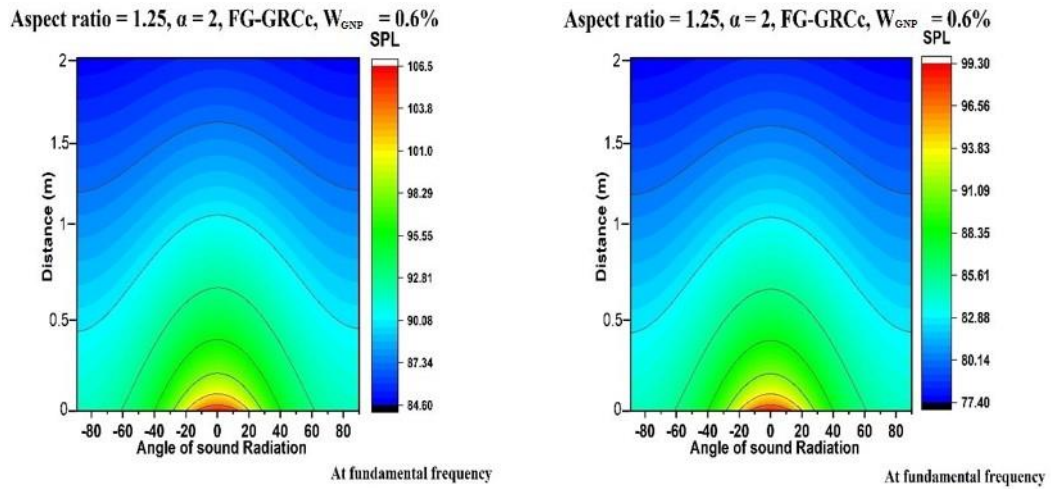
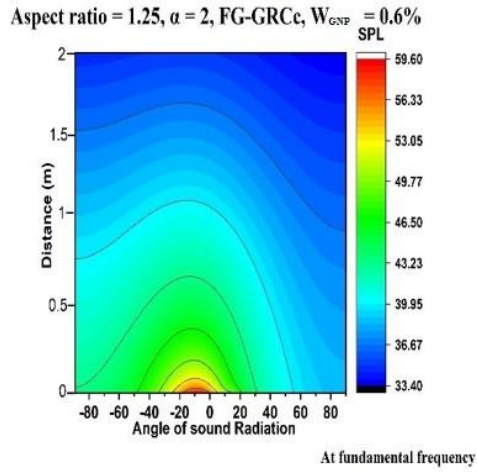


Figure 5.10: Effect of NUE loads on directivity pattern is obtained at a one-meter radius above the centre of the plate (z-axis).



(a) SPL distribution pattern at $0 P_{cr}$

(b) SPL distribution pattern at $0.5 P_{cr}$



(c) SPL distribution pattern at $0.99 P_{cr}$

Figure 5.11: Contour representational effect of NUE load on sound pressure level radiated.

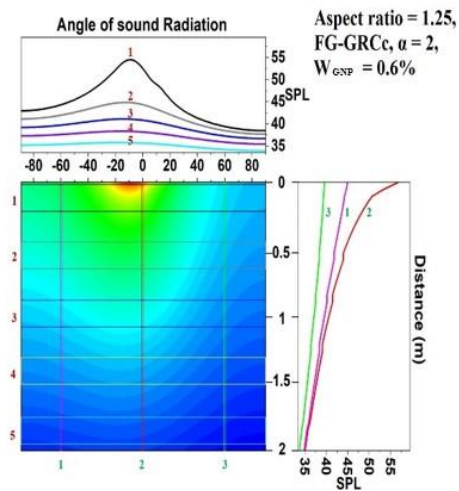
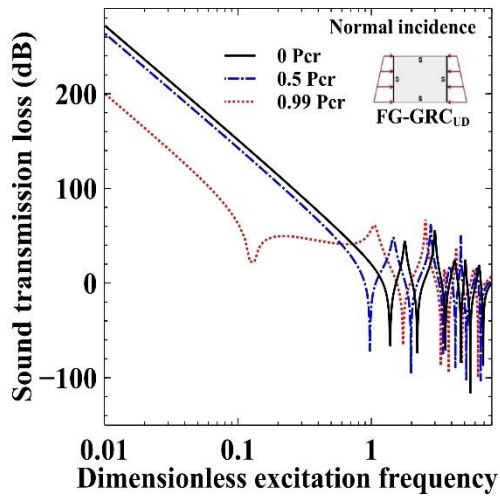


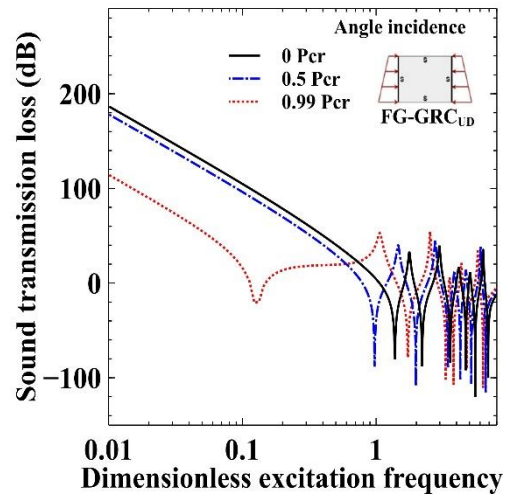
Figure 5.12: Contour profile representational effect of NUE load on sound pressure level radiated at $0.99 P_{cr}$

5.6. Sound transmission loss characteristics

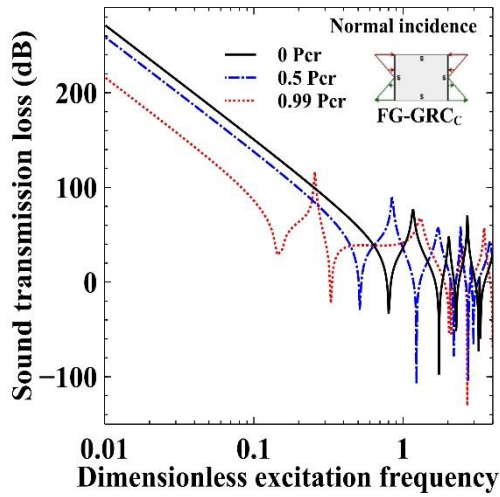
The FG-GRC plates subjected to a pressure wave having intensity of 1 N/m^2 under different NUE loads are analysed for the sound transmission loss characteristics. The influence of normal incident (i.e., $\theta=0^\circ$) and angle incident (i.e., $\theta=45^\circ$) on sound transmission loss of the FG-GRC plates is shown in Figure 5.13. The sound transmission loss plot can be divided into three main sections which is dependent on stiffness, damping and mass. The stiffness region signifies a bandwidth between zero to the first resonance peak, where it is observed that increase in non-uniform buckling load intensity has a significant reduction in the dB level. It is observed that around 15 dB reduction level in $0.5P_{cr}$ and 51 dB reduction in $0.99P_{cr}$ when compared to $0P_{cr}$. This is due to the stiffness softening effect cause by the NUE load intensity, as a result it causes an increase in velocity of the plate and decrease in resonance peak amplitude. Hence, it is revealed that increase in buckling load fraction tends to huge variation in frequencies peaks and reduction in the sound transmission loss level. The damping region signifies a narrow bandwidth of the resonance peak of the STL plot. This region represents the amount of damping which causes a negative STL region. However, the negative region signifies various inherent characteristics of the FG-GRC plate. It is observed that the fundamental resonance peak is suppressed when compared to the higher resonances peak due to the reinforcing effect of $GNPs$ present in FG-GRC plate. The region after the fundamental peak is sensitive of mass, since there is no specific change in the mass of FG-Graphene reinforced plate subjected to nonuniform compressive edge loads. It noticed that no significant change in the dB level. Figure 5.14 shows the effect of different dispersion grading and weight percentage of $GNPs$ on the FG-Graphene reinforced plates.



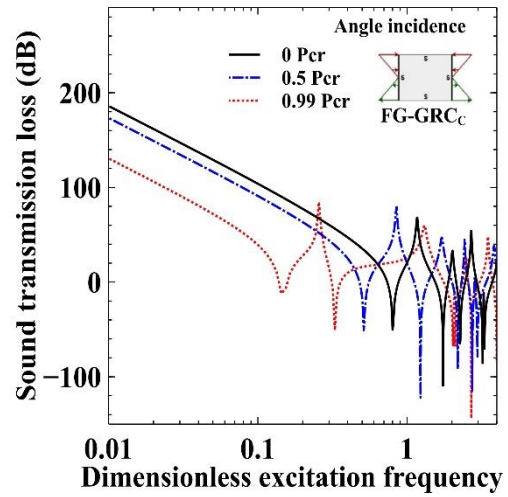
(a) Aspect ratio = 0.5, $W_{GNP} = 0.3\%$



(b) Aspect ratio = 2, $W_{GNP} = 0.3\%$

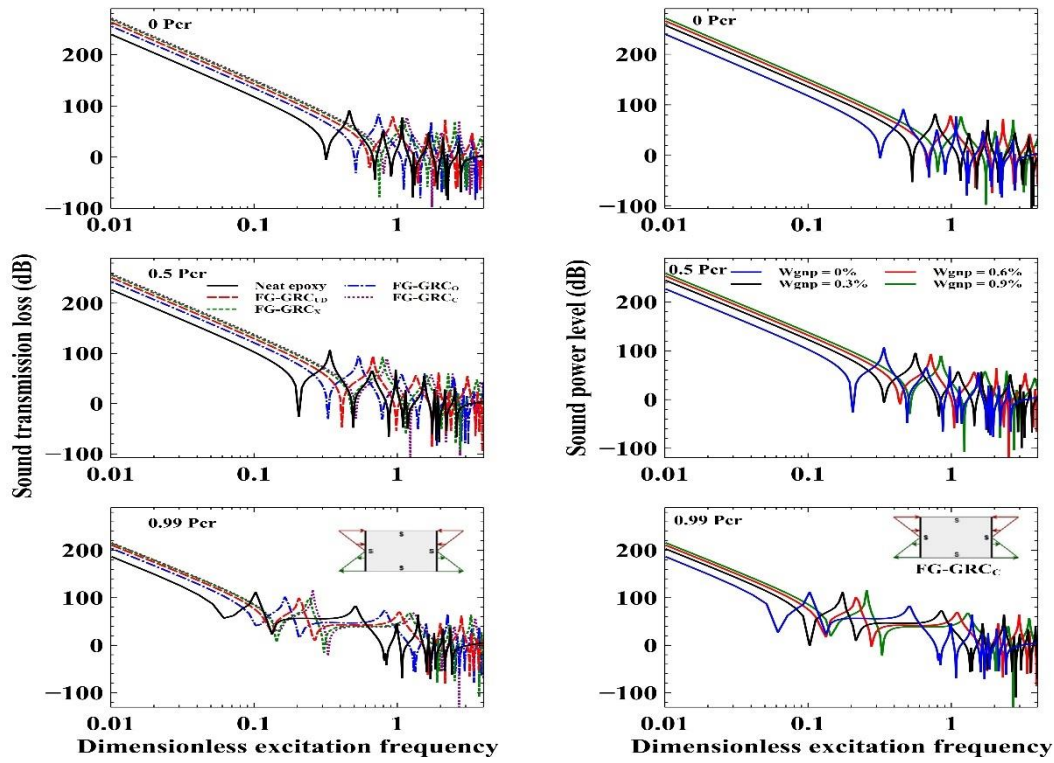


(c) Aspect ratio = 1.25, $W_{GNP} = 0.9\%$



(d) Aspect ratio = 2, $W_{GNP} = 0.9\%$

Figure 5.13: Effect of NUE loads on sound transmission loss for normal and angle incidence.



(a) Aspect ratio = 1.25, $W_{GNP} = 0.9\%$

(b) Aspect ratio = 1.25, $W_{GNP} = 0.9\%$

Figure 5.14: Effect of $GNPs$ dispersion pattern and W_{GNP} on sound transmission loss.

5.7. Closure

Vibro-acoustics physiognomies of simply supported FG-Graphene reinforced plate subjected to NUE loads are analytically investigated. Impact of numerous crucial elements like nature of NUE load, weight fraction (W_{GNP}) and nature of grading of $GNPs$, aspect ratio (a/b) and slenderness ratio (b/h) on buckling and vibro-acoustic behaviour of FG-Graphene plate are investigated. Primarily based on a detailed analytical investigation, $\alpha=2$ load case resulted in the higher critical buckling load (P_{cr}) compared to the other load cases, because of the structural stability improved through the equally combined effect of tensile and compressive forces. For a/b is 0.5 the FG-GRC plate buckles at (1,1) mode for all the load cases. Whereas for $a/b=1.25$ the plate buckles at (1,1) mode for all cases, except for $\alpha=2$ case for which it buckles at (2,1) mode. Hence higher the length of FG-GRC plate in the loading direction (i.e., aspect ratio is 2), mode with higher modal indices (3,1) is observed for the $\alpha=2$ case and the other NUE load cases has (2,1) buckling mode. It is noted that $GNPs$ grading pattern and minute increase in W_{GNP} of $GNPs$ as a significant rate of increase in the

stiffness parameter, which leads to increase in buckling strength and natural frequencies of FG-Graphene reinforced plate. In sound radiation characteristics, the influences of NUE load have significant reduction of sound power level of approximately 30 dB at $0.99P_{cr}$ of fundamental peak when compared to the no-load condition, and slight decrease in the amplitude of fundamental frequency peak for the $0.5P_{cr}$ due to the stiffness interference of the structure. In sound radiation efficiency, no significant variation has been observed concerning the type of NUE load. However, the overall sound power level increases with load intensity in the lower frequency bands. In the STL response, change in dB level is clearly observed only in the stiffness region compared to the damping and mass regions. Significant reduction in structural stiffness with increase in the intensity of non-uniform edge load is the reason for this behaviour. It is observed that the FG-GRC_C grading shows the greater buckling and vibro-acoustic behaviour, because of improved bending stiffness related to *GNPs* orientations.

CHAPTER 6

6. VIBRO-ACOUSTIC STUDIES OF POROUS FG-GRC PANEL UNDER NON-UNIFORM UNIAXIAL EDGE LOADS

6.1. Introduction

A rectangular porous FG-GRC plate whose material properties for the metal matrix and graphene reinforcement are given in Table 2.2, with the dimensions of 0.5 x 0.4 x 0.004 m³ with simply supported condition is considered. By considering real-time manufacturing issues and effective analytical material modelling, it is presumed that porous FG-GRC plate is reinforced with 12 layers of GNP. The synergetic effect of NUE loads, GNP grading patterns, GNP weight percentage, porosity distribution, and porosity coefficients on vibro-acoustics characteristics of porous FG-GRC is discussed in this section. However, to determine vibro-acoustic response of porous FG-GRC plates under the different NUE loading conditions, buckling load ratio (BLR) for the various load cases are calculated first and shown in Table 6.1. Porous FG-GRC plate is presumed to be excited under the influence of NUE loads in an air medium with the constant damping factor (0.01). By performing the convergence study, 0.5 Hz frequency resolution is selected, and considering the “six elements per wavelength” condition 20 x 20 mesh division is followed throughout the vibro-acoustic characterization of the porous FG-GRC plates. Dimensionless buckling load, natural frequency, and average RMS velocity used for the current investigation are defined as

$$\bar{P}_{cr} = P_{cr}^x \left(\frac{b^2}{E_m \pi^2} \right) \times 10^8 \quad (6.1)$$

$$\bar{\omega}_{mn} = \omega_{mn} \sqrt{\frac{\rho_m}{E_m}} \left(\frac{b^2}{\pi^2} \right) \times 10^3 \quad (6.2)$$

$$\bar{V}_{rms} = V_{rms} \left(\frac{E_m h^3}{b^4 F_o} \right) \times 10^{-6} \quad (6.3)$$

Table 6.1: Buckling load ratio of porous FG-GRC under NUE loads.

Aspect ratio (a/b)	Types of NUE loads						
	0	0.5	1	1.5	2	Triangle	Sine
1.25	1 ¹	0.7515 ¹	0.5091 ¹	0.2858 ¹	0.2059 ²	0.5002 ¹	0.8485 ¹

The mode number (m) of respective buckling case is denoted by the superscript number.

6.2. Buckling response

The combined effects of NUE loads, graphene reinforcement ($GNPs$) grading, weight percentage (W_{GNP}), and porosity distribution under the constant porosity coefficients (i.e., VPC-0.4, VPS-0.6708, and UP-0.7404) on dimensionless buckling load of different porous FG-GRC plates are presented in Table 6.2. A third-order approximation is used to the respective strain energy governing equation to obtain the buckling load and buckling load fraction (BLR). The load intensity of different NUE load configuration has a huge impact on the dimensionless buckling load. The buckling strength of the porous FG-GRC plate increases with the load factor (α) as a consequence of non-uniformity and increase in tensile force intensity in the applied load. Because of this reason, the buckling strength of porous FG-GRC plates under NUE loads is much higher than that of the uniform load case. The highest buckling value of porous FG-GRC plate stands for $\alpha=2$ case when compared to other load cases. This is due to as half of the plate edge is subjected to the tensile load which improves the buckling strength and stability. Buckling strength for *triangle* load is very close to $\alpha=1$ case, due to the nearby load intensity of both load cases.

Table 6.2 also shows that the $GNPs$ grading and weight percentage have a significant effect on buckling load of the porous FG-GRC plates. Buckling load value of porous FG-GRC plate increases with nature of $GNPs$ grading pattern in the following ascending order of the patterns O, UD, X, and C. Owing to its unique arrangement and distribution of respective grading pattern variation. It is observed that 8.7, 16.5, 24.5, and 29.2% increase in buckling strength of porous FG-GRC O, UD, X, and C plates respectively ($W_{GNP}=0.3\%$) when compared to the pure metal. Likewise, around 95% increase in buckling load value of porous FG-GRC plate for 0.6% of W_{GNP} compared to 0.3% of W_{GNP} is noticed. However, in case of nature of porous distribution, reduction of stiffness of the porous FG-GRC plate has been observed as seen in Table 6.2. Compared to the non-porous FG-GRC case 14.6, 26

Table 6.2: Dimensionless buckling load of porous FG-GRC under NUE loads.

W_{GNP}	Grading pattern	Alpha (α)					Triangle	Sine
		0	0.5	1	1.5	2		
0%	Matrix ^{NP}	2.53 ¹	3.37 ¹	4.98 ¹	8.88 ¹	14.52 ²	5.07 ¹	2.99 ¹
	Matrix ^{UP}	1.87 ¹	2.50 ¹	3.69 ¹	6.57 ¹	10.75 ²	3.75 ¹	2.21 ¹
	Matrix ^{VPC}	2.16 ¹	2.87 ¹	4.24 ¹	7.56 ¹	12.37 ²	4.32 ¹	2.54 ¹
	Matrix ^{VPS}	1.43 ¹	1.91 ¹	2.82 ¹	5.02 ¹	8.22 ²	2.87 ¹	1.69 ¹
0.3%	FG – GRC ^{NP} _{UD}	2.95 ¹	3.93 ¹	5.80 ¹	10.34 ¹	16.91 ²	5.90 ¹	3.48 ¹
	FG – GRC ^{UP} _{UD}	2.18 ¹	2.91 ¹	4.29 ¹	7.65 ¹	12.52 ²	4.37 ¹	2.57 ¹
	FG – GRC ^{VPC} _{UD}	2.51 ¹	3.34 ¹	4.94 ¹	8.80 ¹	14.40 ²	5.03 ¹	2.96 ¹
	FG – GRC ^{VPS} _{UD}	1.67 ¹	2.22 ¹	3.28 ¹	5.85 ¹	9.56 ²	3.34 ¹	1.97 ¹
	FG – GRC ^{NP} _X	3.15 ¹	4.20 ¹	6.20 ¹	11.04 ¹	18.06 ²	6.31 ¹	3.72 ¹
	FG – GRC ^{UP} _X	2.33 ¹	3.11 ¹	4.59 ¹	8.17 ¹	13.37 ²	4.67 ¹	2.75 ¹
	FG – GRC ^{VPC} _X	2.70 ¹	3.59 ¹	5.31 ¹	9.46 ¹	15.47 ²	5.40 ¹	3.18 ¹
	FG – GRC ^{VPS} _X	1.76 ¹	2.34 ¹	3.46 ¹	6.16 ¹	10.08 ²	3.52 ¹	2.07 ¹
	FG – GRC ^{NP} _O	2.75 ¹	3.66 ¹	5.40 ¹	9.63 ¹	15.75 ²	5.50 ¹	3.24 ¹
	FG – GRC ^{UP} _O	2.03 ¹	2.71 ¹	4.00 ¹	7.13 ¹	11.66 ²	4.07 ¹	2.40 ¹
	FG – GRC ^{VPC} _O	2.32 ¹	3.09 ¹	4.57 ¹	8.14 ¹	13.32 ²	4.65 ¹	2.74 ¹
	FG – GRC ^{VPS} _O	1.58 ¹	2.10 ¹	3.10 ¹	5.53 ¹	9.05 ²	3.16 ¹	1.86 ¹
0.6%	FG – GRC ^{NP} _C	3.27 ¹	4.35 ¹	6.42 ¹	11.44 ¹	18.72 ²	6.54 ¹	3.85 ¹
	FG – GRC ^{UP} _C	2.42 ¹	3.22 ¹	4.75 ¹	8.47 ¹	13.86 ²	4.84 ¹	2.85 ¹
	FG – GRC ^{VPC} _C	2.81 ¹	3.74 ¹	5.53 ¹	9.85 ¹	16.12 ²	5.63 ¹	3.32 ¹
	FG – GRC ^{VPS} _C	1.80 ¹	2.39 ¹	3.54 ¹	6.30 ¹	10.31 ²	3.60 ¹	2.12 ¹
	FG – GRC ^{NP} _{UD}	3.35 ¹	4.46 ¹	6.58 ¹	11.72 ¹	19.18 ²	6.70 ¹	3.95 ¹
	FG – GRC ^{UP} _{UD}	2.48 ¹	3.30 ¹	4.87 ¹	8.68 ¹	14.20 ²	4.96 ¹	2.92 ¹
	FG – GRC ^{VPC} _{UD}	2.85 ¹	3.79 ¹	5.60 ¹	9.98 ¹	16.33 ²	5.70 ¹	3.36 ¹
	FG – GRC ^{VPS} _{UD}	1.89 ¹	2.52 ¹	3.72 ¹	6.63 ¹	10.85 ²	3.79 ¹	2.23 ¹
	FG – GRC ^{NP} _X	3.74 ¹	4.98 ¹	7.35 ¹	13.09 ¹	21.42 ²	7.48 ¹	4.41 ¹
	FG – GRC ^{UP} _X	2.77 ¹	3.68 ¹	5.44 ¹	9.69 ¹	15.86 ²	5.54 ¹	3.26 ¹
	FG – GRC ^{VPC} _X	3.21 ¹	4.28 ¹	6.32 ¹	11.26 ¹	18.41 ²	6.43 ¹	3.79 ¹
	FG – GRC ^{VPS} _X	2.07 ¹	2.75 ¹	4.06 ¹	7.24 ¹	11.84 ²	4.13 ¹	2.43 ¹
FG – GRC ^{NP} _O	2.95 ¹	3.93 ¹	5.80 ¹	10.34 ¹	16.92 ²	5.91 ¹	3.48 ¹	
FG – GRC ^{UP} _O	2.18 ¹	2.91 ¹	4.30 ¹	7.66 ¹	12.52 ²	4.37 ¹	2.58 ¹	
FG – GRC ^{VPC} _O	2.48 ¹	3.31 ¹	4.88 ¹	8.70 ¹	14.23 ²	4.97 ¹	2.93 ¹	
FG – GRC ^{VPS} _O	1.72 ¹	2.29 ¹	3.38 ¹	6.02 ¹	9.85 ²	3.44 ¹	2.02 ¹	
FG – GRC ^{NP} _C	3.96 ¹	5.27 ¹	7.79 ¹	13.87 ¹	22.69 ²	7.93 ¹	4.67 ¹	
FG – GRC ^{UP} _C	2.93 ¹	3.90 ¹	5.76 ¹	10.27 ¹	16.80 ²	5.87 ¹	3.46 ¹	
FG – GRC ^{VPC} _C	3.43 ¹	4.57 ¹	6.75 ¹	12.02 ¹	19.66 ²	6.87 ¹	4.05 ¹	
FG – GRC ^{VPS} _C	2.14 ¹	2.85 ¹	4.22 ¹	7.51 ¹	12.29 ²	4.29 ¹	2.53 ¹	

The mode number(m) of respective buckling case is denoted by the superscript number.

and 43.4% reduction in buckling strength is observed for VPC, UP and VPS porosity cases respectively.

The same amount of reduction is observed for different kinds of grading patterns and weight fraction of $GNPs$ and different types of NUE loads also. This is due to the material removal effect caused by inclusion of porosity in the FG-GRC plate. Figure 6.1 illustrates the effects of porosity coefficients on different porous FG-GRC plates and signifies that a increase in porosity coefficients reduces the stiffness

of plate hence buckling strength of the plate. Reduction in buckling strength with respect to porosity grading is observed in the order of $VPC > UP > VPS$ as seen in Table 6.2 and Figure 6.1. The values given in Table 6.1 helps to obtain the dynamic response of porous FG-GRC plate based on Reddy's TSDT as mentioned in methodology. From the above-detailed buckling investigation, the FG-GRC_C grading pattern achieves the superior buckling strength when compared to the rest of the grading patterns. So, to investigate the effects NUE loads, porosity distribution, and porosity coefficients on the dynamic characteristics of porous FG-GRC plate, FG-GRC_C grading pattern is considered.

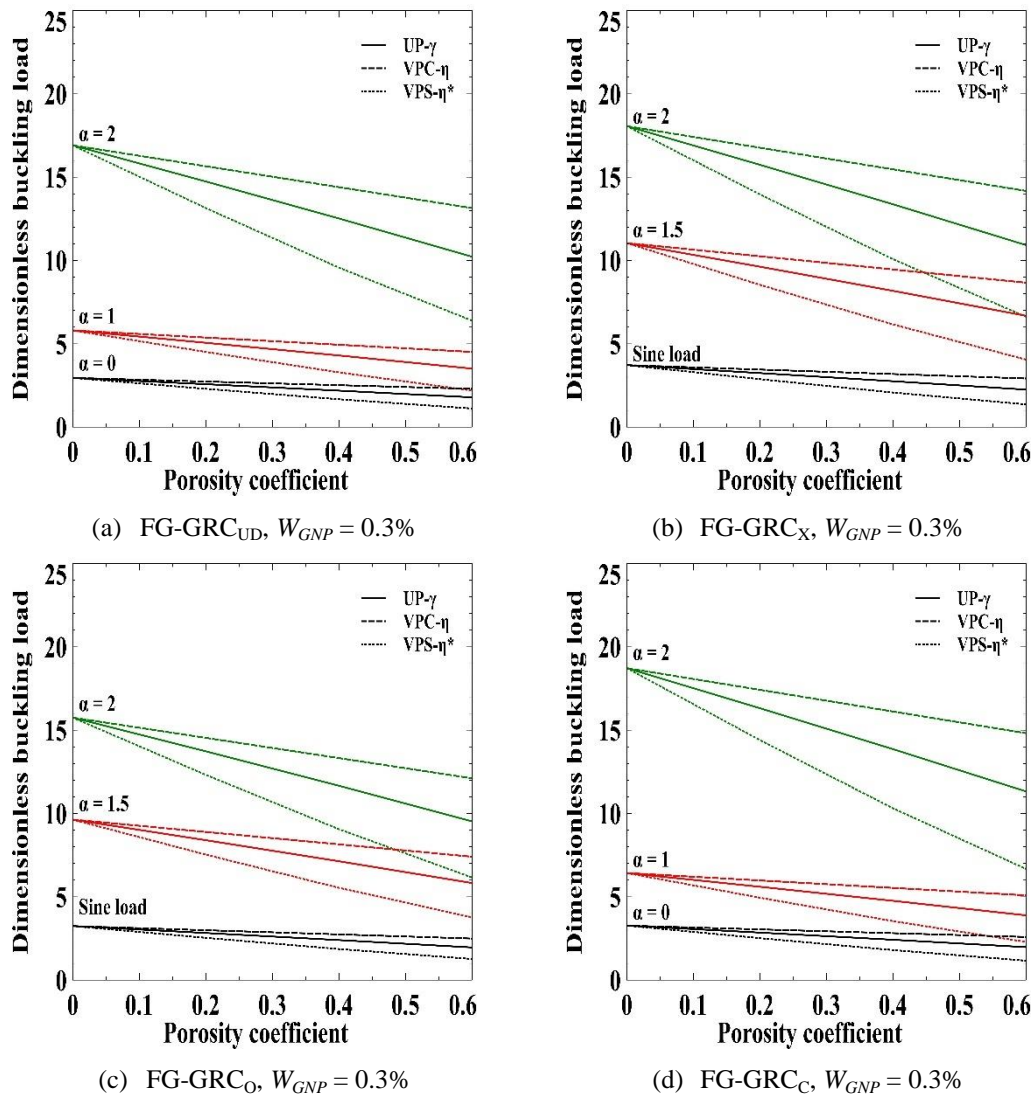


Figure 6.1: Effect of porosity coefficients (γ , η and η^*) on dimensional buckling load.

6.3. Vibration response

6.3.1. Free vibration characteristics

The impacts of *GNPs* grading/weight percentage, porosity dispersion pattern and coefficients on change in natural frequency of porous FG-GRC plates under the NUE loads are shown in Figure 6.2 and Figure 6.3. It is observed that the porous FG-GRC plate frequency reduces to zero when the applied compressive load matches the corresponding buckling load. Similarly, the modal indices of free vibration mode at critical buckling value are same as that of fundamental buckling mode for the particular NUE load. The effect of *GNPs* grading pattern and weight percentage on the dimensionless natural frequency is illustrated in Figure 6.2. It shows that the dispersion pattern has a noteworthy change on natural frequency, and variation of fundamental natural frequency from higher to least is in order of porous FG-GRC C, X, UD, and O with percentage of 16, 13.9, 10.3, and 6.4% increase for W_{GNP} is 0.3%, when compared to pure metal. Likewise, around 30% increase in fundamental frequency for 0.6% of W_{GNP} compared to 0.3% of W_{GNP} is observed. Porous FG-GRC_C grading shows the superior stiffness compared to other grading patterns, due to more amount of *GNPs* distribution towards the outer surface compared to the neutral axis of the porous FG-GRC plate. Whereas the porous FG-GRC_O grading pattern achieves the least stiffness, due to lesser amount of *GNPs* at the outer surfaces and higher amount of *GNPs* at the inner surfaces.

Variations of dimensionless natural frequency under the different types of NUE loads is shown in Figure 6.2(c). For all NUE load cases it is seen that the porous FG-GRC plate buckles at (1,1), but for $\alpha=2$ case the plate buckles at (2,1) mode due to the combined effect of tensile and compressive loads. The effect of porosity distribution can be seen in Figure 6.2(d).

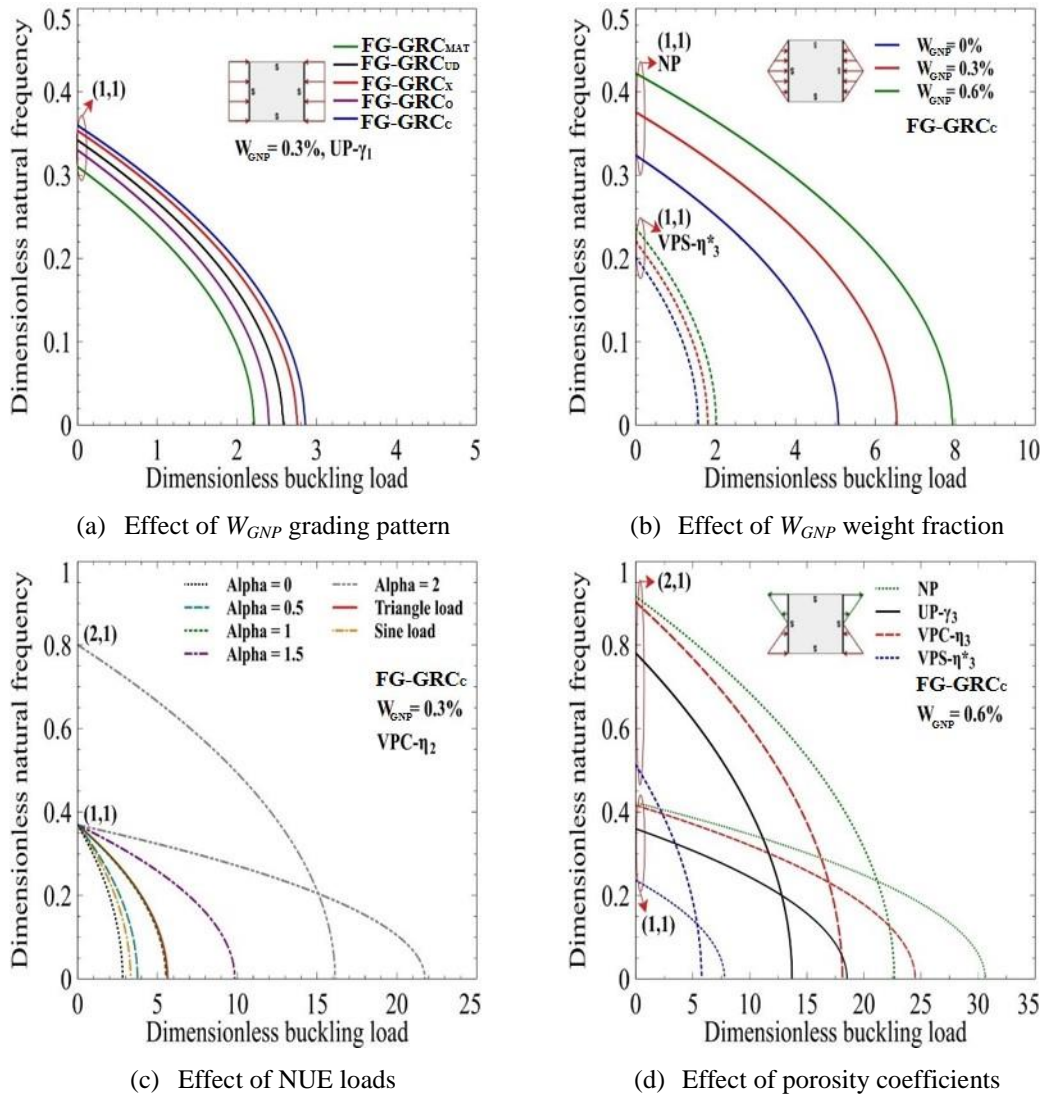


Figure 6.2: Parametric effect on dimensionless load natural frequency.

A similar order of reduction in stiffness of porous FG-GRC plate (i.e., $VPC > UP > VPS$) can be seen, as already discussed in the buckling studies related to the nonporous FG-GRC. The dimensionless natural frequency reduces according to the nature of porosity pattern 1.5% - VPC, 14.7% - UP, and 44.03% - VPS. VPC porosity distribution results in less reduction in natural frequencies compared to UP and VPS. This indicates that the nature of the porosity distribution pattern influences the bending stiffness of plate significantly. As a result of more amount of porosity at the centre, there is not much reduction in overall stiffness for the VPC case. Similarly, due to less amount of porosity at the centre, the structural stiffness reduces significantly for VPS case. The impact of porosity coefficients on fundamental

frequency of porous FG-GRC for different buckling load fractions ($0P_{cr}$, $0.5P_{cr}$, and $0.975P_{cr}$) is shown in Figure 6.3. The increase in porosity coefficients and buckling load fraction roots a drop in natural frequency. Figure 6.4 shows the impact of NUE loads on free vibration mode shapes of the porous FG-GRC, and a detailed explanation about mode shifting behaviour for the corresponding NUE loads is presented in the section of sound radiation response of porous FG-GRC plate.

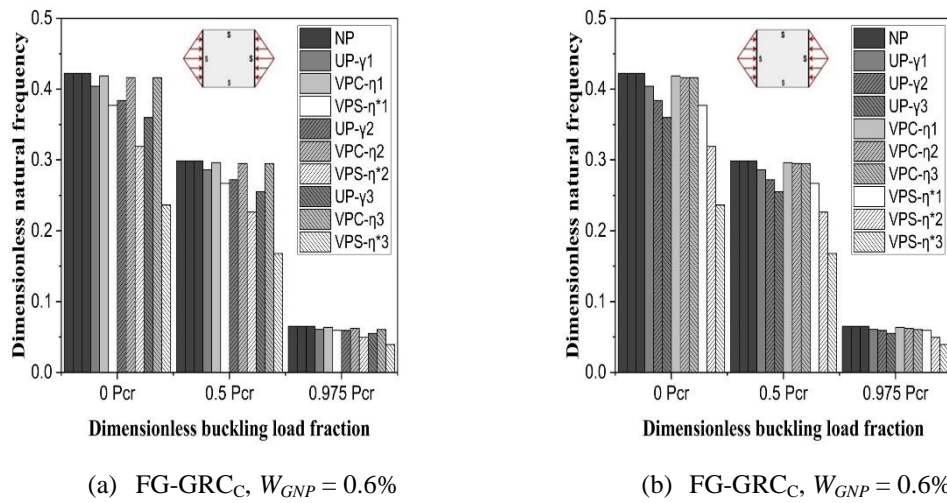


Figure 6.3: Variation of dimensionless fundamental frequency of porous FG-GRC plate under different porosity coefficients.

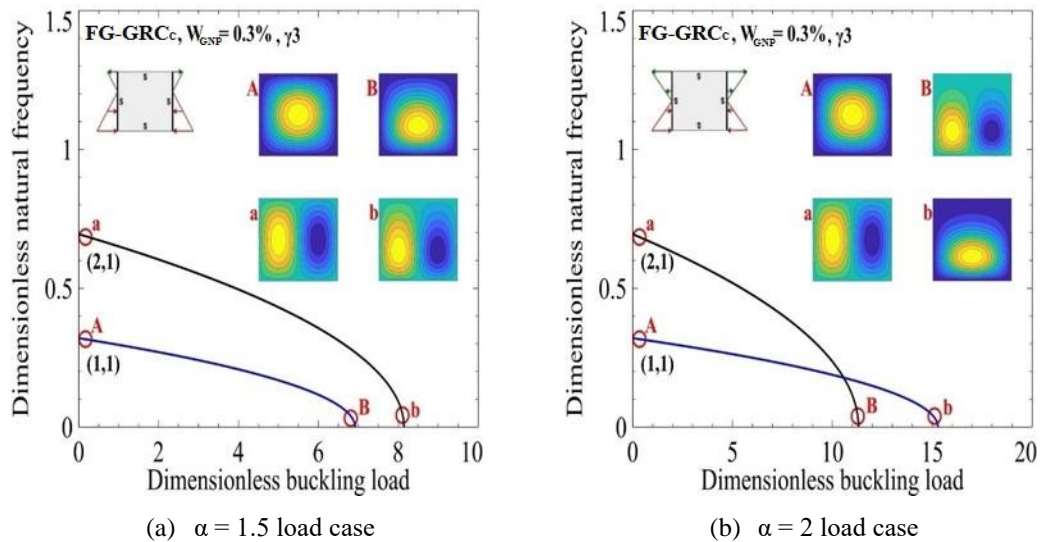
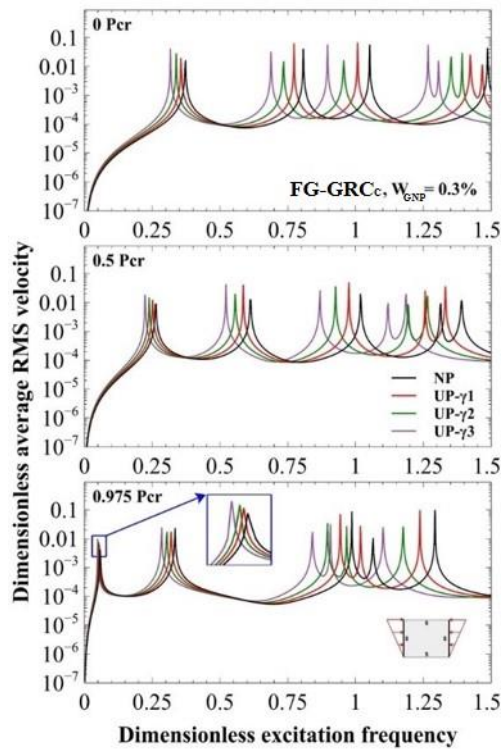


Figure 6.4: Effect of NUE loads on the free vibration mode shapes.

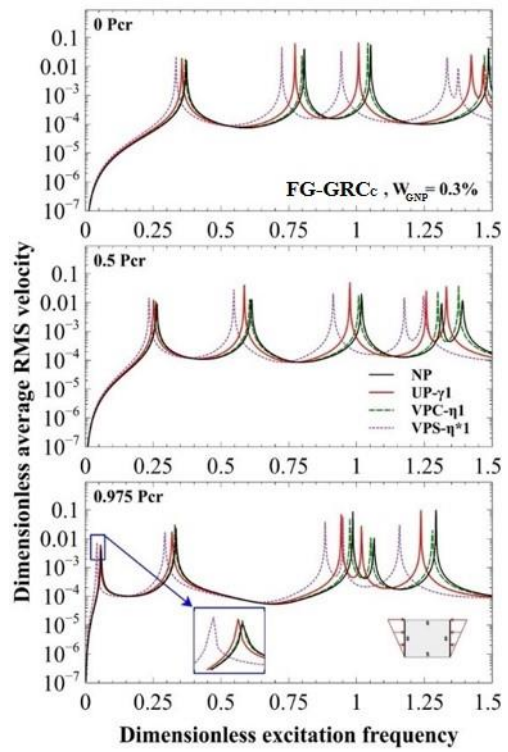
6.3.2. Forced vibration characteristics

Forced vibration response of porous FG-GRC plate under steady-state mechanical excitation, under the influence of grading of porosity, porosity coefficients, and nature of NUE load are presented in this section. For this, a time-dependent sinusoidal force with a magnitude of 1 N with frequency resolution of 0.5 Hz and an excitation frequency range of 0 to 2000 Hz is selected. The concentrated point load is applied along the normal direction to the plate surface at $(a/4, b/4)$ from the origin, to excite the porous FG-GRC plate. Based on the consideration of acoustic coincidence frequency of the porous FG-GRC plate should lie within the range of excitation frequency the upper limit 2000 Hz is chosen for all the further investigation. Buckling load fractions like $0P_{cr}$, $0.5P_{cr}$ and $0.975P_{cr}$ are chosen to analyse the change of dimensionless average RMS velocity of porous FG-GRC subjected to different types of NUE loads.

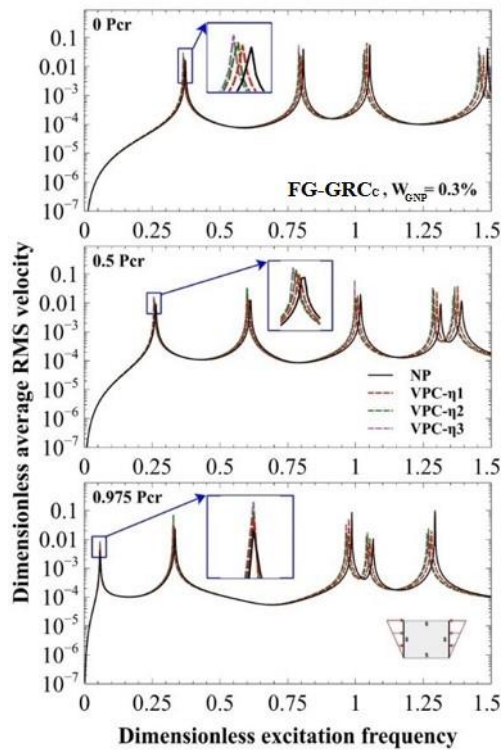
The dynamic response of fundamental mode of porous FG-GRC plates decreases, with the increase in the intensity of the NUE load as a result of a reduction in stiffness as seen in Figure 6.5. By analysing the resonant amplitude one can realize there is no specific trend with respect to an increase in the load intensity for all modes. It is anticipated that a reduction in stiffness will lead to an increase in resonant amplitude. However, this anticipated trend is not observed in the forced vibration response of the other modes. There is no specific trend in the vibration response due to the movement of nodal and anti-nodal lines towards/away from excitation location. However, in the case of porosity distribution and its coefficient effect, it is evident that a increase in porous nature reduces the stiffness of the porous FG-GRC plate in turn causes a increase in the resonant amplitude of average RMS velocity as seen from Figure 6.5. It is also clear that there is a shift in natural frequency peaks towards the lower value as the porosity coefficient increase for the different porosity distributions (i.e., VPC, VPS, and UP). This shifting of natural frequency is significant for VPS type porosity distribution (Figure 6.5(e)), mild for the UP distribution (Figure 6.5(a)), and very least for VPC distribution (Figure 6.5(c)).



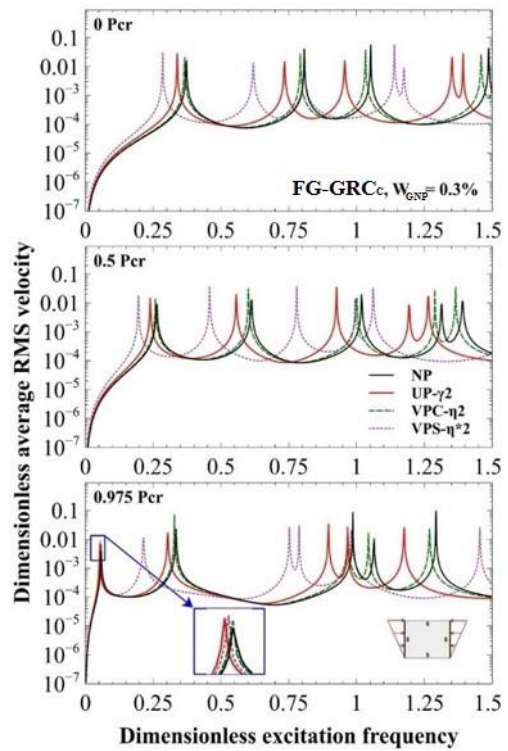
(a) Effect of porosity coefficient
(UP- γ_1 , UP- γ_2 & UP- γ_3)



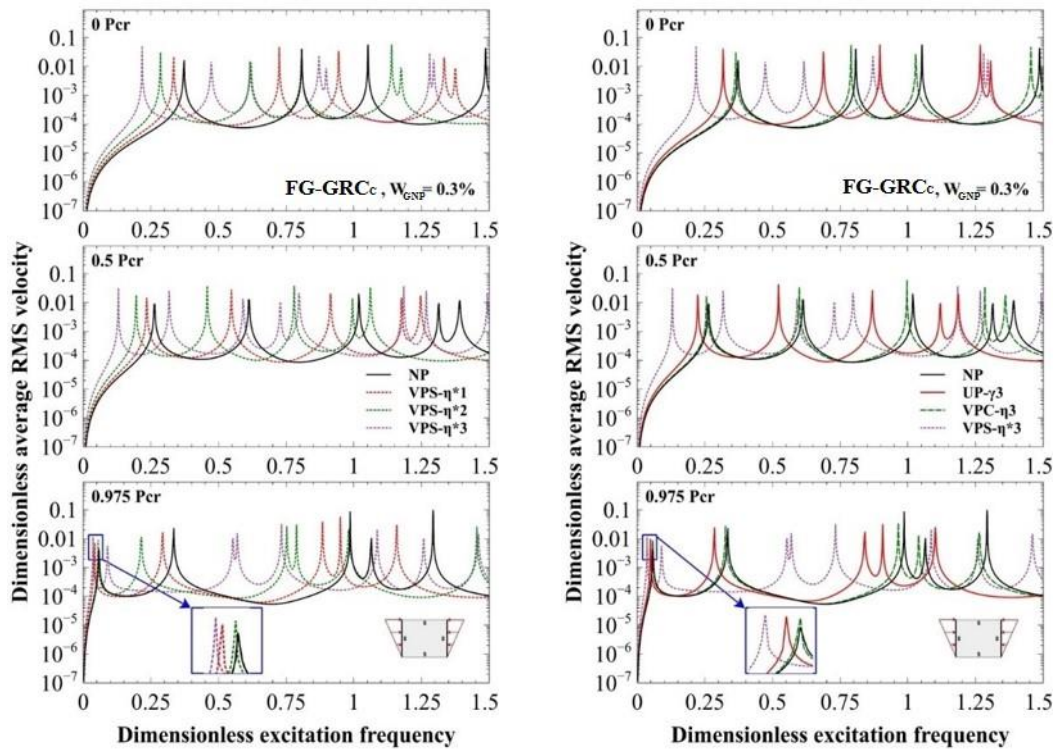
(a) Effect of porosity coefficient
(UP- γ_1 , VPC- η_1 & VPC- η^*1)



(c) Effect of porosity coefficient
(VPC- η_1 , VPC- η_2 & VPC- η_3)



(d) Effect of porosity coefficient
(UP- γ_2 , VPC- η_2 & VPC- η^*2)



(e) Effect of porosity coefficient
(VPC- η^*1 , VPC- η^*2 & VPC- η^*3)

(f) Effect of porosity coefficient
(UP- γ_3 , VPC- η_3 & VPC- η^*3)

Figure 6.5: Forced vibration response of porous FG-GRC plate under different porosity coefficients.

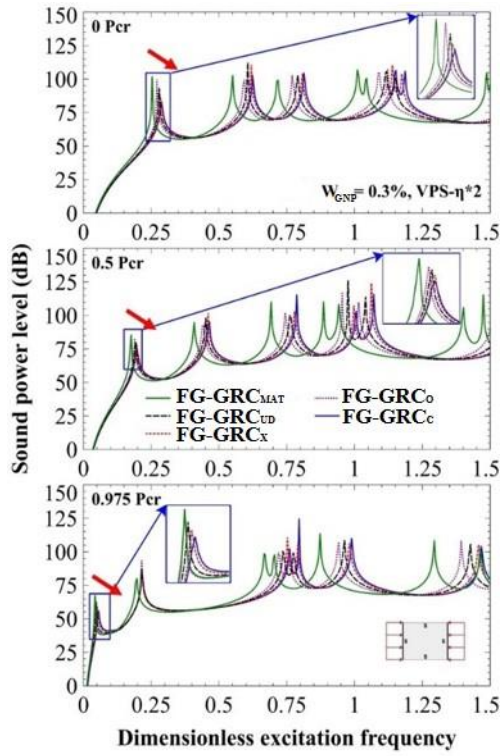
Similarly, the resonant amplitude is also pretentious significantly according to the porosity distributions and porosity coefficients. Trend with a increase in the fundamental peak amplitude, with increase in porosity has been observed due to the variation in stiffness of the respective porous FG-GRC plate caused by porosity distributions.

The variation of porosity pattern influences the structural stiffness significantly as discussed earlier and the effect can be clearly observed with an increase in porosity coefficient. However, UP case has no variation in porosity distribution, a increase in porosity coefficients causes a reduction in stiffness and results in midrange value of cross-sectional inertia between VPC and VPS porosity distributions. Due to this combined effect of grading pattern and coefficient of porosity for UP and VPS cases decrease in stiffness of porous FG-GRC plate is more compared to the VPC case in which the stiffness of the plate increases with an intensification in porosity coefficients. In general conclusion, it is noted for all

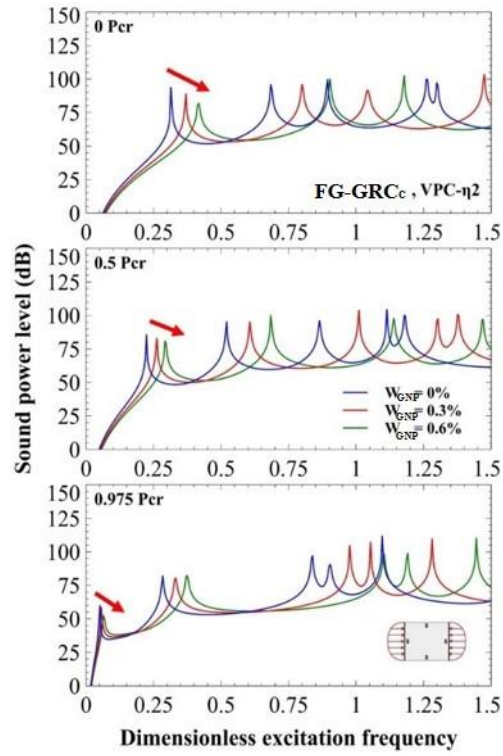
porosity distributions (i.e., VPC, UP, and VPS) the resonant amplitude is higher for the higher porosity coefficients value, due to less stiffness of porous FG-GRC plate for higher porosity coefficients. A similar, effect of variation in resonance amplitude of vibration response is observed from Figure 6.5 (b), (d), and (f) when different porosity distribution is compared. Resonant amplitude for non-porous FG-GRC plate is always lesser compared to different porosity distribution and coefficients, due to the greater value of cross-section inertia which increases flexural/bending stiffness of porous FG-GRC plate. A detailed explanation about variation in resonance peak amplitude for the corresponding NUE loads is presented in the section of acoustic response of porous FG-GRC.

6.4.Sound radiation characteristics

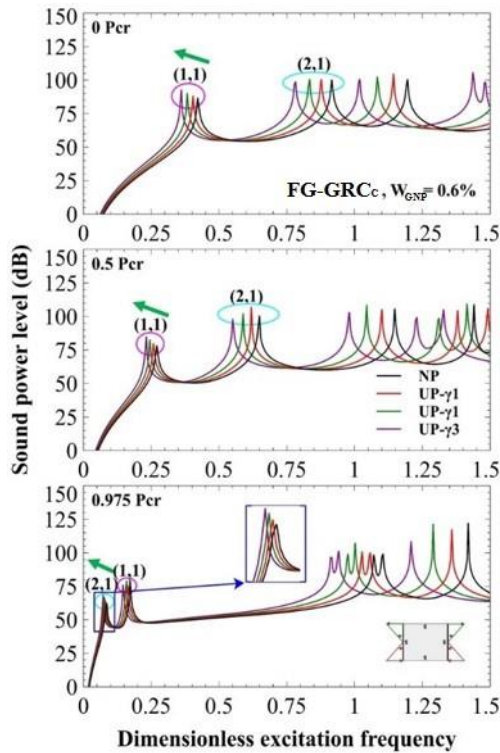
Impact of *GNPs* grading/weight percentage, porosity dispersion/coefficients on sound radiation behaviour of porous FG-GRC plate under the NUE loads is presented in Figure 6.6. The same excitation conditions used in forced vibration response of porous FG-GRC is considered for sound radiation analyses also. From Figure 6.6, it is evident that fundamental peak shift towards lower frequency side when there is a increase in magnitude of applied NUE load. Similarly, by comparison it can be seen that sound radiation plots have a similar trend as that of the forced vibration response plots. However, a very drastic reduction in the fundamental peak of sound power is observed compared to the higher mode peaks. As the magnitude of NUE load is varied as a function of P_{cr} , the reduction in resonant peak of fundamental mode is very significant compared to the higher modes. Another one important reason is SWL level radiated is directly related to excitation frequency also. As the sound power is directly proportional to the frequency, very low amplitude of frequency peak is observed at $0.975P_{cr}$ as observed in forced vibration response. One can clearly witness from Figure 6.6 that the change of first mode (1,1) to second mode (2,1) occurs at $0.975P_{cr}$ of NUE load case $\alpha=2$, rest of the NUE load cases the fundamental mode (1,1) remains same for all the buckling load fractions.



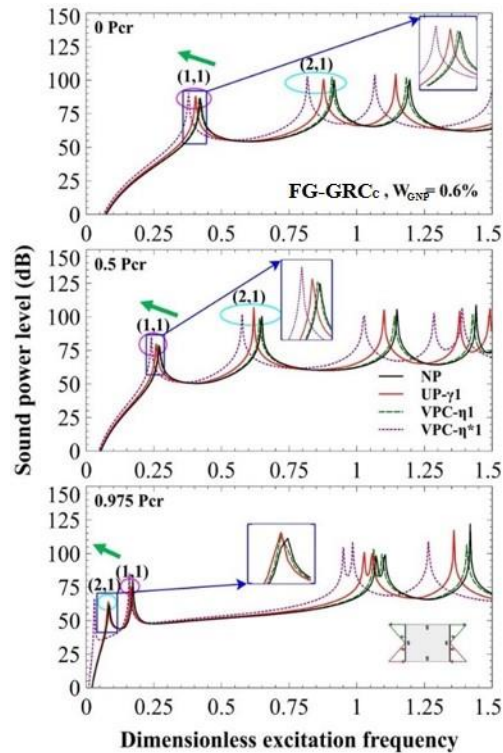
(a) Effect of W_{GNP} grading pattern



(b) Effect of W_{GNP} weight fraction



(c) Effect of porosity coefficient (UP- γ_1 , UP- γ_2 & UP- γ_3)



(d) Effect of porosity coefficient (UP- γ_1 , VPC- η_1 & VPC- η^*1)

Figure 6.6: Effect of porosity coefficients on sound power level of porous FG-GRC plate.

Figure 6.6 (a) and Figure 6.6 (b) illustrate the effect of *GNPs* grading and weight percentage respectively on sound power level of porous FG-GRC plates subjected to NUE loads. In both cases, an increase in stiffness of plate shifts leads to shifting of peaks towards the higher frequency side with a reduction in resonant peak of fundamental mode. According to the nature of *GNPs* grading, fundamental peak of sound power level reduces in order of porous FG-GRC O, UD, X, and C for the given weight percentage of *GNPs*. It is observed that 3, 10, 14, and 20 dB level (i.e., porous FG-GRC O, UD, X, and C) reduction of sound power fundamental peak for $0P_{cr}$, when compared to the pure metal. Further 10 & 29 dB level reduction of sound power for $0.5P_{cr}$ and $0.975P_{cr}$ respectively noted. Resonant amplitudes of sound power radiated reduce with an increase in weight fraction of *GNPs* due to increase in the enhancement of structural stiffness. Porous FG-GRC plate with C type grading pattern of *GNPs* proven to be a superior one as evident from the lowest sound power level peak associated with the fundamental mode compared to the other grading patterns of *GNPs*. Figure 6.6 (c) and Figure 6.6 (d) illustrates the impact of porosity grading pattern and coefficients on SWL of porous FG-GRC.

It is noted that the porosity effect reduces the stiffness of the plate which further causes shifting of the peak towards the lower excitation frequency value, with the little increase in dB level as clearly seen in the fundamental mode. It is observed that 2, 4 and 8-dB level (i.e., UP- γ_1 , UP- γ_2 & UP- γ_3) increase and 2, 3 and 7-dB level (i.e., UP- γ_1 , VPC- η_1 & VPS- η^*1) increase in sound power fundamental peak for $0P_{cr}$, when compared to the pure metal. Further 6 and 32-dB level reduction of SWL is noted for $0.5P_{cr}$ and $0.975P_{cr}$ loads respectively. It is found that peak amplitude of SWL radiated is influenced by the nature of the porosity grading and it reduces in the order of VPS, UP, VPC, and non-porous cases similar to forced vibration response of the plate.

Figure 6.7 shows impact of NUE loads on porous FG-GRC and it is observed that there is a reduction in fundamental frequency peak with increase in the value of α . A mild shifting of fundamental frequency values is observed at $0.5P_{cr}$ load fraction. However, a very drastic reduction in the peak and natural frequency of the fundamental mode is observed for the $0.975P_{cr}$ load. Figure 6.8 illustrates the impact

of load fraction of NUE and porosity co-efficient on sound radiation efficiency, it denotes that the NUE

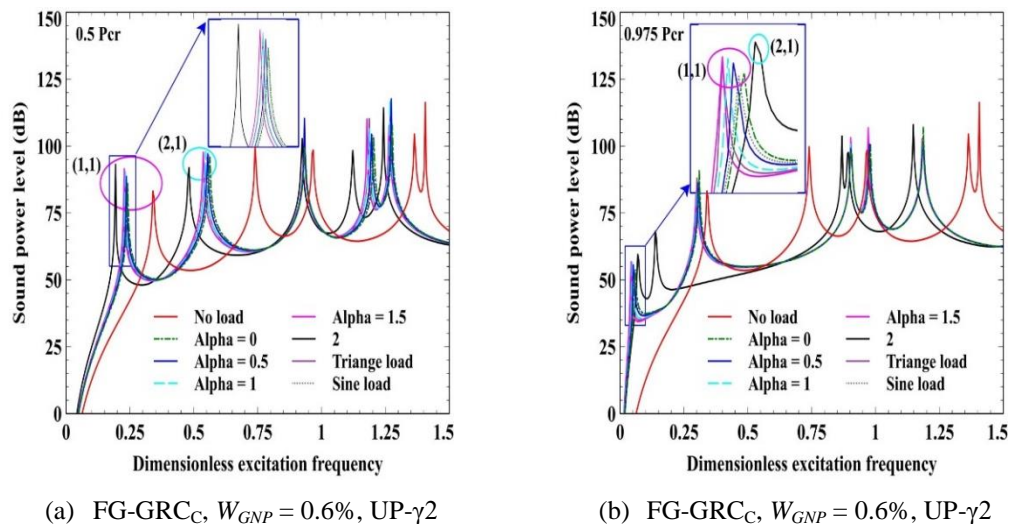


Figure 6.7: Effect of different NUE load on sound power level of porous FG-GRC plate.

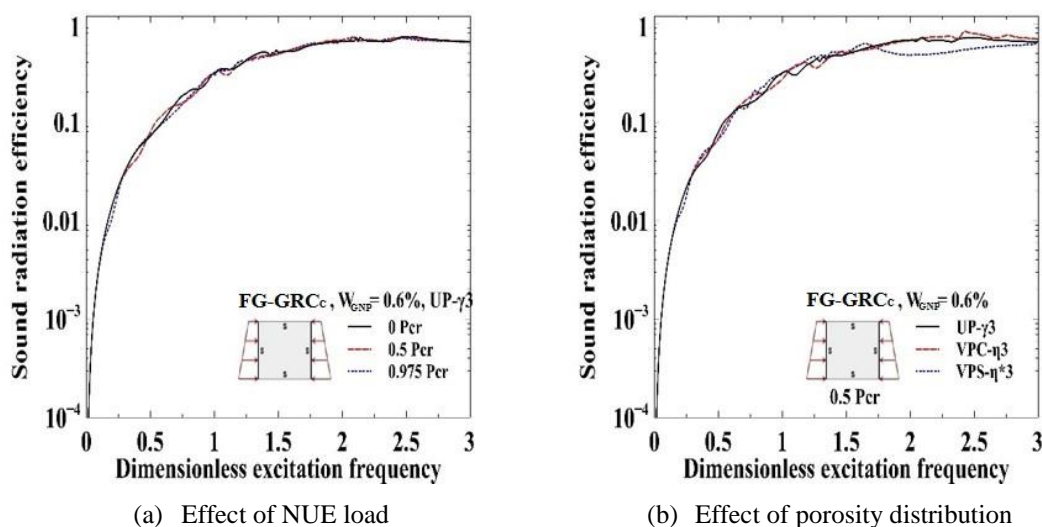
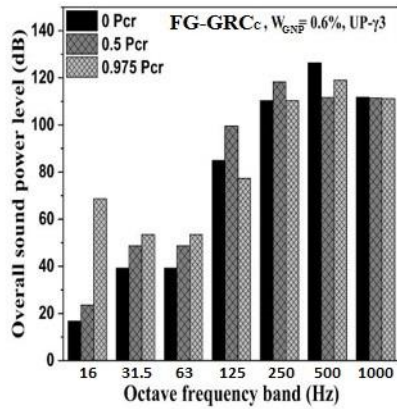
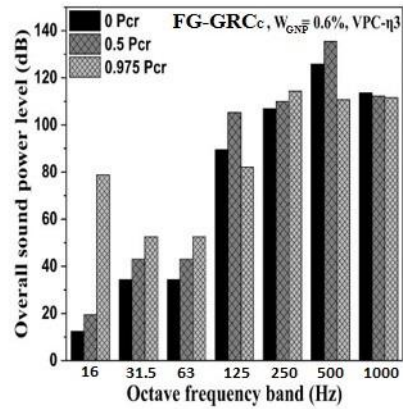


Figure 6.8: Effect of NUE loads and porosity factor on sound radiation efficiency.

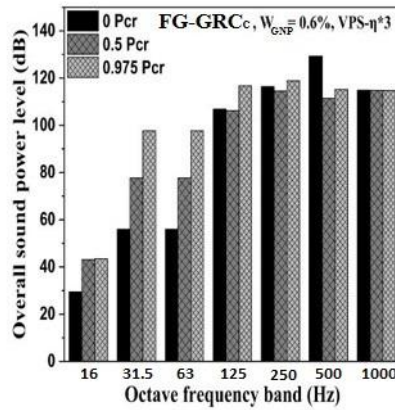
load fraction and porosity grading does not have any impact on sound radiation efficiency. A similar trend of sound radiation efficiency is observed for rest of other cases. Figure 6.9 shows the influence of porous grading on sound power level in constant octave bandwidths. It indicates that the impact of porous grading pattern is substantial in lower frequency bandwidths as the increase of NUE load intensity, compared to mid and high octave frequency bandwidths. Overall sound power level (OSWL) corresponding NUE load intensity (i.e., $0P_{cr}$, $0.5P_{cr}$ and $0.975P_{cr}$) for



(a) Effect of VPC porosity distribution, $\alpha = 1.5$



(b) Effect of VPS porosity distribution, $\alpha = 1.5$



(c) Effect of UP porosity distribution, $\alpha = 1.5$

Figure 6.9: Effect of porosity coefficient on overall sound power level (dB) vs octave frequency band.

different porosity grading patterns are shown in Figure 6.10. Disparity in overall SWL with a increase of magnitude of NUE load is significant, OSWL increase 6 dB for $0.5P_{cr}$ and 12 dB for $0.975P_{cr}$ compared to no-load case.

The directivity pattern for porous FG-GRC plate is obtained at ($x = 0.25$ m, $y = 0.2$ m, and $z = 1$ m) from the lower left corner of the plate. The plate is excited at the fundamental frequency for this study. Figure 6.11 (a) and Figure 6.11 (c) shows the effect of NUE loads on SPL radiated by porous FG-GRC, whereas Figure 6.11 (b) and Figure 6.11 (d) shows the effect of porosity distribution and coefficients under the

buckling load (i.e., $0.5P_{cr}$). A symmetric pattern of sound pressure radiation is observed due to symmetric mode (1,1) for the selected cases.

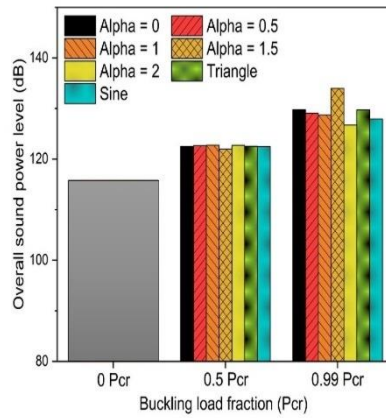
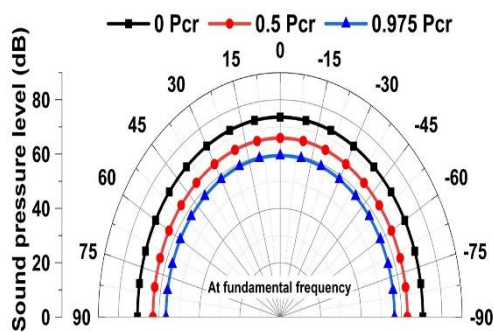
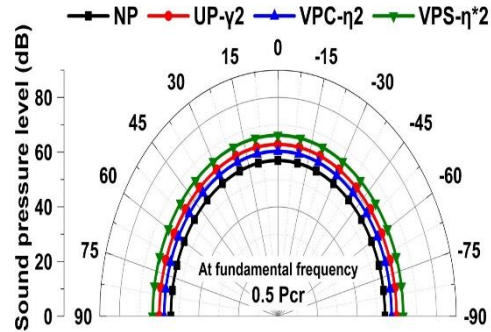


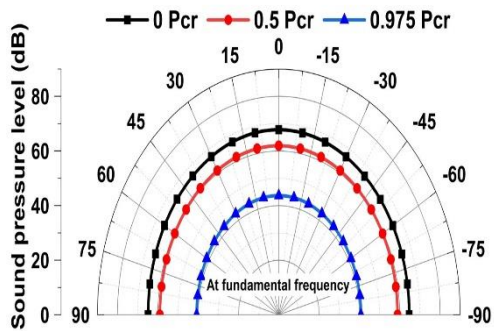
Figure 6.10: Effect of NUE load and porosity factor on the overall sound power level (dB).



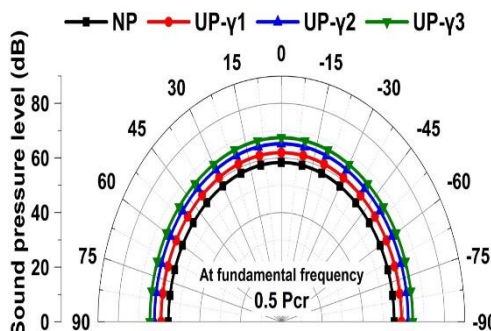
(a) FG-GRC_C, $W_{GNP} = 0.3\%$, $\alpha = 0$, UP- γ_1



(b) FG-GRC_C, $W_{GNP} = 0.3\%$, $\alpha = 1$

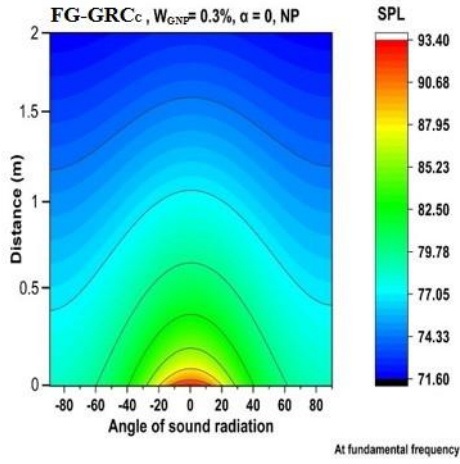


(c) FG-GRC_C, $W_{GNP} = 0.6\%$, Triangle load, VPC- η_3

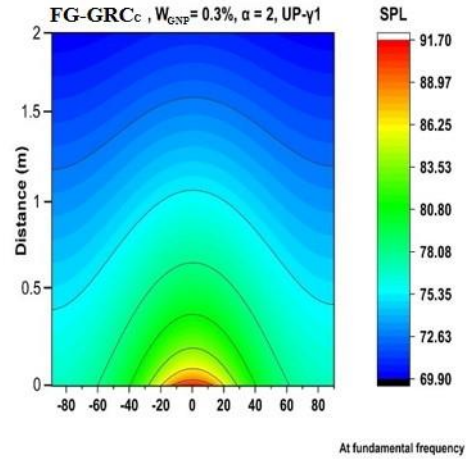


(d) FG-GRC_C, $W_{GNP} = 0.6\%$, Sine load

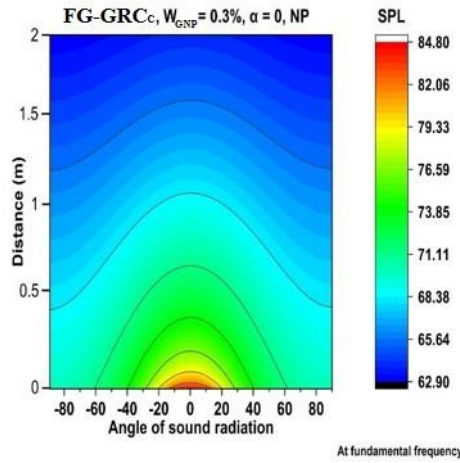
Figure 6.11: Effect of NUE load and porosity factor on directivity pattern is obtained at a one-meter radius above the centre of the plate (z-axis).



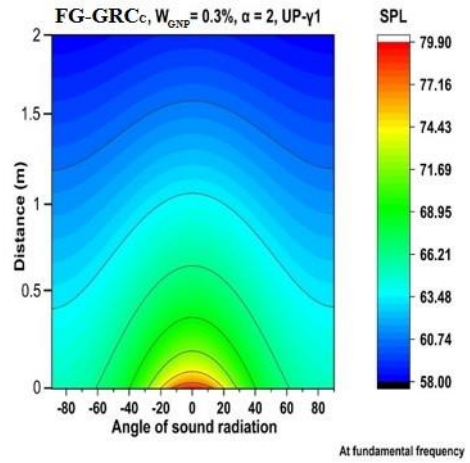
(a) SPL distribution pattern at $0 P_{cr}$



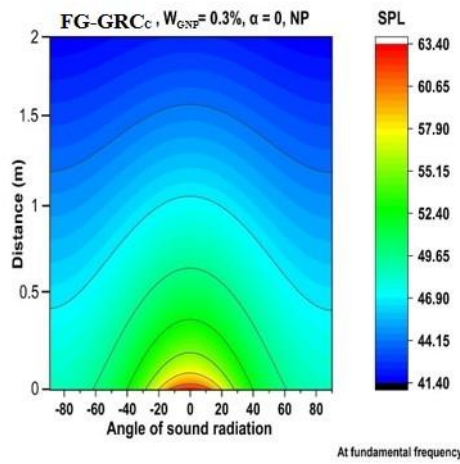
(b) SPL distribution pattern at $0 P_{cr}$



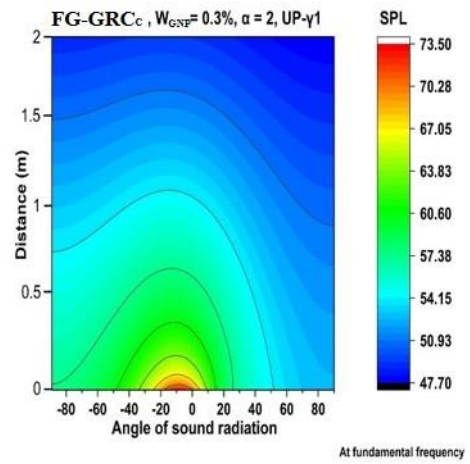
(c) SPL distribution pattern at $0.5 P_{cr}$



(d) SPL distribution pattern at $0.5 P_{cr}$



(e) SPL distribution pattern at $0.975 P_{cr}$



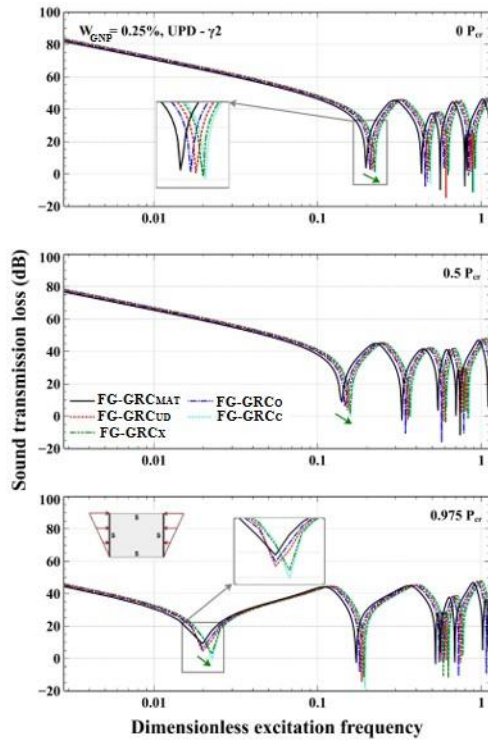
(f) SPL distribution pattern at $0.975 P_{cr}$

Figure 6.12: Contour representational effect of porosity coefficient on SPL radiated.

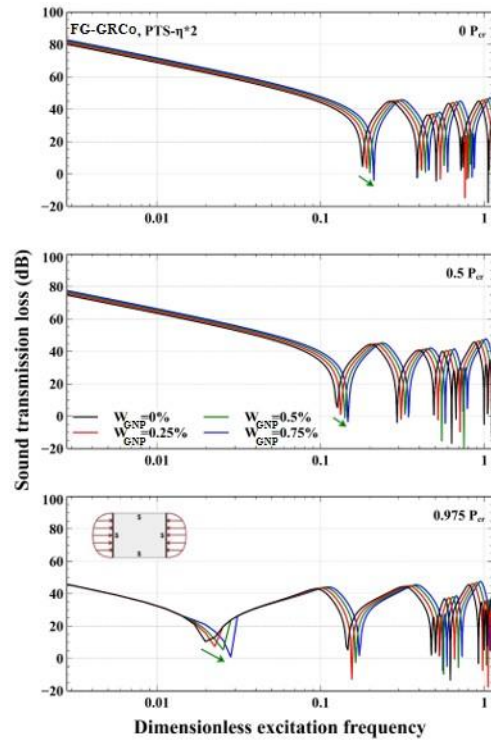
The sound pressure level distribution pattern of porous FG-GRC is significantly affected by the buckling load fraction and porosity factor as clearly seen in Figure 6.11. Contour plot representation of the SPL distribution under the influence of NUE loads and porosity factor is demonstrated in Figure 6.12. It is observed that for load factor $\alpha=2$ at load fraction of $0.975P_{cr}$ the SPL distribution is un-symmetric in nature due to the jumping of fundamental mode from (1,1) to (2,1). However, symmetric distribution of SPL is observed in the remaining cases as there is no jumping of fundamental mode with an increase in load fraction.

6.5.Sound transmission loss characteristics

The porous FG-GRC plates subjected to a pressure wave having intensity of $1 N/m^2$ under different types of NUE loads are analysed for the sound transmission loss characteristics. The sound transmission loss plot can be divided into three main sections which is dependent on stiffness, damping and mass. The stiffness region signifies a bandwidth between zero to the first resonance peak, where it is observed that increase in the magnitude of NUE load has a significant reduction in the dB level. This is due to the stiffness softening effect cause by the magnitude of NUE load, as a result it causes an increase of normal velocity of the plate and consequently decreases the resonant amplitude. Hence, it is revealed that increase in magnitude of NUE load tends to huge variation in frequencies peaks and reduction in the sound transmission loss level. The damping region signifies a narrow bandwidth of the resonance peak of the STL plot. This region represents the amount of damping which causes a negative STL region. However, the negative region signifies various inherent characteristics of the porous FG-GRC plate. It is observed that the fundamental resonance peak is suppressed when compared to the higher resonances peak due to the reinforcing effect of *GNPs* present in porous FG-GRC plate. The region after the fundamental peak is sensitive of mass, since there is no specific change in the mass of FG-Graphene reinforced plate subjected to NUE loads. Figure 6.13 shows the effect of different dispersion grading and weight percentage of *GNPs* on the FG-Graphene reinforced plates. Figure 6.14 shows the impact of different NUE loads on sound transmission loss of porous FG-GRC, it is noted that similar trend in sound radiation results is also observed in the sound transmission loss.

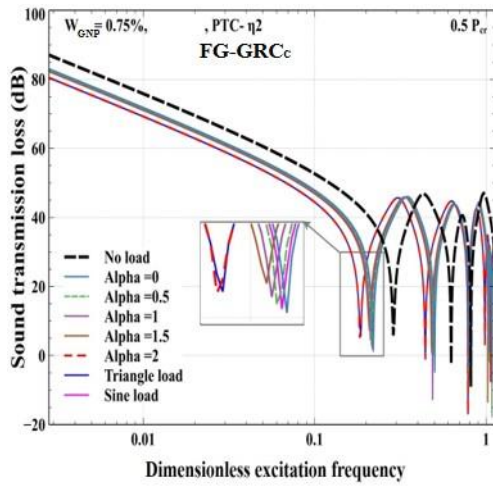


(a) Effect of W_{GNP} grading pattern

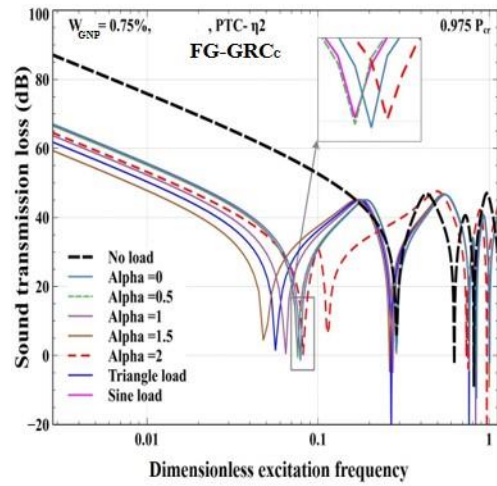


(b) Effect of W_{GNP} weight fraction

Figure 6.13: Effect of porosity coefficients on sound transmission loss of porous FG-GRC plate.



(a) FG-GRC_C, $W_{GNP} = 0.6\%$, VPC- γ_2



(b) FG-GRC_C, $W_{GNP} = 0.6\%$, VPC- γ_2

Figure 6.14: Effect of different NUE load on sound transmission loss of porous FG-GRC plate.

6.6. Closure

Vibro-acoustic characteristics of different porous FG-GRC plates subjected to the NUE loads are investigated analytically. Influence of various parameters like graphene nanoplatelets (*GNPs*) grading/weight percentage, porosity distribution/coefficients and nature of NUE load configuration on buckling and vibro-acoustic behaviour of porous FG-GRC plate are investigated. Based on a detailed analytical study, due to equal combined effect of tensile and compressive load acting at the edge of porous FG-GRC plate, load case $\alpha=2$ obtains high structural stability and buckling strength. The shifting of fundamental frequency modal indices from (1,1) to (2,1) occurs at the $0.975P_{cr}$ load fraction of the $\alpha=2$ case. It is noted that both *GNPs* grading and weight fraction factors has a significant influence in enhancing stiffness of the porous FG-GRC plate, by shifting the frequency peaks towards the higher frequency value and reduces the sound power level emitted by the fundamental mode. Whereas both porosity distribution/coefficients act as a reducing stiffness effect, by shifting the frequency peak towards the lower frequency value and a slight increase in power level emitted by the fundamental mode. No significant effects of NUE loads and porosity factor observed in the sound radiation efficiency, but in OWSL plot it has significant effect in low frequency bandwidths when compared to mid and higher octave frequency bandwidths. FG-GRC with $W_{GNP} = 0.6\%$ proven to be a superior grading pattern in porous FG-GRC plate, by obtaining high stiffness and less dB level emitted by the fundamental mode compared to the rest of the grading and weight percentage of *GNPs*. FG-GRC_C of $W_{GNP}=0.6\%$ with VPC porosity distribution obtains superior case with high stiffness strength then the UP and VPS porosity distribution, when compared to non-porous FG-GRC plate.

CHAPTER 7

7. SUMMARY AND CONCLUSIONS

7.1. Summary

Detailed analytical investigation is carried out to analyze the vibration, sound radiation and transmission loss characteristics of metal and functionally graded graphene reinforced nanocomposites panels under the influence of non-uniform uniaxial edge loads is presented. Detailed parametric study is carried out to analyze the influence of different graphene nanoplatelets grading/weight percentage, porosity distribution/coefficients and nature of NUE load configurations on the vibro-acoustic performance of the nano composite plate. An analytical approach followed in the present work is based on the effective material properties of graphene reinforced nanocomposites with different grading pattern/weight fraction of graphene nanoplates are obtained by grouping of modified Halpin-Tsai model and rule of mixture. In order to model the porous graphene reinforced nanocomposites, closed-cell cellular solids under Gaussian Random Field (GRF) are used. An analytical method based on the strain energy approach is used to calculate the buckling load. Free and forced vibration responses of the plate are obtained using an analytical method based on Reddy's TSDT while acoustic behaviour is analysed using Rayleigh Integral. The analytical approach is validated by comparing its results with results available in published literature based on theoretically modelled 2D continuum orthotropic plate of FG-graphene reinforced nanocomposites.

7.2. Conclusions

7.2.1. Studies of the isotropic plate

From the analytical investigation carried out on vibro-acoustic behavior of isotropic plate under the influence of non-uniform uniaxial edge loads.

- It is found that the buckling load parameter significantly influenced by NUE load variation. The fundamental buckling mode for $\alpha = 2$ is (2,1) while for the remaining cases it is (1,1) for the aspect ratio $(a/b) = 1.25$.
- Higher buckling load is observed for $\alpha=2$ case due to the structural stability obtained by the combined effect of tensile and compressive forces.
- Better variation in average RMS velocity with increase in magnitude of NUE load is observed when the plate is analysed by varying P_{cr} of the respective edge load case.
- In acoustical radiation characteristics, the effect of NUE load has a major role which signifies the 17 dB level of SWL level reduces at $0.975P_{cr}$ of fundamental frequency peak when compared to the no-load condition, and slight increase in amplitude of fundamental frequency peak for the $0.5P_{cr}$ due to the stiffness interference of the structure.
- In sound radiation efficiency, there is no significant variation has been observed concerning the non-uniform buckling load.
- The increase in magnitude of the NUE load has a significant effect on the SWL only at the lower frequency band and there is no variation in the overall SWL.
- The effect of applied NUE load is significant only in the stiffness region hence remarkable change in STL is observed only in the stiffness region compared to the damping and mass regions.

7.2.2. Free vibration studies of FG-GRC plate

From the analytical investigation carried out on free vibration behavior of isotropic plate under the influence of non-uniform uniaxial edge loads.

- It is evident from the isotropic studies, that the increase of load factor (α), increases the buckling strength of the FG-GRC plate subjected to the NUE load. Due to this reason, the FG-GRC plate under $\alpha = 2$ load case obtains better stability and withstand higher buckling load when compared to rest of NUE loads because of addition stiffness gained by the tensile force.
- It is noted that minute increase in W_{GNP} of $GNPs$ results in a significant increase of the stiffness parameter of rectangular FG-GRC plate, as an outcome it leads to a increase in buckling load and natural frequencies.
- The distribution pattern of $GNPs$ for a given fraction of $GNPs$ has a huge impact on the stiffness parameter of the rectangular FG-GRC plate.
- It is noted that the FG-GRC_C pattern shows the superior buckling and free vibration characteristics when compared to the other cases due to the enhanced bending stiffness associated with FG-GRC_C pattern.

7.2.3. Vibro-acoustic studies of FG-GRC plate

From the analytical investigation carried out on vibro-acoustic behavior of FG-GRC plate under the influence of non-uniform uniaxial edge loads.

- The FG-GRC plate having $a/b=0.5$, buckles with (1,1) mode for all the load cases. However, when $a/b = 1.25$, the plate buckles with (1,1) mode for all cases, except for $\alpha=2$ case for which it buckles with (2,1) mode. Hence, higher the aspect ratio (a/b), the FG-GRC plate buckles at higher modal indices for $\alpha = 2$ case when compared to the rest of NUE loads.
- In sound radiation characteristics, the influences of non-uniform compressive load have significant reduction of sound power level of approximately 30 dB level at $0.99P_{cr}$ of fundamental peak when compared to the no-load condition, and slight decrease in the amplitude of fundamental frequency peak for the $0.5 P_{cr}$ due to the stiffness interference of the structure.

- In sound radiation efficiency, no significant variation has been observed concerning the variation in NUE load. But in overall sound power level plot, it indicates when load fraction increases the overall SWL also increased with increase of buckling load fraction.
- It is evident from the isotropic studies, for FG-GRC plates same trend has been observed in change of dB level in the stiffness region compared to the damping and mass regions. Also, GNPs grading and weight fraction has significant influence in sound transmission loss characteristics.
- It is observed that the FG-GRC_C with $W_{GNP} = 0.6\%$ proven to be a superior grading pattern in FG-GRC plate, by obtaining high stiffness and less dB level emitted by the fundamental mode compared to the rest of the grading and weight percentage of *GNPs*.

7.2.4. Vibro-acoustic study of porous FG-GRC plate

From the analytical investigation carried out on vibro-acoustic behavior of porous FG-GRC plate under the influence of non-uniform uniaxial edge loads.

- It is evident from the previous study on vibro-acoustic characteristics of FG-GRC plate, that both *GNPs* grading and weight fraction factors has a significant influence in enhancing stiffness of the porous FG-GRC plate, by shifting the frequency peaks towards the higher frequency value and reduces the sound power level emitted by the fundamental mode.
- Whereas both porosity distribution/coefficients act as a reducing stiffness effect, by shifting the frequency peak towards the lower frequency value and a slight increase in power level emitted by the fundamental mode.
- No significant effects of NUE loads and porosity factor observed in the sound radiation efficiency, but in OWSL plot it has significant effect in low frequency bandwidths when compared to mid and higher octave frequency bandwidths.
- FG-GRC_C of $W_{GNP} = 0.6\%$ with VPC porosity distribution obtains superior case with high stiffness strength then the UP and VPS porosity distribution, when compared to non-porous FG-GRC plate.

7.3.Scope for Future Research

The present work focuses on the influence of non-uniform uniaxial edge loads on the vibro-acoustic characteristics of flat isotropic/porous functionally graded graphene reinforced nanocomposites under simply supported boundary conditions. In future this work can be extended to carry out

- The vibro-acoustic characteristics of isotropic/porous FG-graphene reinforced nanocomposites under different non-uniform biaxial/shear edge loads and boundary conditions.
- Experimental investigation on vibro-acoustic characteristics of isotropic/porous FG-graphene reinforced nanocomposites under different NUE loads.
- Vibro-acoustic behavior of skew isotropic/ FG-graphene reinforced nanocomposites under different NUE loads.

Appendix A. Different Coefficients of [K] and [M] are given as

$$[K] = \begin{bmatrix} k_{11} & k_{12} & k_{13} & k_{14} & k_{15} \\ k_{12} & k_{22} & k_{23} & k_{24} & k_{25} \\ k_{13} & k_{23} & k_{33} & k_{43} & k_{53} \\ k_{14} & k_{24} & k_{34} & k_{44} & k_{54} \\ k_{15} & k_{25} & k_{35} & k_{45} & k_{55} \end{bmatrix}; [Q] = \begin{bmatrix} 0 \\ 0 \\ q_{mn} \\ 0 \\ 0 \end{bmatrix};$$

$$[M] = \begin{bmatrix} m_{11} & m_{12} & m_{13} & m_{41} & m_{51} \\ m_{12} & m_{22} & m_{23} & m_{42} & m_{52} \\ m_{13} & m_{23} & m_{33} & m_{43} & m_{53} \\ m_{14} & m_{24} & m_{34} & m_{44} & m_{54} \\ m_{15} & m_{25} & m_{35} & m_{45} & m_{55} \end{bmatrix}; [\psi] = \begin{bmatrix} u_{mn} \\ v_{mn} \\ w_{mn} \\ \phi_x \\ \phi_y \end{bmatrix};$$

$$\begin{aligned} m_{11} &= m_{22} = I_0; \\ m_{31} &= m_{13} = -c_1 I_3(\underline{\tau}); \quad m_{32} = m_{23} = -c_1 I_3(\underline{\varepsilon}); \\ m_{43} &= m_{34} = -c_1 J_4(\underline{\tau}); \quad m_{53} = m_{35} = -c_1 J_4(\underline{\varepsilon}); \\ m_{41} &= m_{14} = m_{25} = m_{52} = J_1; \\ m_{12} &= m_{15} = m_{21} = m_{24} = 0; \\ m_{42} &= m_{45} = m_{51} = m_{54} = 0; \\ m_{33} &= I_0 + c_1^2 I_6(\underline{\tau}^2 + \underline{\varepsilon}^2); \\ m_{44} &= m_{55} = K_2; \end{aligned}$$

where

$$\begin{aligned} (I_0, I_i) &= \int_{-h/2}^{h/2} \rho(1, z^i) dz; \quad (i = 1, 2, \dots) \\ J_i &= I_i - c_1 I_{i+2}; \quad (i = 1, 4) \\ K_2 &= I_2 - 2c_1 I_4 + c_1^2 I_6; \\ k_{11} &= -(A_{11}(\underline{\tau})^2 + A_{66}(\underline{\varepsilon})^2); \quad k_{22} = -(A_{66}(\underline{\tau})^2 + A_{22}(\underline{\varepsilon})^2); \\ k_{12} &= -(A_{11} + A_{66})(\underline{\tau})(\underline{\varepsilon}); \\ k_{13} &= c_1 E_{11}(\underline{\tau})^3 + (c_1 E_{12} + 2c_1 E_{66})(\underline{\tau})(\underline{\varepsilon})^2; \\ k_{14} &= (-B_{11} + c_1 E_{11})(\underline{\tau})^2 + (-B_{66} + c_1 E_{66})(\underline{\varepsilon})^2; \\ k_{15} &= -(B_{12} + B_{66} - c_1 E_{12} - c_1 E_{66})(\underline{\tau})(\underline{\varepsilon}); \\ k_{23} &= (c_1 E_{12} + 2c_1 E_{66})(\underline{\tau})^2(\underline{\varepsilon}) + c_1 E_{22}(\underline{\varepsilon})^3; \\ k_{24} &= -(B_{21} + B_{66} - c_1 E_{21} - c_1 E_{66})(\underline{\tau})(\underline{\varepsilon}); \\ k_{25} &= (-B_{66} + c_1 E_{66})(\underline{\tau})^2 + (B_{22} - c_1 E_{22})(\underline{\varepsilon})^2; \\ k_{33} &= -\left((A_{55} - 6c_1 D_{55} + 9c_1^2 F_{55})(\underline{\tau})^2 + (A_{44} - 6c_1 D_{44} + 9c_1^2 F_{44})(\underline{\varepsilon})^2 \right) \\ &\quad - c_1^2 H_{55}(\underline{\tau})^4 - 2(c_1^2 H_{12} + 2c_1^2 H_{66})(\underline{\tau})^2(\underline{\varepsilon})^2 \\ &\quad - c_1^2 H_{22}(\underline{\varepsilon})^4 - N_{xx}(BLR)(\underline{\tau})^2 - N_{yy}(\underline{\varepsilon})^2; \end{aligned}$$

$$\begin{aligned}
k_{34} &= -(A_{55} - 6c_1D_{55} + 9c_1^2F_{55})(\underline{\tau}) + (c_1F_{11} - c_1^2H_{11})(\underline{\tau})^3 \\
&\quad + (2c_1F_{66} - 2c_1^2H_{66} + c_1F_{21} - c_1^2H_{21})(\underline{\tau})(\underline{\varepsilon})^2; \\
k_{35} &= -(A_{44} - 6c_1D_{44} + 9c_1^2F_{44})(\underline{\varepsilon}) + (c_1F_{22} - c_1^2H_{22})(\underline{\varepsilon})^3 \\
&\quad + (2c_1F_{12} - 2c_1^2H_{66} + c_1F_{66} - c_1^2H_{12})(\underline{\varepsilon})(\underline{\tau})^2; \\
k_{44} &= (-D_{11} - 2c_1F_{11} - c_1^2H_{11})(\underline{\tau})^2 + (-D_{66} - 2c_1F_{66} - c_1^2H_{66})(\underline{\varepsilon})^2 \\
&\quad - (A_{55} - 6c_1D_{55} + 9c_1^2F_{55}); \\
k_{45} &= (-D_{12} - 2c_1F_{12} - c_1^2H_{12} - D_{66} - 2c_1F_{66} - c_1^2H_{66})(\underline{\tau})(\underline{\varepsilon}); \\
k_{55} &= (-D_{66} - 2c_1F_{66} - c_1^2H_{66})(\underline{\tau})^2 + (-D_{22} - 2c_1F_{22} - c_1^2H_{22})(\underline{\varepsilon})^2 \\
&\quad - (A_{44} - 6c_1D_{44} + 9c_1^2F_{44});
\end{aligned}$$

where

$$(A_{ij}, B_{ij}, D_{ij}, E_{ij}, F_{ij}, H_{ij}) = \sum_{k=1}^{N_L} \int_{z_k}^{z_{k+1}} Q_{ij}^k(1, z, z^2, z^3, z^4, z^6) dz \quad (i, j = 1, 2, 6)$$

REFERENCE

- Affdl, J. H., and Kardos, J. L.** (1976). The Halpin-Tsai equations: a review. *Polymer Engineering & Science*, 16(5), 344-352.
- AKBAŞ, Ş. D.** (2017). Stability of a non-homogenous porous plate by using generalized differential quadrature method. *International Journal of Engineering and Applied Sciences*, 9(2), 147-155.
- Arefi, M., Bidgoli, E. M. R., Dimitri, R., and Tornabene, F.** (2018). Free vibrations of functionally graded polymer composite nanoplates reinforced with graphene nanoplatelets. *Aerospace Science and Technology*, 81, 108-117.
- Arunkumar, M. P., Pitchaimani, J., Gangadharan, K. V., and Babu, M. L.** (2016). Influence of nature of core on vibro acoustic behavior of sandwich aerospace structures. *Aerospace Science and Technology*, 56, 155-167.
- Arunkumar, M. P., Pitchaimani, J., Gangadharan, K. V., and Leninbabu, M. C.** (2018). Vibro-acoustic response and sound transmission loss characteristics of truss core sandwich panel filled with foam. *Aerospace Science and Technology*, 78, 1-11.
- Ashby, M. F., Evans, T., Fleck, N. A., Hutchinson, J. W., Wadley, H. N. G., and Gibson, L. J.** (2000). *Metal foams: a design guide*. Elsevier.
- Assaf, S., and Guerich, M.** (2008). Numerical prediction of noise transmission loss through viscoelastically damped sandwich plates. *Journal of Sandwich Structures & Materials*, 10(5), 359-384.
- Baker, G., Pavlović, M. N., and Tahan, N.** (1993). An exact solution to the two-dimensional elasticity problem with rectangular boundaries under arbitrary edge forces. *Philosophical Transactions of the Royal Society of London. Series A: Physical and Engineering Sciences*, 343(1668), 307-336.
- Bakshi, S. R., Lahiri, D., and Agarwal, A.** (2010). Carbon nanotube reinforced metal matrix composites-a review. *International materials reviews*, 55(1), 41-64.

- Bert, C. W., and Devarakonda, K. K.** (2003). Buckling of rectangular plates subjected to nonlinearly distributed in-plane loading. *International Journal of Solids and Structures*, 40(16), 4097-4106.
- Bonaccorso, F., Colombo, L., Yu, G., Stoller, M., Tozzini, V., Ferrari, A. C., ... and Pellegrini, V.** (2015). Graphene, related two-dimensional crystals, and hybrid systems for energy conversion and storage. *Science*, 347(6217).
- Chandra, N., Raja, S., and Gopal, K. N.** (2014). Vibro-acoustic response and sound transmission loss analysis of functionally graded plates. *Journal of Sound and Vibration*, 333(22), 5786-5802.
- Chandra, Y., Chowdhury, R., Scarpa, F., Adhikari, S., Sienz, J., Arnold, C., ... and Bould, D.** (2012). Vibration frequency of graphene-based composites: a multiscale approach. *Materials Science and Engineering: B*, 177(3), 303-310.
- Chen, J., Cui, P., and Li, Q. S.** (2020). Free Vibrations of Functionally Graded Graphene-Reinforced Composite Blades with Varying Cross-Sections. *International Journal of Structural Stability and Dynamics*, 20(14), 2043006.
- Choi, J. B., and Lakes, R. S.** (1995). Analysis of elastic modulus of conventional foams and of re-entrant foam materials with a negative Poisson's ratio. *International Journal of Mechanical Sciences*, 37(1), 51-59.
- D'Alessandro, V., Petrone, G., Franco, F., and De Rosa, S.** (2013). A review of the vibroacoustics of sandwich panels: Models and experiments. *Journal of Sandwich Structures & Materials*, 15(5), 541-582.
- De Villoria, R. G., and Miravete, A.** (2007). Mechanical model to evaluate the effect of the dispersion in nanocomposites. *Acta Materialia*, 55(9), 3025-3031.
- Fahy, F. J., and Gardonio, P.** (2007). *Sound and structural vibration: radiation, transmission and response*. Elsevier.
- Ferreira, A. J. M., Roque, C. M. C., Neves, A. M. A., Jorge, R. M. N., Soares, C. M. M., and Liew, K. M.** (2011). Buckling and vibration analysis of isotropic and

laminated plates by radial basis functions. *Composites Part B: Engineering*, 42(3), 592-606.

Fuller, C. R. (1990). Active control of sound transmission/radiation from elastic plates by vibration inputs: I. Analysis. *Journal of Sound and Vibration*, 136(1), 1-15.

Garcia-Macias, E., Rodriguez-Tembleque, L., and Saez, A. (2018). Bending and free vibration analysis of functionally graded graphene vs. carbon nanotube reinforced composite plates. *Composite Structures*, 186, 123-138.

Geng, Q., and Li, Y. (2012). Analysis of dynamic and acoustic radiation characters for a flat plate under thermal environments. *International Journal of Applied Mechanics*, 4(03), 1250028.

Geng, Q., Li, H., and Li, Y. (2014). Dynamic and acoustic response of a clamped rectangular plate in thermal environments: experiment and numerical simulation. *The Journal of the Acoustical Society of America*, 135(5), 2674-2682.

George, N., Pitchaimani, J., Murigendrappa, S. M., and Lenin Babu, M. C. (2018). Vibro-acoustic behavior of functionally graded carbon nanotube reinforced polymer nanocomposite plates. *Proceedings of the Institution of Mechanical Engineers, Part L: Journal of Materials: Design and Applications*, 232(7), 566-581.

Gibson, L. J., and Ashby, M. F. (1999). *Cellular Solids: Structure and Properties*, Cambridge Univ.

Guo, H., Cao, S., Yang, T., and Chen, Y. (2018). Vibration of laminated composite quadrilateral plates reinforced with graphene nanoplatelets using the element-free IMLS-Ritz method. *International Journal of Mechanical Sciences*, 142, 610-621.

Hangai, Y., Takahashi, K., Yamaguchi, R., Utsunomiya, T., Kitahara, S., Kuwazuru, O., and Yoshikawa, N. (2012). Nondestructive observation of pore structure deformation behavior of functionally graded aluminum foam by X-ray computed tomography. *Materials Science and Engineering: A*, 556, 678-684.

- Jagannadham, K.** (2012). Thermal conductivity of copper-graphene composite films synthesized by electrochemical deposition with exfoliated graphene platelets. *Metallurgical and Materials Transactions B*, 43(2), 316-324.
- Jeyaraj, P.** (2010). Vibro-acoustic behavior of an isotropic plate with arbitrarily varying thickness. *European Journal of Mechanics-A/Solids*, 29(6), 1088-1094.
- Jeyaraj, P.** (2013). Buckling and free vibration behavior of an isotropic plate under nonuniform thermal load. *International journal of structural stability and dynamics*, 13(03), 1250071.
- Jeyaraj, P., Ganesan, N., and Padmanabhan, C.** (2009). Vibration and acoustic response of a composite plate with inherent material damping in a thermal environment. *Journal of Sound and Vibration*, 320(1-2), 322-338.
- Jones, R. M.** (2006). *Buckling of bars, plates, and shells*. Bull Ridge Corporation.
- Kang, J. H., and Leissa, A. W.** (2001). Vibration and buckling of SS-F-SS-F rectangular plates loaded by in-plane moments. *International Journal of Structural Stability and Dynamics*, 1(04), 527-543.
- Kang, J. H., and Leissa, A. W.** (2005). Exact solutions for the buckling of rectangular plates having linearly varying in-plane loading on two opposite simply supported edges. *International Journal of Solids and Structures*, 42(14), 4220-4238.
- Khorshidi, K.** (2011). Vibro-acoustic analysis of Mindlin rectangular plates resting on an elastic foundation. *Scientia Iranica*, 18(1), 45-52.
- King, J. A., Klimek, D. R., Miskioglu, I., and Odegard, G. M.** (2015). Mechanical properties of graphene nanoplatelet/epoxy composites. *Journal of Composite Materials*, 49(6), 659-668.
- Kirkup, S. M.** (1994). Computational solution of the acoustic field surrounding a baffled panel by the Rayleigh integral method. *Applied mathematical modelling*, 18(7), 403-407.

- Koohbor, B., and Kidane, A.** (2016). Design optimization of continuously and discretely graded foam materials for efficient energy absorption. *Materials & Design*, 102, 151-161.
- Leissa, A. W.** (1986). Conditions for laminated plates to remain flat under inplane loading. *Composite structures*, 6(4), 261-270.
- Leissa, A. W., and Kang, J. H.** (2001). Exact solutions for the free vibrations and buckling of rectangular plates with linearly varying in-plane loading. *ASME Applied Mechanics Division-Publications-AMD*, 249, 1-18.
- Li, Q., and Yang, D.** (2020). Vibro-acoustic performance and design of annular cellular structures with graded auxetic mechanical metamaterials. *Journal of Sound and Vibration*, 466, 115038.
- Li, S., and Li, X.** (2008). The effects of distributed masses on acoustic radiation behavior of plates. *Applied Acoustics*, 69(3), 272-279.
- Li, Z., Young, R. J., Wilson, N. R., Kinloch, I. A., Vallés, C., and Li, Z.** (2016). Effect of the orientation of graphene-based nanoplatelets upon the Young's modulus of nanocomposites. *Composites Science and Technology*, 123, 125-133.
- Liew, K. M., Wang, J., Ng, T. Y., and Tan, M. J.** (2004). Free vibration and buckling analyses of shear-deformable plates based on FSDT meshfree method. *Journal of Sound and Vibration*, 276(3-5), 997-1017.
- Lin, F., Xiang, Y., and Shen, H. S.** (2017). Temperature dependent mechanical properties of graphene reinforced polymer nanocomposites—a molecular dynamics simulation. *Composites Part B: Engineering*, 111, 261-269.
- Lord, R.** (1945). The theory of sound. *cambridge university press*.
- Mellert, V., Baumann, I., Freese, N., and Weber, R.** (2008). Impact of sound and vibration on health, travel comfort and performance of flight attendants and pilots. *Aerospace Science and Technology*, 12(1), 18-25.

- Mijušković, O., Ćorić, B., and Šćepanović, B.** (2014). Exact stress functions implementation in stability analysis of plates with different boundary conditions under uniaxial and biaxial compression. *Thin-Walled Structures*, 80, 192-206.
- Mirzaei, M., and Kiani, Y.** (2017). Isogeometric thermal buckling analysis of temperature dependent FG graphene reinforced laminated plates using NURBS formulation. *Composite Structures*, 180, 606-616.
- Moita, J. S., Araújo, A. L., Correia, V. F., Soares, C. M. M., and Herskovits, J.** (2020). Buckling behavior of composite and functionally graded material plates. *European Journal of Mechanics-A/Solids*, 80, 103921.
- Natarajan, S., and Padmanabhan, C.** (2019). Scaled boundary finite element method for mid-frequency interior acoustics. *The Journal of the Acoustical Society of America*, 146(4), 3006-3006.
- Neves, A. M. A., Ferreira, A. J. M., Carrera, E., Cinefra, M., Roque, C. M. C., Jorge, R. M. N., and Soares, C. M.** (2013). Static, free vibration and buckling analysis of isotropic and sandwich functionally graded plates using a quasi-3D higher-order shear deformation theory and a meshless technique. *Composites Part B: Engineering*, 44(1), 657-674.
- Novoselov, K. S., Geim, A. K., Morozov, S. V., Jiang, D. E., Zhang, Y., Dubonos, S. V., Grigorieva, I. V., and Firsov, A. A.** (2004). Electric field effect in atomically thin carbon films. *science*, 306(5696), 666-669.
- Petrone, G., D'Alessandro, V., Franco, F., and De Rosa, S.** (2014). Numerical and experimental investigations on the acoustic power radiated by Aluminium Foam Sandwich panels. *Composite Structures*, 118, 170-177.
- Phan, D. H.** (2020). Isogeometric analysis of functionally-graded graphene platelets reinforced porous nanocomposite plates using a refined plate theory. *International Journal of Structural Stability and Dynamics*, 20(07), 2050076.
- Phung-Van, P., Thai, C. H., Nguyen-Xuan, H., and Abdel-Wahab, M.** (2019). An isogeometric approach of static and free vibration analyses for porous FG nanoplates. *European Journal of Mechanics-A/Solids*, 78, 103851.

- Rafiee, M. A., Rafiee, J., Wang, Z., Song, H., Yu, Z. Z., and Koratkar, N.** (2009). Enhanced mechanical properties of nanocomposites at low graphene content. *ACS nano*, 3(12), 3884-3890.
- Rafiee, M. A., Rafiee, J., Yu, Z. Z., and Koratkar, N.** (2009). Buckling resistant graphene nanocomposites. *Applied Physics Letters*, 95(22), 223103.
- Ramteke, P. M., Panda, S. K., and Sharma, N.** (2019). Effect of grading pattern and porosity on the eigen characteristics of porous functionally graded structure. *Steel and Composite Structures*, 33(6), 865-875.
- Reddy, J. N.** (2006). *Theory and analysis of elastic plates and shells*. CRC press.
- Reddy, R. M. R., Karunasena, W., and Lokuge, W.** (2018). Free vibration of functionally graded-GPL reinforced composite plates with different boundary conditions. *Aerospace Science and Technology*, 78, 147-156.
- Roberts, A. P., and Garboczi, E. J.** (2001). Elastic moduli of model random three-dimensional closed-cell cellular solids. *Acta materialia*, 49(2), 189-197.
- Sarıgül, A. S., and Karagözü, E.** (2018). Vibro-acoustic coupling in composite plate-cavity systems. *Journal of vibration and control*, 24(11), 2274-2283.
- Sharma, N., Mahapatra, T. R., and Panda, S. K.** (2018). Numerical analysis of acoustic radiation properties of laminated composite flat panel in thermal environment: a higher-order finite-boundary element approach. *Proceedings of the Institution of Mechanical Engineers, Part C: Journal of Mechanical Engineering Science*, 232(18), 3235-3249.
- Sharma, N., Mahapatra, T. R., and Panda, S. K.** (2018). Numerical analysis of acoustic radiation responses of shear deformable laminated composite shell panel in hygrothermal environment. *Journal of Sound and Vibration*, 431, 346-366.
- Shen, H. S., Xiang, Y., Lin, F., and Hui, D.** (2017). Buckling and postbuckling of functionally graded graphene-reinforced composite laminated plates in thermal environments. *Composites Part B: Engineering*, 119, 67-78.

- Song, M., Kitipornchai, S., and Yang, J.** (2017). Free and forced vibrations of functionally graded polymer composite plates reinforced with graphene nanoplatelets. *Composite Structures*, 159, 579-588.
- Song, M., Yang, J., and Kitipornchai, S.** (2018). Bending and buckling analyses of functionally graded polymer composite plates reinforced with graphene nanoplatelets. *Composites Part B: Engineering*, 134, 106-113.
- Song, M., Yang, J., Kitipornchai, S., and Zhu, W.** (2017). Buckling and postbuckling of biaxially compressed functionally graded multilayer graphene nanoplatelet-reinforced polymer composite plates. *International Journal of Mechanical Sciences*, 131, 345-355.
- Sun, J., Zhao, J., Gong, F., Li, Z., and Ni, X.** (2018). Design, fabrication and characterization of multi-layer graphene reinforced nanostructured functionally graded cemented carbides. *Journal of Alloys and Compounds*, 750, 972-979.
- Talebitooti, R., and Zarastvand, M. R.** (2018). Vibroacoustic behavior of orthotropic aerospace composite structure in the subsonic flow considering the Third order Shear Deformation Theory. *Aerospace Science and Technology*, 75, 227-236.
- Thai, C. H., Ferreira, A. J. M., Tran, T. D., and Phung-Van, P.** (2019). Free vibration, buckling and bending analyses of multilayer functionally graded graphene nanoplatelets reinforced composite plates using the NURBS formulation. *Composite Structures*, 220, 749-759.
- Thompson, D. J., Gardonio, P., and Rohlfing, J.** (2009). Can a transmission coefficient be greater than unity?. *Applied acoustics*, 70(5), 681-688.
- Timoshenko, S. P., and Gere, J. M.** (2009). Theory of elastic stability. Mineola.
- Tiwari, A., and Syväjärvi, M.** (2015). *Graphene materials: fundamentals and emerging applications*. John Wiley & Sons.
- Wang, Y. Q., and Zhang, Z. Y.** (2019). Bending and buckling of three-dimensional graphene foam plates. *Results in Physics*, 13, 102136.

- Wicklein, M., and Thoma, K.** (2005). Numerical investigations of the elastic and plastic behaviour of an open-cell aluminium foam. *Materials Science and Engineering: A*, 397(1-2), 391-399.
- Wu, H., Kitipornchai, S., and Yang, J.** (2017a). Thermal buckling and postbuckling of functionally graded graphene nanocomposite plates. *Materials & Design*, 132, 430-441.
- Wu, H., Yang, J., and Kitipornchai, S.** (2017b). Dynamic instability of functionally graded multilayer graphene nanocomposite beams in thermal environment. *Composite Structures*, 162, 244-254.
- Wu, H., Yang, J., and Kitipornchai, S.** (2018). Parametric instability of thermo-mechanically loaded functionally graded graphene reinforced nanocomposite plates. *International Journal of Mechanical Sciences*, 135, 431-440.
- Xu, Z., and Huang, Q.** (2019). Vibro-acoustic analysis of functionally graded graphene-reinforced nanocomposite laminated plates under thermal-mechanical loads. *Engineering Structures*, 186, 345-355.
- Yang, J., Chen, D., and Kitipornchai, S.** (2018). Buckling and free vibration analyses of functionally graded graphene reinforced porous nanocomposite plates based on Chebyshev-Ritz method. *Composite Structures*, 193, 281-294.
- Yang, T., Zheng, W., Huang, Q., and Li, S.** (2016). Sound radiation of functionally graded materials plates in thermal environment. *Composite Structures*, 144, 165-176.
- Yasmin, A., and Daniel, I. M.** (2004). Mechanical and thermal properties of graphite platelet/epoxy composites. *Polymer*, 45(24), 8211-8219.
- Zaman, I., Kuan, H. C., Dai, J., Kawashima, N., Michelmore, A., Sovi, A., Doug, S., Luong, L., and Ma, J.** (2012). From carbon nanotubes and silicate layers to graphene platelets for polymer nanocomposites. *Nanoscale*, 4(15), 4578-4586.
- Zhang, H., Shi, D., Zha, S., and Wang, Q.** (2018). Vibro-acoustic analysis of the thin laminated rectangular plate-cavity coupling system. *Composite Structures*, 189, 570-585.

Zhong, H., and Gu, C. (2006). Buckling of simply supported rectangular Reissner–Mindlin plates subjected to linearly varying in-plane loading. *Journal of engineering mechanics*, 132(5), 578-581.

Zhou, K., Lin, Z., Huang, X., and Hua, H. (2019). Vibration and sound radiation analysis of temperature-dependent porous functionally graded material plates with general boundary conditions. *Applied Acoustics*, 154, 236-250.

Zhao, S., Zhao, Z., Yang, Z., Ke, L., Kitipornchai, S., and Yang, J. (2020). Functionally graded graphene reinforced composite structures: A review. *Engineering Structures*, 210, 110339.

CURRICULUM VITAE

1. Name: **VIJAY G**
2. Date of Birth: 06/12/1991
3. Permanent Address: Pl.No: 27, D.No: 31, Deva Nagar,
Reddiarpalayam Post,
Puducherry – 605010, India.
4. Mobile Number: 9597931989 / 9606315655
5. Email ID: yajiv62@gmail.com
/yajiv.177me022@nitk.edu.in
6. Education Qualification:

2013 Bachelor of Engineering
Institution: Vellore Institute of Technology University,
Vellore Campus,
Vellore, Tamil Nadu, India.
Specialization: Mechanical Engineering

2017 Master of Engineering
Institution: Vellore Institute of Technology University,
Chennai Campus,
Chennai, Tamil Nadu, India.
Specialization: Computer-aided design and Computer-aided
manufacturing (CAD/CAM)

2021 Doctor of Philosophy
Institution: National Institute of Technology Karnataka,
Surathkal, Karnataka, India.
Registration Date: 07/07/2017
Thesis Submission Date: 07/10/2021
Viva-Voice Date:

LIST OF PUBLICATIONS BASED ON THESIS

International Journals

1. Gunasekaran, V., Pitchaimani, J., & Chinnapandi, L. B. M. (2020). Vibro-acoustics response of an isotropic plate under non-uniform edge loading: An analytical investigation. *Aerospace Science and Technology*, 105, 106052. (SCI, IF = 5.107).
2. Gunasekaran, V., Pitchaimani, J., & Chinnapandi, L. B. M. (2020). Analytical investigation on free vibration frequencies of polymer nano composite plate: Effect of graphene grading and non-uniform edge loading. *Materials Today Communications*, 24, 100910. (SCI, IF = 2.678).
3. Gunasekaran, V., Pitchaimani, J., & Chinnapandi, L. B. M. (2021). Acoustic radiation and transmission loss of FG-Graphene composite plate under nonuniform edge loading. *European Journal of Mechanics-A/Solids*, 88, 104249. (SCI, IF = 4.220).
4. Gunasekaran, V., Pitchaimani, J., Chinnapandi, L. B. M. & Kumar, A. (2021). Sound Radiation Characteristics of Porous Graphene Nanocomposites Plate: Effect of Porosity and Arbitrary Edge Loading. *International Journal of Structural Stability and Dynamics*, 20(05), 2050068. (SCI, IF = 2.558).

International Conferences

1. Gunasekaran, V., Pitchaimani, J., & Chinnapandi, L. B. M. (2018). Vibro-acoustic behavior of an isotropic plate under edgewise compression loads. *Western Pacific Commission for Acoustics*, New Delhi (11th – 15th November).